LBNL-46174

ERNEST ORLANDO LAWRENCE
BERKELEY NATIONAL LABORATORY

Enhanced Mass Removal due to Phase Explosion during High Irradiance Nanosecond Laser Ablation of Silicon

Jong H. Yoo

Environmental Energy Technologies Division

May 2000

Ph.D. Thesis

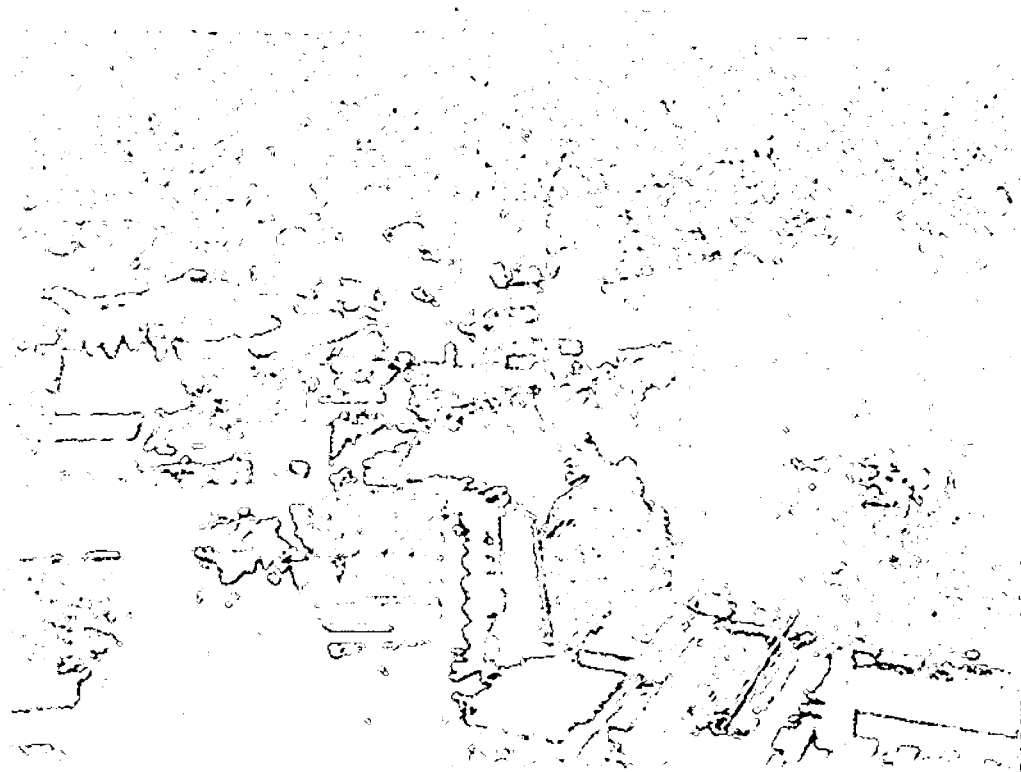

REFERENCE COPY
Does Not
Circulate
Bldg. 50 Library - Ref.
Lawrence Berkeley National Laboratory

LBNL-46174
Copy 1

DISCLAIMER

This document was prepared as an account of work sponsored by the United States Government. While this document is believed to contain correct information, neither the United States Government nor any agency thereof, nor The Regents of the University of California, nor any of their employees, makes any warranty, express or implied, or assumes any legal responsibility for the accuracy, completeness, or usefulness of any information, apparatus, product, or process disclosed, or represents that its use would not infringe privately owned rights. Reference herein to any specific commercial product, process, or service by its trade name, trademark, manufacturer, or otherwise, does not necessarily constitute or imply its endorsement, recommendation, or favoring by the United States Government or any agency thereof, or The Regents of the University of California. The views and opinions of authors expressed herein do not necessarily state or reflect those of the United States Government or any agency thereof, or The Regents of the University of California.

Ernest Orlando Lawrence Berkeley National Laboratory
is an equal opportunity employer.

DISCLAIMER

This document was prepared as an account of work sponsored by the United States Government. While this document is believed to contain correct information, neither the United States Government nor any agency thereof, nor the Regents of the University of California, nor any of their employees, makes any warranty, express or implied, or assumes any legal responsibility for the accuracy, completeness, or usefulness of any information, apparatus, product, or process disclosed, or represents that its use would not infringe privately owned rights. Reference herein to any specific commercial product, process, or service by its trade name, trademark, manufacturer, or otherwise, does not necessarily constitute or imply its endorsement, recommendation, or favoring by the United States Government or any agency thereof, or the Regents of the University of California. The views and opinions of authors expressed herein do not necessarily state or reflect those of the United States Government or any agency thereof or the Regents of the University of California.

LBNL-46174

Enhanced Mass Removal due to Phase Explosion during High Irradiance Nanosecond Laser Ablation of Silicon

Jong Hyun Yoo
Ph.D. Thesis

Mechanical Engineering Department
University of California, Berkeley

and

Environmental Energy Technologies Division
Ernest Orlando Lawrence Berkeley National Laboratory
University of California
Berkeley, CA 94720

May 2000

This work was supported by the Director, Office of Science, Office of Basic Energy Sciences, of the U.S. Department of Energy under Contract No. DE-AC03-76SF00098.

Enhanced Mass Removal due to Phase Explosion during High Irradiance Nanosecond Laser Ablation of Silicon

by

Jong Hyun Yoo

B.S. (University of California, Berkeley) 1993
M.S. (Stanford University) 1994

A dissertation submitted in partial satisfaction of the

requirements for the degree of

Doctor of Philosophy

in

Engineering - Mechanical Engineering

in the

GRADUATE DIVISION

of the

UNIVERSITY OF CALIFORNIA, BERKELEY

Committee in charge:

Professor Ralph Greif, Chair
Professor Costas P. Grigoropoulos
Professor Per Peterson

Spring 2000

Enhanced Mass Removal due to Phase Explosion during High Irradiance Nanosecond Laser Ablation of Silicon

Copyright © 2000

by

Jong Hyun Yoo

The U.S. Department of Energy has the right to use this document
for any purpose whatsoever including the right to reproduce
all or any part thereof.

Abstract

Enhanced Mass Removal due to Phase Explosion during High Irradiance Nanosecond Laser Ablation of Silicon

by

Jong Hyun Yoo

Doctor of Philosophy in Engineering

University of California at Berkeley

Professor Ralph Greif, Chair

The morphology of craters resulting from high irradiance laser ablation of silicon was measured using a white light interferometry microscope. The craters show a dramatic increase in their depth and volume at a certain irradiance, indicating a change in the primary mechanism for mass removal. Laser shadowgraph imaging was used to characterize and differentiate the mass ejection processes for laser irradiances above and below the threshold value. Time-resolved images show distinct features of the mass ejected at irradiances above the threshold value including the presence of micron-sized particulates; this begins at approximately 300 ~ 400 ns after the start of laser heating.

The analysis of the phenomena was carried out by using two models: a thermal evaporation model and a phase explosion model. Estimation of the crater depth due to the thermally evaporated mass led to a large underestimation of the crater depth for irradiances above the threshold. Above the threshold irradiance,

the possibility of phase explosion was analyzed. Two important results are the thickness of the superheated liquid layer that is close to the critical temperature and the time for vapor bubbles that are generated in the superheated liquid to achieve a critical size. After reaching the critical size, vapor bubbles can grow spontaneously resulting in a violent ejection of liquid droplets from the superheated volume. The effects of an induced transparency, i.e. of liquid silicon turning into an optically transparent liquid dielectric medium, are also introduced. The estimated time for a bubble to reach the critical size is in agreement with the delay time measured for the initiation of large mass ejection. Also, the thickness of the superheated liquid layer that is close to the critical temperature at the time of the beginning of the large mass ejection is representative of the crater depth at the threshold irradiance. These results suggest that phase explosion is a plausible thermal mechanism for high irradiance laser ablation.

Laser processing parameters were also investigated for nanosecond laser ablation of silicon. Longer incident wavelengths and larger laser beam sizes were associated with higher values of a threshold irradiance.

To My Parents and Wife, Miyeun

Table of Contents

DEDICATION iii

TABLE OF CONTENTS iv

LIST OF FIGURES viii

LIST OF TABLES xiii

ACKNOWLEDGEMENTS xiv

Chapter 1 INTRODUCTION

1.1 Laser ablation technology: overview 1

1.2 Scope of the present work 4

References 6

Chapter 2 DRAMATIC CHANGE IN CRATER PROPERTIES DURING NANOSECOND LASER ABLATION OF SILICON: ONSET OF NEW ABLATION MECHANISM UNDER HIGH IRRADIANCE

2.1 Introduction 8

2.2 Experimental system 10

2.2.1 Laser ablation set-up 10

2.2.2 Crater characterization using whitelight interferometry microscope 13

2.3 Results and discussion 15

2.4 Conclusions 24

References 26

Chapter 3 TIME-RESOLVED SHADOWGRAPH IMAGING OF EJECTED MASS DURING HIGH IRRADIANCE LASER ABLATION OF SILICON

3.1 Introduction 28

3.2 Experimental system 31

3.2.1 Shadowgraph imaging for nanosecond laser ablation of silicon 31

3.2.2 Shadowgraph imaging for picosecond laser ablation of silicon 32

3.3 Results and discussion 36

3.3.1 Ejection of large particulates above the threshold irradiance For nanosecond ablation of silicon 36

3.3.2 Early time shadowgraph imaging of the air plasma and vapor plume during picosecond laser ablation of silicon 38

3.4 Conclusions 42

References 52

Chapter 4 PHASE EXPLOSION (EXPLOSIVE BOILING) AND INDUCED TRANSPARENCY DURING HIGH IRRADIANCE LASER ABLATION

4.1 Introduction 54

4.2 Background on phase explosion (explosive boiling) 56

4.3 Threshold irradiance for phase explosion 58

4.4 Delay in mass ejection due to phase explosion 63

4.5 Analysis by solution of the energy equation 65

4.5.1 Thermal evaporation 65

4.5.2 Induced transparency of liquid silicon near the critical temperature and phase explosion 68

4.6 Calculated results and discussion 73

4.6.1 Thermal equilibrium model 77

4.6.2 Induced-transparency model 78

4.7 Conclusions 87

References 89

Chapter 5 DEPENDENCE OF PHASE EXPLOSION ON LASER SAMPLING PARAMETERS AND ITS EFFECTS ON INDUCTIVELY COUPLED MASS SPECTROMETRY

5.1 Introduction 92

5.2 Experimental system 94

5.3 Results and discussion 95

5.3.1 Phase explosion and correlation of crater depth with respect to ICP-MS intensity counts 95

5.3.2 Influence of laser wavelength and beam size on phase explosion 96

5.3.3 Dependence of the entrainment and transport efficiency on the laser irradiance 105

5.4 Conclusions 113

References 115

Chapter 6 CONCLUSIONS AND FUTURE DIRECTIONS

6.1 Conclusions 117

6.2 Future directions 120

List of Figures

Chapter 2

Figure 2.1 Schematic diagram of the laser ablation experimental system

Figure 2.2 Improvement of laser beam profile with the pinhole spatial filter

Figure 2.3 Schematic diagram of white light interferometric microscope

Figure 2.4 3D White light interferometric microscope images of the craters at various laser irradiances (FWHM = 3 ns): a) 2.6×10^9 W/cm^2, b) 1.2×10^{10} W/cm^2, c) 2.0×10^{10} W/cm^2, d) 2.4×10^{10} W/cm^2, e) 3.6×10^{10} W/cm^2, and f) 5.1×10^{10} W/cm^2

Figure 2.5 Cross sectional view of the craters at various laser irradiances (FWHM = 3 ns): a) 2.6×10^9 W/cm^2, b) 1.2×10^{10} W/cm^2, c) 2.0×10^{10} W/cm^2, d) 2.4×10^{10} W/cm^2, e) 3.6×10^{10} W/cm^2, and f) 5.1×10^{10} W/cm^2

Figure 2.6 Enlarged 3-D image of crater produced at 1.2×10^{10} W/cm^2

Figure 2.7 SEM images of the crater for a) laser irradiance slightly below the explosive boiling threshold and b) laser irradiance slightly above the threshold. The focused laser spot size was 50 μm

Figure 2.8 Crater volume and depth as a function of laser irradiance

Figure 2.9 The ratio of Volume_{up} to Volume_{down} as a function of the laser power irradiance

Chapter 3

Figure 3.1 Schematic diagram of relevant processes during short pulse laser irradiance

Figure 3.2 Schematic diagram for shadow graph imaging of the ejected mass from the sample surface for nanosecond laser ablation of silicon

Figure 3.3 Laser shadowgraph imaging schematic for early time ejecta gas dynamics during picosecond laser ablation of silicon

Figure 3.4 Sequence of mass ejection images obtained by laser shadowgraphy for the laser irradiance (FWHM = 3 ns) of 1.9×10^{10} W/cm^2

Figure 3.5 Sequence of mass ejection images obtained by laser shadowgraphy for the laser irradiance (FWHM = 3 ns) of 3.9×10^{10} W/cm^2

Figure 3.6 Sequence of mass ejection images obtained by laser shadowgraphy for the laser irradiance (FWHM = 3 ns) of 8.7×10^{10} W/cm^2

Figure 3.7 Crater depth as a function of laser irradiance for picosecond laser ablation of silicon (FWHM = 35 ps)

Figure 3.8 Time-resolved shadowgraph images of air plasma and vapor plume during picosecond laser ablation (FWHM = 35 ps) of silicon at 1.9×10^{12} W/cm^2

Figure 3.9 Time-resolved shadowgraph images of air plasma and vapor plume during picosecond laser ablation (FWHM = 35 ps) of silicon at 6.0×10^{12} W/cm^2

Figure 3.10 Time-resolved shadowgraph images of air plasma and vapor plume during picosecond laser ablation (FWHM = 35 ps) of silicon at 9.8×10^{12} W/cm^2

Figure 3.11 Dependence of air plasma and vapor plume formation on laser irradiance at selected times. (a) 68 ps and (b) 1.0 ns (FWHM = 35 ps)

Chapter 4

Figure 4.1 Spinodal lines and metastable regions on a P-V diagram

Figure 4.2 Region showing superheating of liquid silicon on a generalized P-T diagram

Figure 4.3 Sequence of possible processes in the superheated liquid during laser heating of the sample

Figure 4.4 Schematic diagram for enthalpy-temperature relation during melting

Figure 4.5 Schematic diagram of the sample during induced-transparency in the superheated liquid

Figure 4.6 Comparison of measured crater depths (●) with the computed data. (❑ : maximum depth of induced-transparency layer, ◊ : thickness of liquid layer with temperature greater than $0.8T_c$ at t=200ns, Δ : evaporation depth)

Figure 4.7 Receding velocity of the evaporation front with respect to laser pulse energy. (Thermal evaporation model)

Figure 4.8 Variation of surface temperature for different laser fluences (Thermal evaporation model)

Figure 4.9 Variation of maximum depth of computed induced-transparency layer with respect to thermodynamic critical temperature

Figure 4.10 Temperature distribution inside the sample at different elapsed times (Induced-transparency model, F=100 J/cm^2)

Figure 4.11 Temperature distribution inside the sample for different laser fluence at 200 ns after laser pulse irradiation is initiated (Induced-transparency model)

Chapter 5

Figure 5.1 Correlation of Integrated ICP-MS signal with the crater depth for high irradiance laser ablation of silicon involving phase explosion

Figure 5.2 Crater depths as a function of laser irradiance for different laser beam sizes at λ = 266 nm

Figure 5.3 Crater depths as a function of laser irradiance for different laser beam sizes at λ = 532 nm

Figure 5.4 Crater depths as a function of laser irradiance for different laser beam sizes at λ = 1064 nm

Figure 5.5 Dependence of crater depth on incident laser wavelength for laser beam size of 35 μm

Figure 5.6 Wavelength-dependent absorption of incident laser light in silicon (L_T = thermal penetration depth, α_P = optical penetration depth)

Figure 5.7 Dependence of phase explosion threshold on laser beam sizes at λ = 532 nm

Figure 5.8 Ratio of integrated ICP-MS intensity to net crater volume as a function of laser irradiance

Figure 5.9 Crater depths as a function of laser irradiance at λ = 266 nm on a linear scale (replot of Figure 5.2)

List of Tables

Table 4.1 Thermal and optical properties of silicon

Acknowledgements

This dissertation has not been possible without encouragement and support from many people. First of all, I would like to express my deep gratitude towards my parents for their continuous support and guidance throughout my life. They have sacrificed their lives in their home country, Republic of Korea, and moved to the U.S to create better education opportunities for my brothers and me. Because of them, my life has been so much more enriched both culturally and intellectually. I am also profoundly indebted to my wife, Miyeun for her patience and support. Living separated while I was in school was very difficult for both of us. However, her understanding and support gave the extra strength to focus on the school work and complete this dissertation.

I would like to thank my research advisor Professor Ralph Greif of Mechanical Engineering Department at UC Berkeley. He has assisted me in finding a research assistantship position at Lawrence Berkeley National Laboratory. I greatly valued his detailed review of my research materials and his advice on things both related to academics and life.

I also would like to thank Dr. Richard E. Russo at Lawrence Berkeley National Laboratory (LBNL) for allowing me join his group and providing me with the financial support. He was very patient with my research progress and ultimately guided me to do an independent and original research work.

I appreciate all the research support and friendship that I have received from my colleagues at LBNL. Dr. Sungho Jeong's expertise in the numerical computation made the analysis work on the phase explosion phenomena possible. I also greatly appreciate Dr. Xianglei Mao for his help in setting up many of my experiments. I enjoyed friendship with Sam Mao, Ron Reade, and Oleg Borisov at LBNL.

Finally, I am very grateful to Professor Per F. Peterson and Professor Costas P. Grigoropoulos for reviewing this dissertation and spending time to discuss the work.

Chapter 1

Introduction

1.1 Laser ablation technology: overview

Since the introduction of the first ruby laser in the early 1960s, there has been tremendous progress in manufacturing more sophisticated powerful lasers. Today common solid state Nd:YAG lasers can generate several tens of millijoules of energy in light pulses that are less than a few nanoseconds, resulting in a power on the order of 10^7 W per laser pulse. Further advances in pulse compression technology are now enabling reduction of pulse times to sub-picoseconds and even femtoseconds [1]. Versatility of today's solid state lasers includes tunable wavelength, variable output energy, and variable repetition rate of pulses.

As lasers become more powerful and versatile, their uses have been found in an increasing number of technical applications including pulse laser deposition [2,3], laser surface texturing [4], laser cleaning of the surface [5], optical communication [6], biological surgery [7], machining of miniature devices and sensors [8], generations of nano-particles [9], and chemical analysis [10]. In each of these applications, lasers can offer several advantages over other competing technologies. For example, in the area of pulsed laser deposition, due to the minute amount of film deposited per laser pulse, the thickness of the deposited film can be more precisely controlled as compared to more traditional thin film deposition processes such as physical vapor deposition (PVD) or chemical vapor deposition (CVD). A rapid nonequilibrium heating of the target results in congruent

evaporation of different elements in the target material and deposition of a multi-component film that has the exact stoichiometry as the source is possible. Furthermore, a highly energetic vapor plume formed by the short laser pulse enables the formation of a crystalline film with a lower substrate temperature.

In the area of micromachining of miniature devices and sensors, using a short laser pulse time can offer direct-write capability, saving many of the lithography steps that are needed in traditional wet or dry etching. Virtually all materials can be machined by the selecting appropriate incident wavelength at which the absorption of light occurs readily. Unlike the planar etching technology used in the fabrication of semiconductor chips, laser micromachining can enable the fabrication of minute three-dimensional structures, which are gaining importance in biomedical devices and sensors. Presently, the use of ultrashort (sub-picosecond or femtosecond) pulses is gaining more attention because thermal effects are minimized by using shorter pulses, allowing machining or patterning of sharper structures.

The use of lasers also offers many advantages in the area of chemical analysis. Traditional chemical sampling techniques require sample preparation procedures, which are often time consuming and hazardous if the sample is toxic. In laser solid sampling, sample preparation is often minimal. In addition, laser solid sampling consumes only a minute amount of sample material, typically in the range of ng or μg per pulse. Thus, there is minimal personal exposure, sample

handling, and instrument contamination with laser solid sampling, which makes this technique very attractive for analyzing, for example, radioactive material.

Despite the growing interest in utilizing laser technology in various applications, an understanding of the processes generated by laser-material interactions has remained elusive. This is especially true for the nonlinear complex processes that occur during short pulse, high irradiance laser ablation. For high irradiance laser ablation, the matter may be heated rapidly to close to the critical temperature where both thermal and optical properties of the sample undergo drastic change [11]. Above the sample surface, an expansion of the evaporating vapor induces a gas dynamic flow in the ambient [12,13]. Moreover, compression of the ambient medium ahead of the expanding mass can result in the formation of a shockwave. The expanding vapor can interact with the latter portion of the laser pulse and create a highly energetic non-equilibrium plasma [14]. These processes influence the fraction of the laser energy that is transmitted to the sample. Sample interaction with the transmitted laser energy and the energy transferred by the secondary processes such as radiative heating induce thermal, electronic, collisional, thermo-mechanical, and a combination of these mechanisms to remove mass from the sample [15,16].

Due to the complexity of the phenomena, analysis of high irradiance laser ablation has been limited by the incomplete knowledge of the relevant mechanisms that are responsible for the mass removal. There are many experimental works using probe beam deflection measurements, fast imaging, fast photography, laser

interferometry, and time of flight measurements to further enhance understanding of the gas dynamics and mass ejection processes resulting from laser-material interactions. One of the most critical issues in laser ablation applications is the control of the quantity of mass removed and the shape of the material ejected. Therefore, a detailed understanding of the relevant gas dynamic and mass ejection processes are crucial for successful implementation of laser ablation technology.

1.2 Scope of the Present Work

This dissertation is devoted to understanding mass removal at high laser irradiance. A threshold irradiation corresponding to a dramatic increase of the removed mass per laser pulse is observed with an altered ejected mass size distribution. In chapter 2, a detailed study of the morphology of the craters created by high irradiance laser ablation of a silicon sample was conducted and a white light interferometry microscope was used to characterize the crater properties. The evidence of a change in the ablation mechanism under high irradiance is obtained by noting the drastic change in the crater morphology at a certain threshold irradiance. Chapter 3 contains experimental shadowgraph imaging studies to characterize the mass ejection process due to the onset of this mechanism. Based on the experimental data obtained from Chapter 2 and 3, Chapter 4 analyzes possible ablation mechanisms that may be responsible for drastic increase in mass removal. Based on the determination of the thickness of the evaporated layer and the superheated liquid layer formed, it is proposed that phase explosion (or

explosive boiling) may be the mechanism responsible for enhanced mass removal. In Chapter 5, a parametric study of the variation of the phase explosion threshold irradiance on laser processing parameters including incident wavelength and beam size is presented for the silicon sample. Conclusions and directions for future research are provided in Chapter 6.

REFERENCE

1. A. Yariv: Optical electronics in modern communications (Oxford University Press, New York, 1997)
2. X. D. Wu, D. Dijkkamp, S. B. Ogale, A. Inam, E. W. Chase, P. F. Miceli, C. C. Chang, J. M. Tarascon, and T. Venkatesan: Appl. Phys. Lett. **51**, 861 (1987)
3. D. H. Lowndes, D. B. Geohegan, A. A. Puretzky, D. P. Norton, and C. M. Rouleau: Science **273**, 898 (1996)
4. P. Baumpart, D.J. Krajnovich, T.A. Nguyen, and A.C. Tam: IEEE Trans. Mag. **31**, 2946 (1995)
5. W. Zapka, W. Ziemlich, W.P. Leung, and A.C. Tam: Microel. Engin. **20** 171 (1993)
6. C.C. Eaglesfield: Laser light; fundamentals and optical communications (St. Martin's Press, London, 1967)
7. A.A. Oraevsky, R.O. Esenaliev, and V.S. Letokhov: Pulsed laser ablation of biological tissue: Review of the mechanism, in Laser ablation; mechanisms and applications, edited by J.C. Miller and R.F. Haglund, Jr. (Springer, New York, 1991)
8. B. Craig: Laser Focus World **34**, 79 (1998)
9. A. M. Morales and C. M. Lieber: Science **279**, 208 (1998)
10. R. E. Russo: Applied Spectroscopy **49**, 14 (1995)

11. V.A. Batanov, F.V. Bunkin, A.M. Prokhorov, and V.B. Fedorov: Sov. Phys. JEPT **36**, 311 (1973)

12. G. Callies, P.Berger, and H. Hugel: J. Phys. D **28**, 1302 (1991)

13. R. Kelly and B. Braren: Appl. Phys. B **53**, 160 (1991)

14. X.L. Mao and R.E. Russo: Appl. Phys. A, **64** 1 (1997)

15. R. Kelly, A. Miotello, B. Braren, A. Gupta, and K. Casey: Nuclear Instruments and Methods in Physics Research B **65**, 187 (1992)

16. R.W. Dreyfus, R. Kelly, and R.E. Walkup: Appl. Phys. Lett. **49**, 1478 (1986)

Chapter 2

Dramatic Change in Crater Properties during Nanosecond Laser Ablation of Silicon: Onset of New Ablation Mechanism under High Irradiance

2.1 Introduction

There is a great deal of interest in utilizing laser ablation for applications such as production of nano-materials, deposition of thin metal and dielectric films, welding and bonding of metal parts, and micromachining of semiconductor materials [1-8]. The use of laser ablation for solid sampling offers many advantages for chemical analysis [9,10,11]. For laser ablation applications, it is important to know the relationship between the quantity and the size of the ablated particulates and the laser irradiance. These parameters directly influence the yield and quality of films for pulsed-laser deposition applications. For laser solid sampling, the quantity and size of the ablated particulates affect the transport efficiency for inductively coupled plasma (ICP), and therefore analytical sensitivity [12,13,14]. A tight laser beam focus is required for machining sub-micron structures and for localized chemical analysis of a sample: therefore, laser irradiance can exceed 10^9 W/cm^2, even for moderate laser energy. However, there have been only a few studies that investigate the particulate nature of the ablated mass at irradiance exceeding 10^9 W/cm^2.

An understanding of mass removal processes during laser ablation requires an identification of the dominant energy transport mechanisms. The removal of mass from the irradiated zone can occur by both thermal and non-thermal mechanisms. Incident laser radiation on metal or semiconductor samples creates a large population of highly excited nonequilibrium electrons in a region near the sample surface. This electronic excitation can lead to bond breaking of the sample material or "desorption", and subsequently can cause atomic-size particulates to be ejected from the surface [15]. For a thermal mechanism, the excited electrons transfer energy to phonons during electron-phonon relaxation. The energy is redistributed through lattice vibrations and consequently, heat is conducted into the sample. The conducted heat may melt the sample and bring its local temperature to the vaporization temperature. Further addition of energy in excess of the heat of vaporization can result in the removal of atomic-size mass from the sample by evaporation. Mass removal in the form of micron-sized droplets can also result from a hydrodynamic instability of the molten liquid layer [16,17,18]. The evaporating vapor can exert a recoil pressure on the melted surface, and molten mass can be pushed radially outward from the irradiated zone [2]. The mass may also be removed in the form of bulk solid flakes with an exfoliation process, in which separation of flakes from the surface occurs along the defects that absorb the laser energy [19,20,21,22].

In this chapter, the ablation of polished pure silicon samples during high laser irradiation ($10^9 - 10^{11}$ W/cm^2) is investigated by measuring characteristics of

the crater. The volume of the crater and the crater morphology were measured using a white light interferometric microscope. The net volume of the crater (the volume of the crater subtracted by that of the rim) multiplied by the density of the silicon indicates the amount of mass removed from the irradiated zone. By measuring this quantity, the dependence of the ablated mass versus laser irradiance was obtained over this irradiance regime. Furthermore, by studying the crater morphology, possible mechanisms that might be present for this irradiance regime are discussed.

2.2 Experimental System

2.2.1 Laser Ablation Set-up

A diagram of the experimental system is shown in Figure 2.1. An Infinity 40-100 Nd-YAG laser (FWHM = 3 ns) emits a beam at 266 nm by quadrupling the fundamental frequency. In order to improve the spatial power profile, the beam was focused through a ~ 50 μm pinhole and collimated using two identical plano-convex (PLCX) lenses (f = 20 cm). The pinhole was placed in a glass vacuum cell with quartz windows to prevent breakdown of air at the focus point. The collimated beam profile was measured with a CCD Camera (Cohu Solid State Camera) and a laser beam analyzer (Spiricon Model LBA-100A). Figure 2.2 shows the beam profile without and with the pinhole spatial filter. Without the pinhole spatial filter, the beam originally had an asymmetric profile with a hot spot

present on its right portion. After passing through the pinhole, the beam has a symmetric profile with a near Gaussian profile.

Without the pinhole **With the pinhole**

Figure 2.2 Improvement of laser beam profile with the pinhole spatial filter

The beam was directed to the silicon sample using a beam splitter (BS 1, R = 50 %) and focused onto the sample surface using a plano-convex quartz lens (f = 20 cm). A polished single crystal silicon wafer (99.99% purity) was diced to 1 x 2 cm^2 rectangular pieces before mounting on a XYZ-micrometer translation stage. The silicon sample was ablated using a laser beam size of 50 μm. The energy of the laser beam was varied by changing energy output of the laser and was measured with a calibrated joulemeter and an oscilloscope (Tektronix Model DSA 602A). The laser fluence ranged from 5 to 400 J/cm^2, which results in irradiance of approximately $1x10^9$ to $1x10^{11}$ W/cm^2. The single laser pulse was generated by external triggering using a function generator (Nicolet Model 42). All experiments in this work were conducted using a single laser pulse (FWHM = 3ns) on a fresh

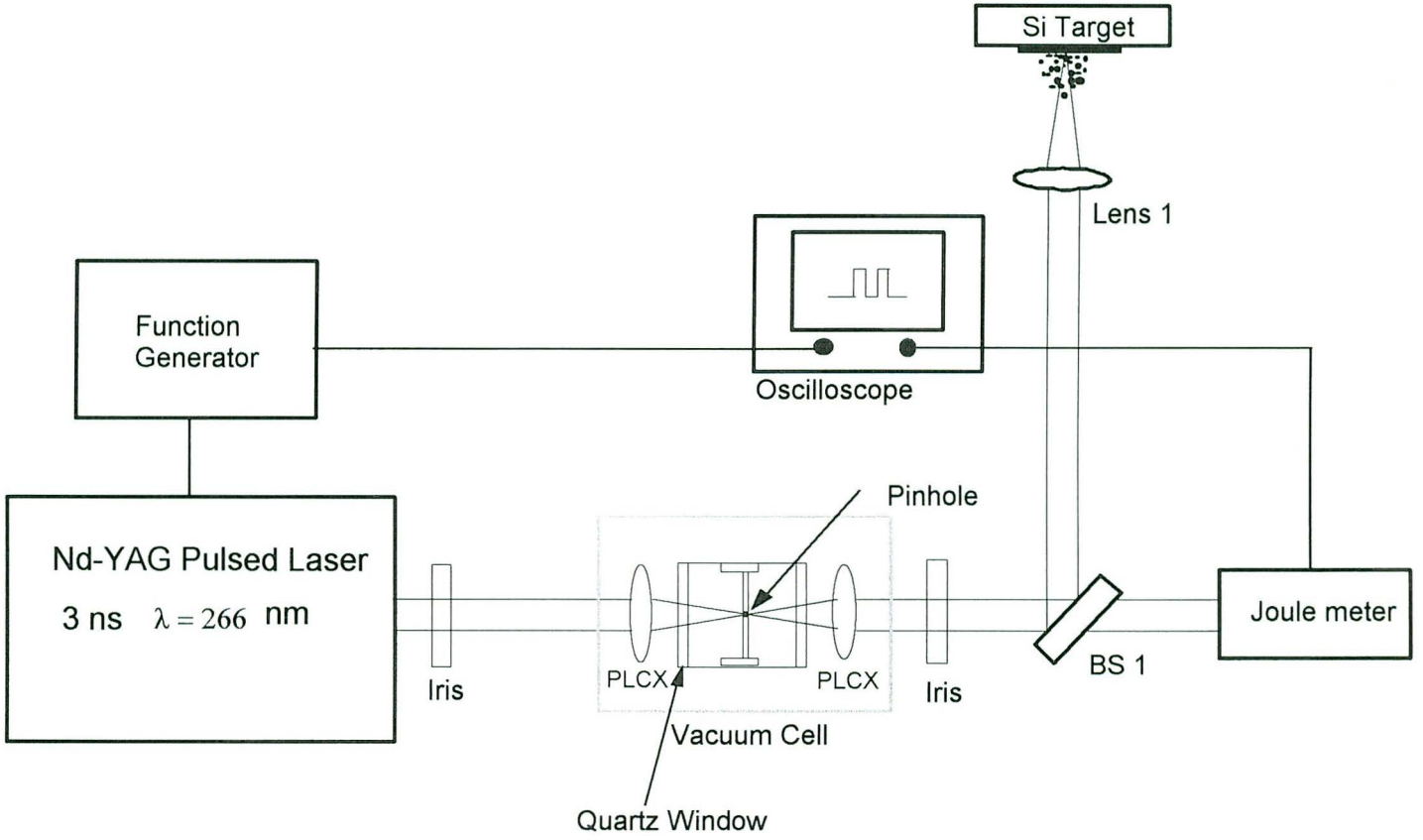

Figure 2.1 Schematic diagram of the laser ablation experimental system

surface location.

2.2.2 Crater Characterization Using Whitelight Interferometry Microscope

The morphology and the volume of the crater were studied with a white light interferometric microscope (Zygo Model NewView 200). Figure 2.3 shows a schematic diagram of the white light interferometric microscope. In NewView 200 microscope, the output light from a white light illuminator is split into two portions by an internal beam splitter. One portion reaches the test sample surface and reflects from it while the other reflects from an internal, high quality reference surface. Both reflected portions are then directed to a solid state camera to form interference fringes. The fringe information is used to identify surface structure of the test sample. The test sample is scanned by moving the objective vertically with a piezoelectric transducer (PZT). This scan enables the collection of the fringe intensity at each camera pixel at a different vertical height of the sample and a three dimensional image of the crater is generated based on the collected data using MetroPro software from Zygo Corporation. For measurement of the craters, a 20X Mirau lens was used with 1.5X and 2.0X image zoom which achieves a 600X and 800X system magnification. At this magnification setting, lateral and vertical resolution of the measurement was 0.88 micron and 0.1 nm. The crater volume is estimated by creating a circular mask for the test region and rectangular masks for the undisturbed surface around the crater. Then image pixels that lie below the

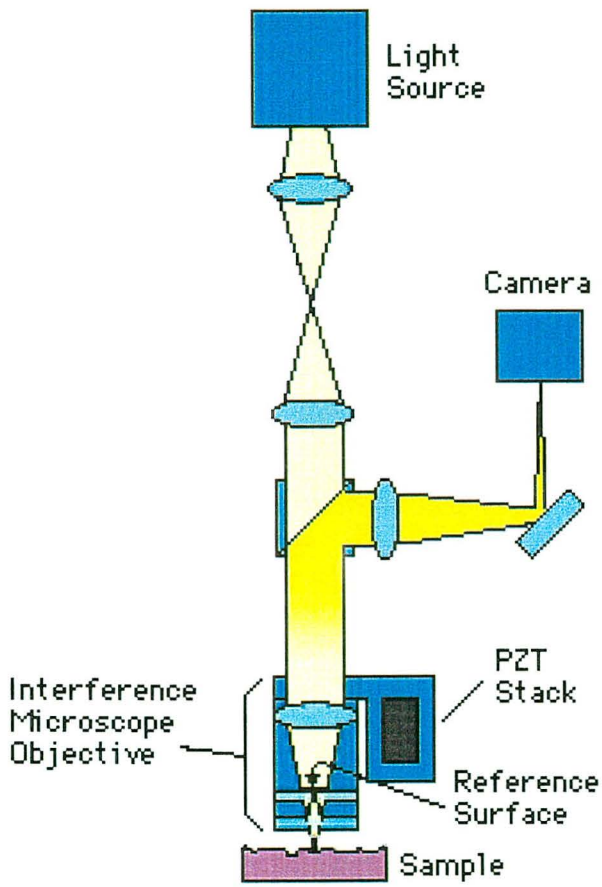

Figure 2.3 Schematic diagram of white light interferometric microscope

rectangular masks were added using MetroPro software to obtain the value for the crater volume.

2.3 Results and Discussion

Figures 2.4 and 2.5 show three-dimensional and cross sectional views, respectively, of the craters at selected laser irradiances from $1x10^9$ to $1x10^{11}$ W/cm^2. Figure 2.4 shows three rows of crater pictures. The top row shows the overall dimensions of the crater in the lateral and vertical direction. The central and bottom rows illustrate crater features when viewed from a plane above and below the original silicon surface, respectively. These crater images show a dramatic change in the crater shape at the irradiance of approximately $2.2x10^{10}$ W/cm^2 (between columns (c) and (d) in Figure 2.4 & (c) and (d) in Figure 2.5) (Note the scale change in Figure 2.5).

For irradiances below $\approx 1.0x10^{10}$ W/cm^2, the craters exhibit a hemispherical shape with a rim above the surface, which is believed to result from the resolidification of molten silicon around the edge of the crater. A melt-flush mechanism may be responsible for the formation of the crater and rim. In Figure 2.5 (a), the bottom of the crater is smooth. With increasing irradiance, both crater diameter and depth increase while maintaining a hemispherical shape. In addition, circular ripples are seen near the edges of the crater (Figure 2.5, (b) & (c) and Figure 2.6). These structures may result from the motion of the molten silicon induced by a lateral pressure gradient between the high pressure plasma above the

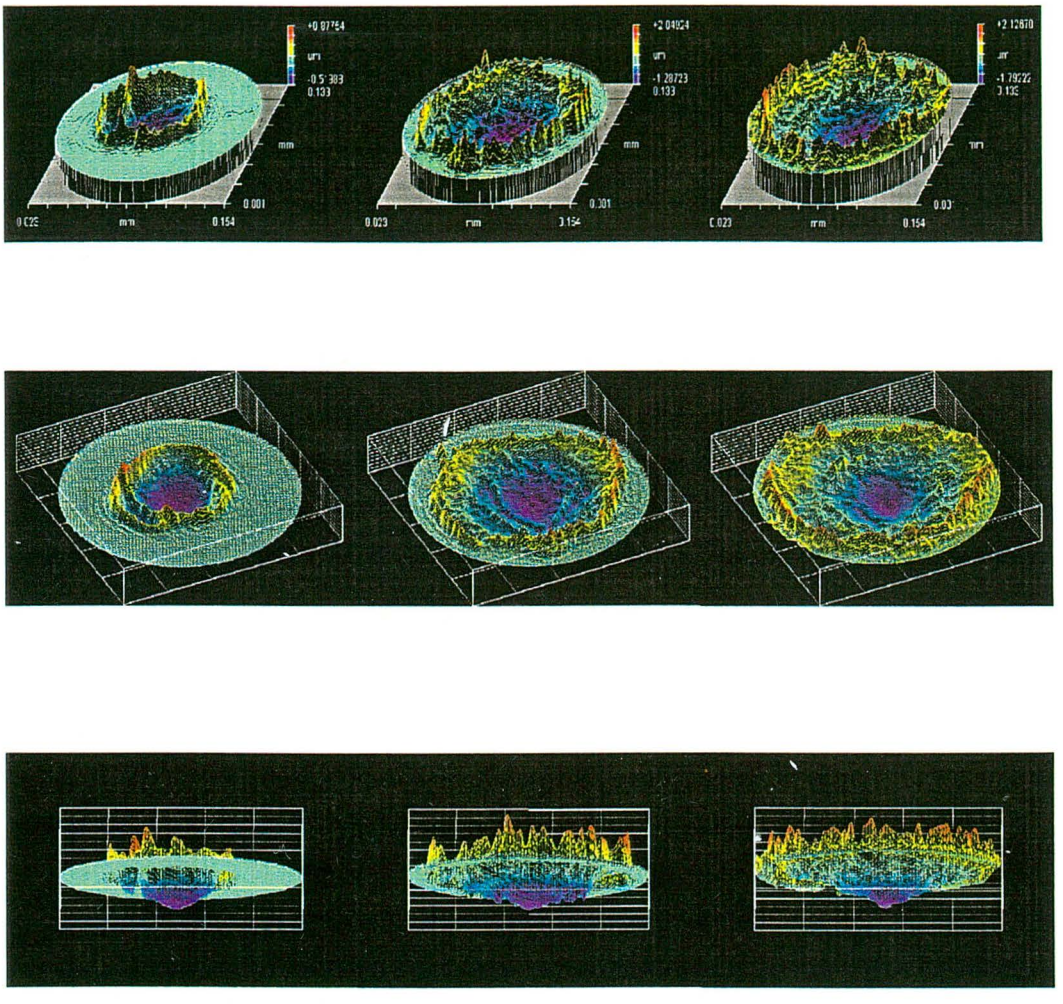

(a) (b) (c)

Figure 2.4 3D White light interferometric microscope images of the craters at various laser irradiances (FWHM = 3 ns): a) 2.6×10^9 W/cm^2, b) 1.2×10^{10} W/cm^2, c) 2.0×10^{10} W/cm^2

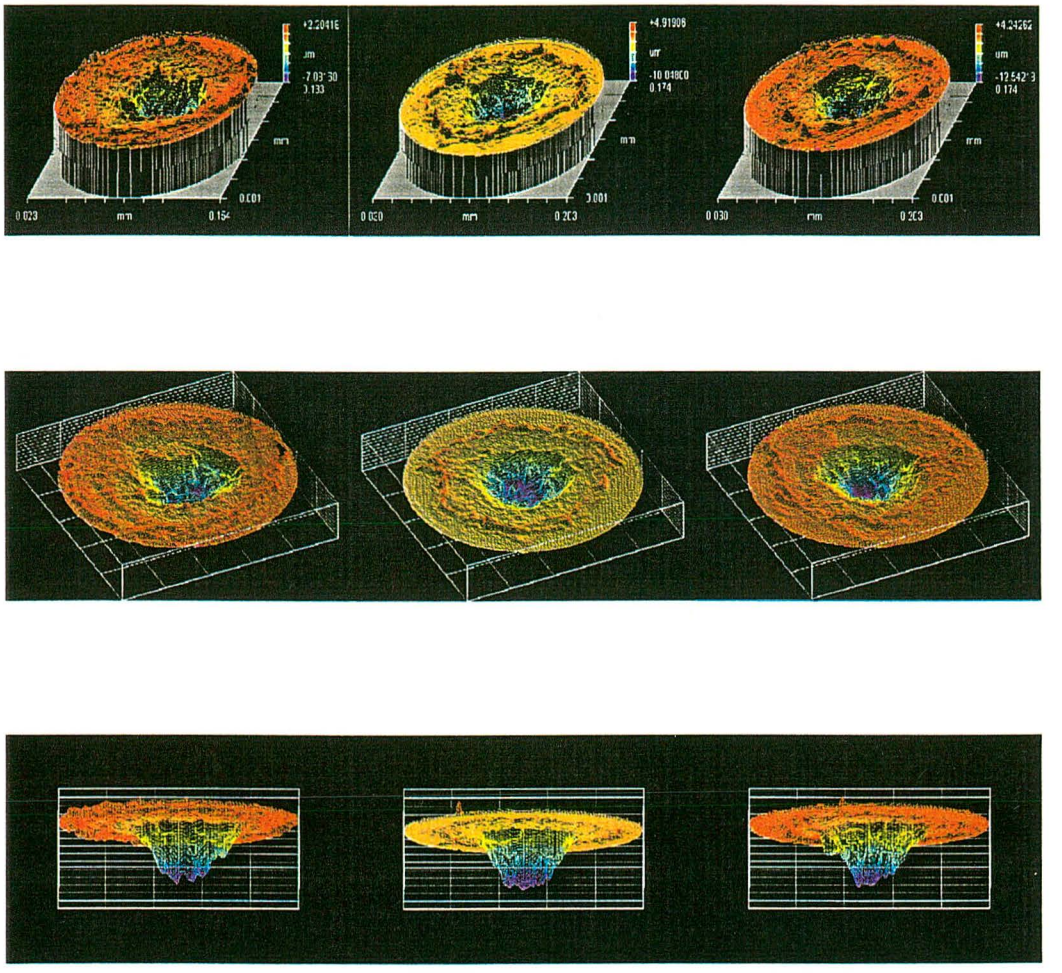

(d) (e) (f)

Figure 2.4 (continued) 3D White light interferometric microscope images of the craters at various laser irradiances (FWHM = 3ns): d) 2.4×10^{10} W/cm^2, e) 3.6×10^{10} W/cm^2, and f) 5.1×10^{10} W/cm^2

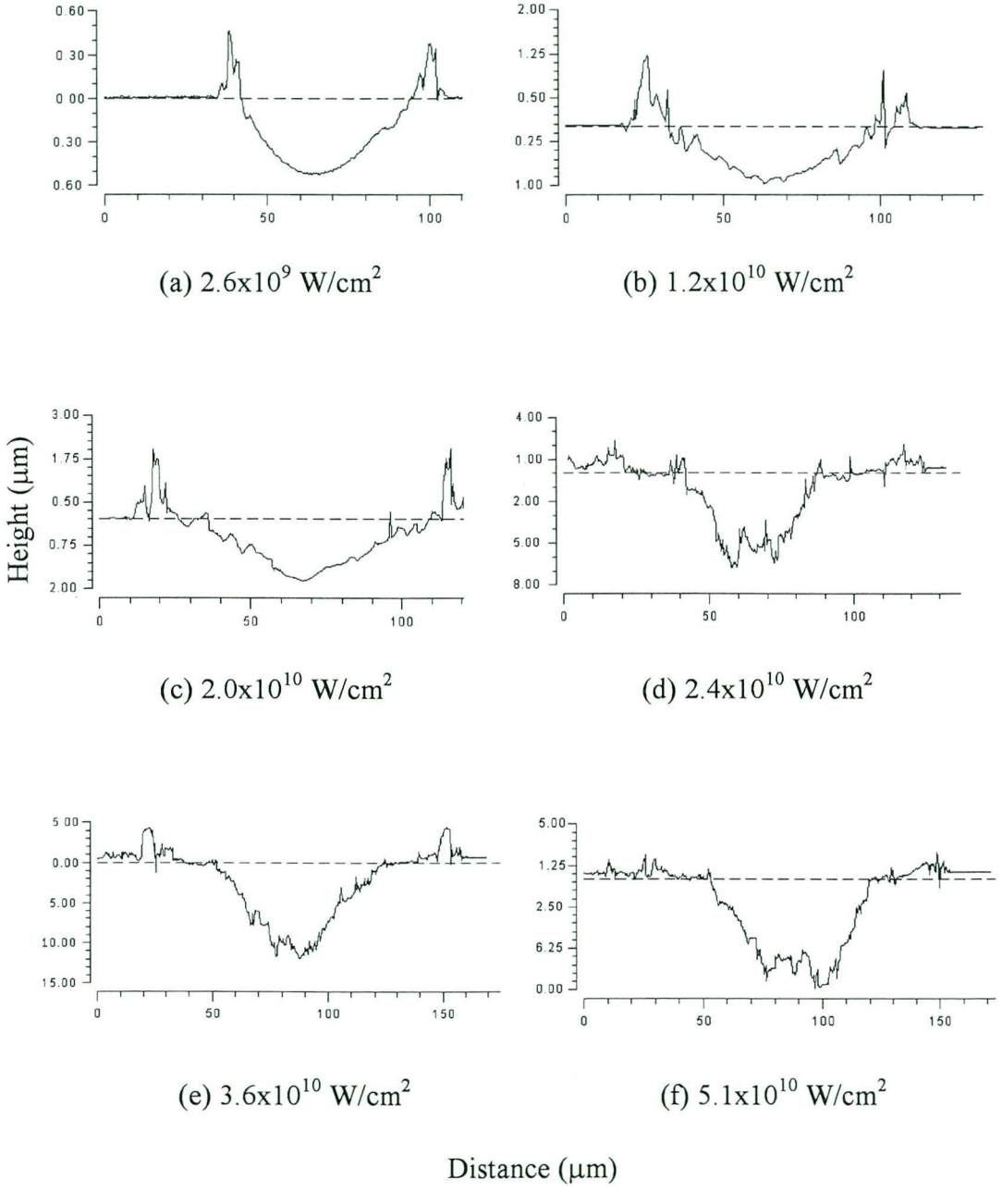

(a) 2.6×10^{9} W/cm^2

(b) 1.2×10^{10} W/cm^2

(c) 2.0×10^{10} W/cm^2

(d) 2.4×10^{10} W/cm^2

(e) 3.6×10^{10} W/cm^2

(f) 5.1×10^{10} W/cm^2

Figure 2.5 Cross sectional view of the craters at various laser irradiances (FWHM = 3 ns): a) 2.6×10^{9} W/cm^2, b) 1.2×10^{10} W/cm^2, c) 2.0×10^{10} W/cm^2, d) 2.4×10^{10} W/cm^2, e) 3.6×10^{10} W/cm^2, and f) 5.1×10^{10} W/cm^2

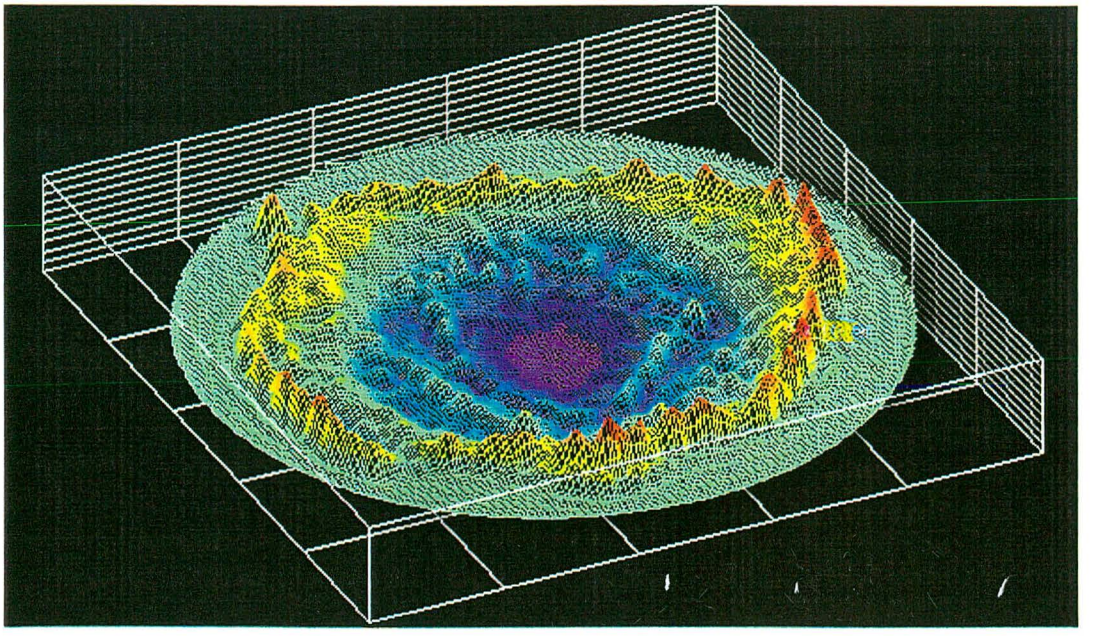

Figure 2.6 Enlarged 3-D image of crater produced at 1.2×10^{10} W/cm^2

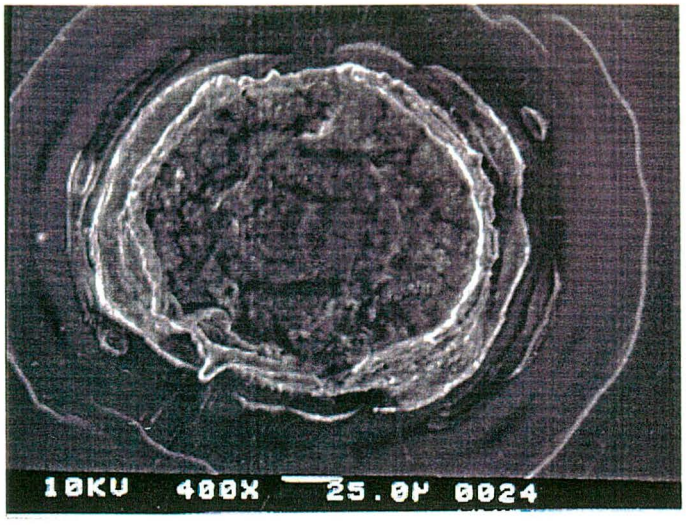

(a)

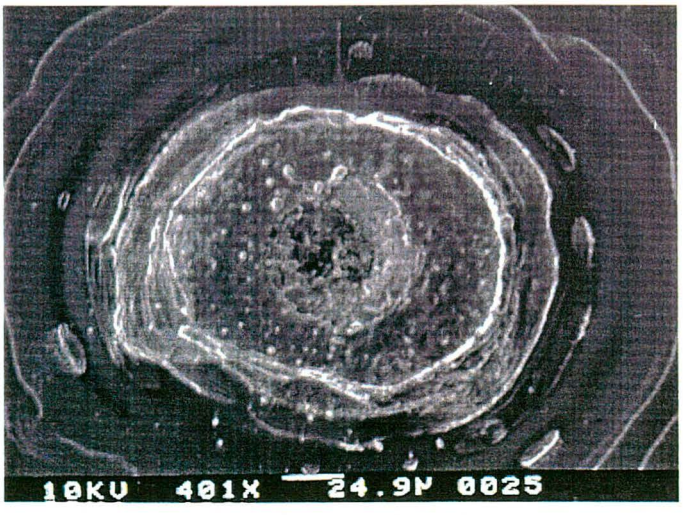

(b)

Figure 2.7 SEM images of the crater for a) laser irradiance slightly below the explosive boiling threshold and b) laser irradiance slightly above the threshold. The focused laser spot size was 50 μm

sample surface and the surrounding ambient. At approximately 2.2×10^{10} W/cm^2, a different crater structure is produced (note the change in scale in the figures). The shape is now characterized by a deep hole near the center of the crater, a thermally affected area that surrounds the deep hole, and a rim at the very edge of the crater (Figure 2.5 (d), (e), and (f)). Unlike the smooth crater bottom observed for laser irradiances below 2.2×10^{10} W/cm^2, the bottom of the crater is now rough with several local peaks and valleys. In the region surrounding the deep hole, many micron-sized droplets are present (Figure 2.7). Additional droplets can be seen on the surface, in regions beyond the rim of the craters.

Figures 2.8 shows the measured crater volume and depth as a function of irradiance. The crater depth and volume undergo a dramatic increase at the irradiance of $\approx 2.2 \times 10^{10}$ W/cm^2. As the irradiance is increased from 1.9×10^9 to 2.2×10^{10} W/cm^2, the crater depth increases gradually from 0.4 to 1.8 μm. At 2.2×10^{10} W/cm^2, the crater depth abruptly increases from 1.8 to 6 μm (Figure 2.8), more than a three-fold increase in the ablation depth. From 2.2×10^{10} to 9.5×10^{10} W/cm^2, the crater depth increases rapidly from 6 to 19 μm. Due to the sudden change in the crater morphology to the deep structure, the crater volume also increases abruptly at this laser power density for both laser spot sizes.

In order to check pulse-to-pulse repeatability of the measured crater depth and volume, several single pulse ablation tests were conducted on fresh sample sites at the same energy fluence (fluence variation less than 0.9%). Below 2.2×10^{10} W/cm^2, the variation in the measured crater volume and the depth was

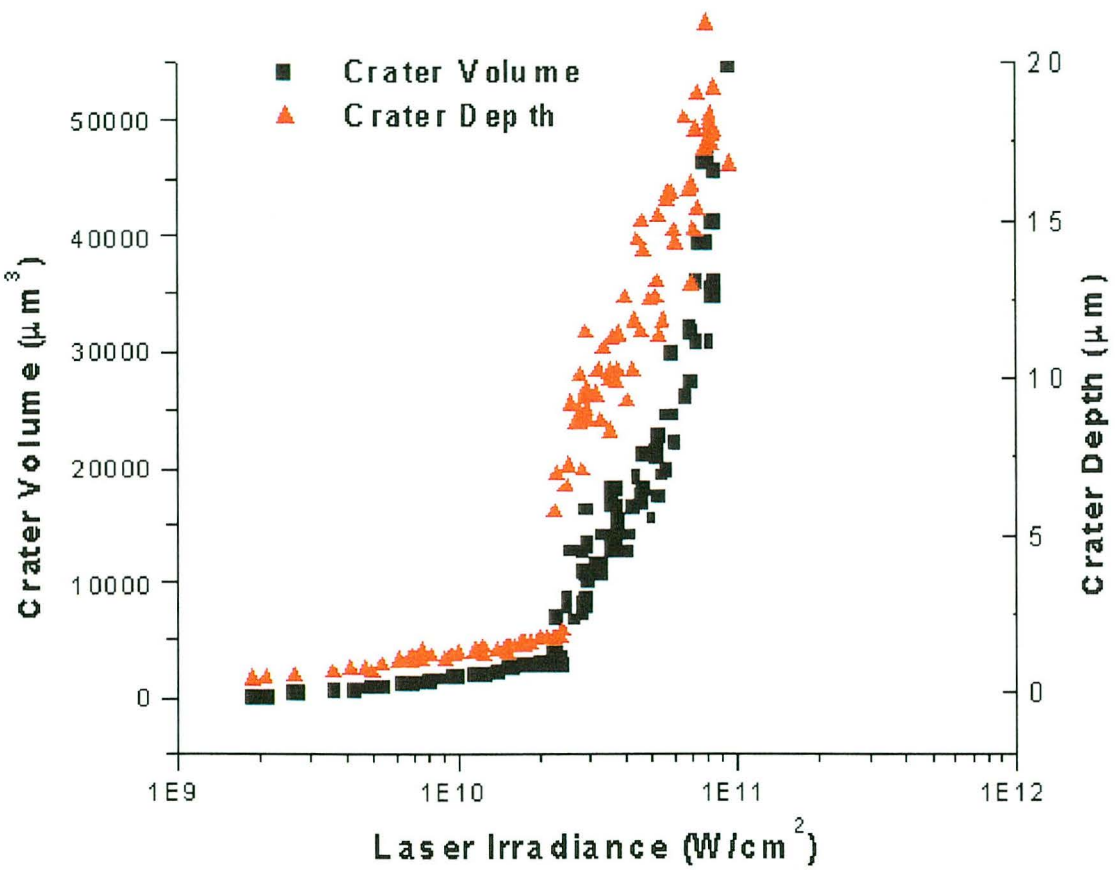

Figure 2.8 Crater volume and depth as a function of laser irradiance

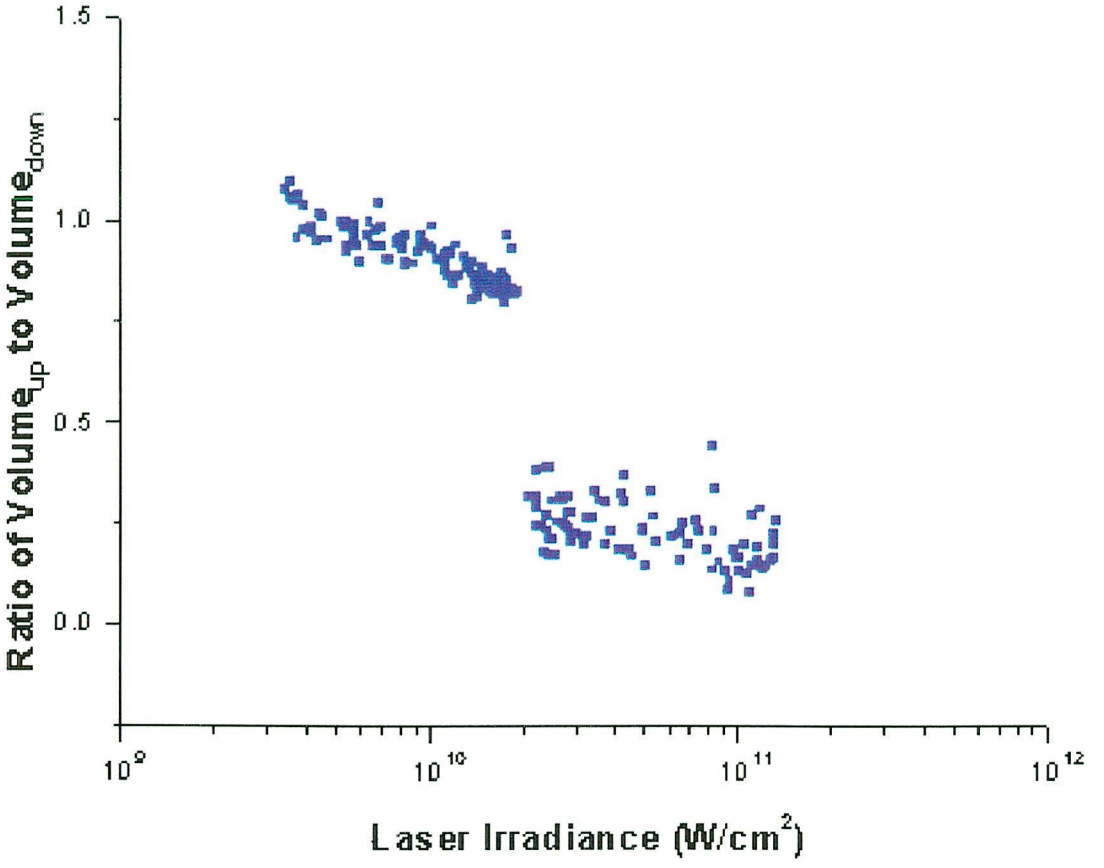

Figure 2.9 The ratio of Volume$_{up}$ to Volume$_{down}$ as a function of the laser power irradiance

approximately 2% and 4%, respectively. However, above 2.2×10^{10} W/cm^2, the pulse-to-pulse variation in depth and volume exceeded 20%. The highest fluctuation in these parameters occurred over the irradiance range from 2.2×10^{10} to 3.0×10^{10} W/cm^2. In this irradiance range, each crater was splattered with resolidified molten mass; the amount varied causing a large variation in the measured volumes and depths.

Figure 2.9 shows the ratio of the volume of mass above ($Volume_{up}$) the original silicon surface (crater rim) to the volume of mass removed from the crater ($Volume_{down}$). This ratio also shows a significant change at $\approx 2.2 \times 10^{10}$ W/cm^2. For laser irradiance from 1.0×10^9 to 4.0×10^9 W/cm^2, the ratio of $Volume_{up}$ to $Volume_{down}$ remains near unity. A ratio close to 1 suggests that the crater might be mainly formed by "washing out" [2] molten silicon from the irradiated zone with subsequent resolidification at the crater edge, forming the rim. With increasing irradiance, this ratio shows a modest decrease, which may be attributed to increased evaporation at increased laser irradiances. However, at 2.2×10^{10} W/cm^2, the ratio decreases sharply, indicating significant net mass removal from the silicon surface. These data on crater properties suggest the initiation of a different mechanism or a shift in the primary mechanism responsible for mass removal at the threshold irradiance of 2.2×10^{10} W/cm^2.

2.4 Conclusions

In this chapter, mass removal from the silicon sample during high laser irradiance was investigated by studying the morphology and the volume of the resulting crater with a whitelight interferometric microscope. A dramatic change in the crater morphology at $\approx 2.2\text{x}10^{10}$ W/cm^2 (FWHM = 3 ns) suggests two distinct ablation regimes. Below $2.2\text{x}10^{10}$ W/cm^2, the crater morphology showed clear signs of surface melting. The formation of the molten silicon and its subsequent solidification around the edge of the crater appears to be responsible for the formation of the rim. In addition, the circular ripples and wavy structures inside the crater, which may result from the motion and solidification of the molten silicon, further indicate the presence of the molten silicon during laser heating. In this laser irradiance regime, the relevant ablation mechanisms may include surface vaporization and hydrodynamic instability of the molten layer as well as the recoil pressure of the evaporating vapor, which could act to "flush out" the molten silicon. At $2.2\text{x}10^{10}$ W/cm^2, there is a drastic increase of mass removal, evidenced by a sharp jump in the ablation depth and volume. The sudden change in the crater morphology to a deep structure signifies a shift in the primary mechanism for mass removal at this irradiance. The new ablation mechanism was very efficient in removing the mass from the sample, causing more than a three-fold increase in the ablation depth at the onset, followed by rapid growth above the threshold irradiance. The remaining chapters of the dissertation are devoted to additional experimental investigations and analysis to identify the ablation mechanism that greatly enhances mass removal above $2.2\text{x}10^{10}$ W/cm^2 for silicon samples.

REFERENCE

1. W.W. Duley: UV Lasers: Effects and Applications in Materials Science (Cambridge University Press, Cambridge, 1996)
2 M. Von Allmen: Laser Beam Interactions with Materials (Springer, Heidelberg, 1987)
3. W. Kautek, B. Roas, and L. Schultz: Thin Solid Films **191**, 317 (1990)
4. H. Habermeier, G. Beddies, B. Leibold, G. Lu, and G. Wagner: Physica C **180**, 17 (1990)
5. T.D. Bennett, D.J. Krajnovich, C.P. Grigoropoulos, P. Baumgart, and A.C. Tam: Journal of Heat Transfer **119**, 589 (1997)
6. H. Varel, D. Ashkenasi, A. Rosenfeld, M. Wahmer, and E.E.B. Campbell: Applied Physcis A **65**, 367 (1997)
7. C. Momma, S. Nolte, B.N. Chichkov, F.v. Alvensleben, and A. Tunnermann: Applied Surface Science **109/110**, 15 (1997)
8. P. Simon and J. Ihlemann: Applied Surface Science **109/110**, 25 (1997)
9. M. A. Shannon, X. Mao, A. Fernandez, W.T. Chan, and R. E. Russo: Analytical Chemistry **67**, 4522 (1995)
10. A. Fernandez, X. L. Mao, W.T. Chan, M. A. Shannon, and R. E. Russo: Analytical Chemistry **67**, 2444 (1995)
11. W.T. Chan and R. E. Russo: Spectrochimica Acta **46B**, 1471 (1991)
12. S.H. Jeong, O. Borisov, J.H. Yoo, X.L. Mao, R.E. Russo: Analytical Chemistry **71**, 5123 (1999)

13. P. Arrowsmith and S.K. Hughes: Appl. Spectrosc. **42**, 1231 (1988)

14. D.J. Figg, J.B. Cross, and C. Brink: Applied Surface Science **127 – 129**, 287 (1998)

15. J.C. Miller and R.F. Haglund, Jr. : Laser Ablation Mechanisms and Applications (Springer, Heidelberg, 1991)

16. X. Zhang, S.S. Chu, J.R. Ho, and C.P. Grigoropoulos: Applied Physics A **64**, 545 (1997)

17. A.B. Brailovsky, S.V. Gaponov, and V.I. Luchin: Applied Physics A **61**, 81 (1995)

18. T.D. Bennett, C.P. Grigoropoulos, and D.J. Krajnovich: J. Appl. Phys. 77(2), 849 (1995)

19. S. Gogoll, E. Stenzel, M. Reichling, H. Johansen, and E. Matthias: Appl. Surf. Sci. **96 – 98**, 332 (1996)

20. H.K. Park and R.F. Haglund, Jr. : Appl. Phys. A **64**, 431 (1997)

21. R.L. Webb, L.C. Jensen, S.C. Langford, and J.T. Dickinson: J. Appl. Phys. **74**, 2323 (1993)

22. J.T. Dickinson, L.C. Jensen, R.L. Webb, M.L. Dawes, and S.C. Langford: J. Appl. Phys. **74**, 3758 (1993)

Chapter 3

Time-resolved Shadowgraph Imaging of Ejected Mass during High Irradiance Laser Ablation of Silicon

3.1 Introduction

Laser ablation involves non-linear complex and collective processes that are not completely understood. These processes occur over many orders of magnitude in time, from the initial absorption of the laser light by the sample to ejection of the mass from the sample surface. Figure 3.1 illustrates some of the possible processes that may occur during laser-material interaction. The initial laser-material interaction can create excited electrons in the solid, which leads to ejection of some electrons from the sample on the time scale less than a picosecond by means of photoelectric or thermiomic emission [1,2,3,4,5]. The emitted electrons can quickly form air plasma above the sample surface on the picosecond time scale [6]. In the solid, the excited electrons undergo electron-phonon relaxation and the energy is transferred to the lattice. Through lattice vibration, the transferred energy is dissipated from the irradiated zone to the bulk in the form of heat [7,8]. The heat conduction occurs on the time scale of several tens of picoseconds, which is slightly larger than the electron-phonon relaxation process. Following heat conduction into the bulk, melting and vaporization of the sample may be initiated. The molecules leaving the liquid-vapor interface during laser evaporation establish an equilibrium distribution of velocity in a small region above the sample surface called the Knudsen layer as shown in Figure 3.1 [9,10]. Above the Knudsen layer,

the vapor plume can rapidly expand, compressing the ambient gas and forming a shock wave front. In addition, the expanding plume can interact with the latter part of the laser pulse, effectively shielding the laser energy from the sample surface and becoming highly energetic [11,12]. The high temperature vapor plume can also heat the sample surface via radiative heating [13,14]. The vaporization of the sample and the subsequent gas dynamic processes of the expanding plume take place on the time scale of nanoseconds. Other mass removal processes such as exfoliation may occur on the time scale substantially larger than nanoseconds.

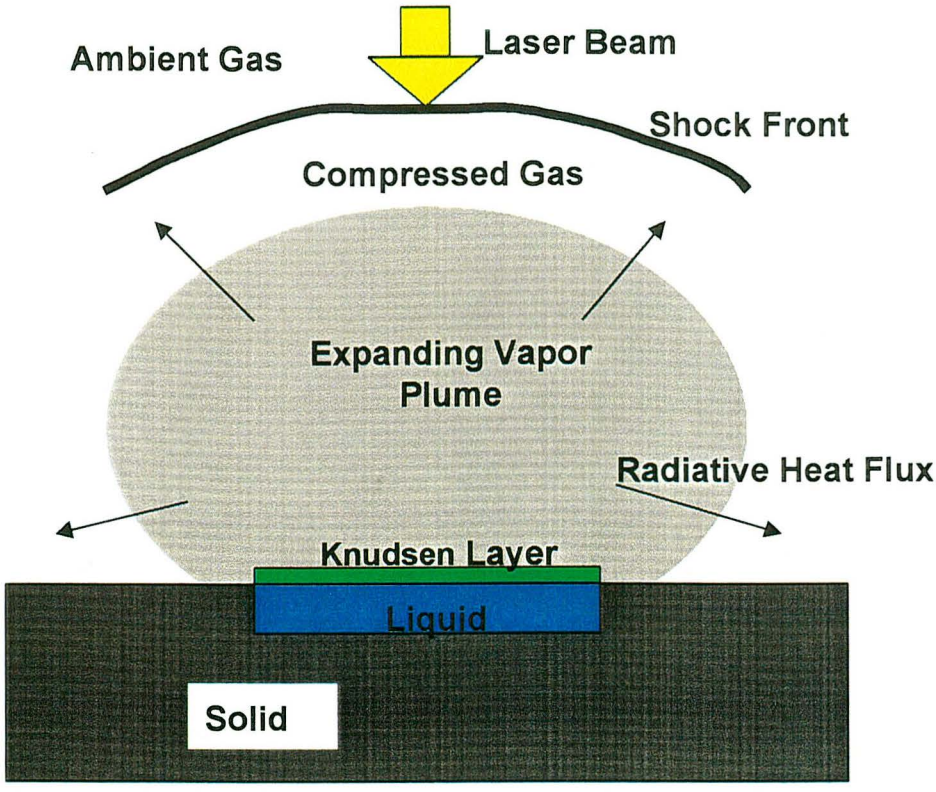

Figure 3.1 Schematic diagram of relevant processes during short pulse laser irradiance

Laser shadowgraph imaging has been a useful experimental technique that has enabled the identification of relevant gas dynamic and mass ejection processes and their corresponding time scales during and after the laser heating. In laser shadowgraph imaging, the pump beam ablates the sample while the probe beam scans the region above the focal spot of the pump beam. The probe beam is then directed to the CCD camera. If the ejected mass is present in the scanned region, the probe light will either be absorbed or scattered, creating shadows on the image recorded by the camera. Mao [6] used the shadowgraph imaging technique to study the early time air plasma formed by the emitted electrons from the copper sample during picosecond laser ablation. Also using this technique, Kelly [15,16] and Srinivasan [17,18] studied the shock wave structure and gas dynamic behavior of ejecta during nanosecond laser ablation of polymer sample.

In the previous chapter, we identified the threshold irradiance during nanosecond laser ablation of silicon samples, at which a dramatic increase in mass removal occurs. This drastic change in the mass removal with respect to the laser irradiance indicates a fundamental change in the primary ablation mechanism at this irradiance. In order to better understand mechanisms which may be responsible for enhanced mass removal, the laser shadowgraph imaging was used to obtain time-resolved information for vapor plume dynamics and mass ejection from the sample surface at irradiances below and above the threshold. In addition, laser shadowgraphy was used to approximately estimate size of the ejected mass and to infer the time scale for the onset of mass ejection. This chapter describes

experimental results that characterize the mass ejection process that cause enhanced mass removal above the threshold irradiance. The knowledge obtained from this experimental work forms the basis for the analysis of the phenomena in Chapter 4.

3.2 Experimental System

3.2.1 Shadowgraph imaging for nanosecond laser ablation of silicon

Figure 3.2 shows the experimental schematic diagram for shadowgraph imaging of the ejected mass for nanosecond laser ablation of silicon. The delivery of the pump beam (or ablation) beam to the silicon sample was described in detail in the previous chapter. Very briefly, an Infinity 40-100 Nd-YAG laser (FWHM = 3 ns) emits a beam at 266 nm. The beam passes through the pinhole spatial filter and is focused on the silicon sample using a beam splitter (BS 2, R = 50) and a plano-convex quartz lens (f = 20 cm).

A Continuum YG601 Nd-YAG laser (FWHM = 35 ps) was used as a probe beam for the laser shadowgraph imaging of mass ejection from the silicon surface. The 532 nm wavelength probe beam was aligned parallel to the silicon surface and perpendicular to the ablation beam using two mirrors. A polarizing glass filter was placed between two mirrors to adjust the intensity of the probe beam before the CCD camera (Photometrics Model CH250/A). A narrow-band filter centered at the probe laser wavelength was placed in front of the CCD camera shutter to block the plume radiation. The time interval between the ablation pulse and the probe pulse is controlled by adjusting the trigger delay using a four channel digital delay/ pulse

generator (Stanford Research Systems, Model DG535). To measure the time delay between the probe and the ablation pulse, a part of the beam was delivered to a fast UV photodiode using a beam splitter (BS 1 or BS 3) placed in each beam path. By measuring the time difference between two photodiode signals with a digital oscilloscope (Tektronix Model DSA 602A), the time delay of the probe pulse with respect to the ablation beam was obtained. At each selected laser irradiance, time resolved images of mass ejection above the silicon surface were acquired by varying the delay from 5 ns to 30 μsec. Due to the jitter time associated with triggering the probe pulse (~500 ns), it was not possible to obtain a sequence of time-resolved images with a high degree of time resolution at times less than 500 ns.

3.2.2 Shadowgraph imaging for picosecond laser ablation of silicon

The drastic change of the crater morphology into the deep structure was also observed for picosecond laser ablation of silicon at $\lambda = 1064$ nm. Due to the jitter time associated with triggering the probe beam, the early time imaging of ejecta gas dynamics just after the laser pulse was not possible for nanosecond pulse ablation. The problem of jitter time with triggering the probe beam was eliminated in the picosecond study by varying the optical path of the probe beam in controlling the timing between the pump and the probe beam. Having more precise control on specifying the time delay between two pulses with a time resolution better than 10 ps, the shadowgraph imaging was used to study the ejecta gas dynamics during the

early stage of the expansion and to check the possibility of large particulate ejection at times just after the laser pulse.

Figure 3.3 shows the schematic diagram for the shadowgraph imaging set-up used for studying picosecond laser ablation. The ablation beam is emitted by a Continuum Nd:YAG laser (model YG601) at the fundamental wavelength of 1064 nm. The pulse duration of the laser beam was 35 ps (FWHM). The beam was delivered to the sample surface using multiple mirrors and focused using a quartz plano-convex lens (f = 20 cm). The focused beam size was approximately 80 μm. The probe beam is also emitted by the same laser at the laser wavelength of 532 nm by using second harmonic generation. After passing through the polarizer that adjusts the intensity of the beam for CCD, the probe beam is directed to optical mirrors situated on the movable stage. The time delay between the pump (ablation) and the probe pulse was adjusted by translating the stage, which effectively alter the optical path of the probe beam. The light travels at a speed of 3.0×10^{10} cm/s and translation of the stage by 1 mm results in a difference of 6.67 ps in terms of the time delay between the probe and the pump beam. The maximum time delay between the two beams was approximately 3 ns. The ejected mass is scanned with the probe beam, which is aligned parallel to the sample surface, and its shadowgraph was recorded with a CCD camera (Photometrics AT200). In each imaging experiment, the zero time delay is defined as the time when peaks of the pump and the probe beam overlaps with each other.

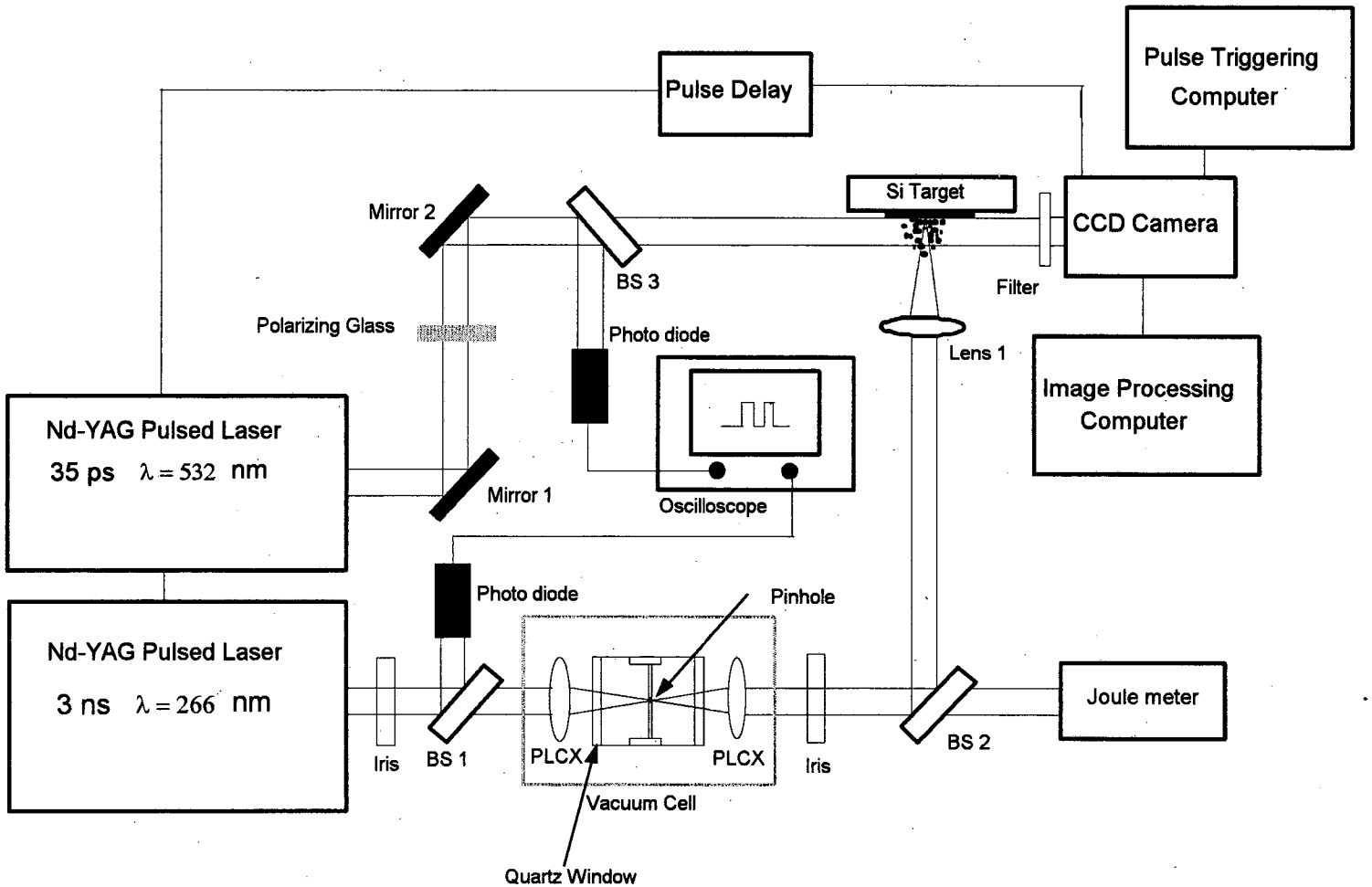

Figure 3.2 Schematic diagram for shadow graph imaging of the ejected mass from the sample surface for nanosecond laser ablation of silicon

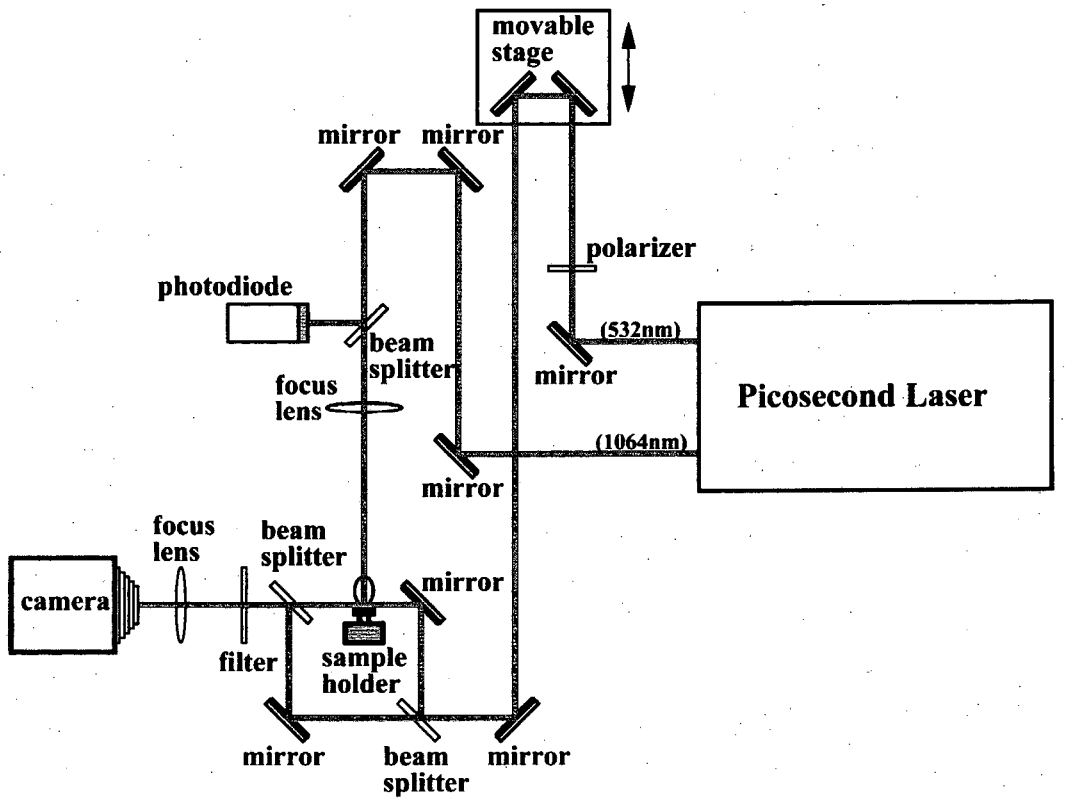

Figure 3.3 Laser shadowgraph imaging schematic for early time ejecta gas dynamics during picosecond laser ablation of silicon

3.3 Results and Discussion

3.3.1 Ejection of large particulates above the threshold irradiance for nanosecond ablation of silicon

Time-sequenced images of ejected mass at selected laser irradiances were measured using laser shadowgraphy, covering a region of ≈ 500 μm in front of the target surface. These images reveal that the formation of the deep crater structure produced at irradiances ≈ 2.2×10^{10} W/cm^2 and above is accompanied by a violent ejection of liquid droplets. Images of the ejected mass were obtained at irradiances of 1.9×10^{10}, 3.9×10^{10}, and 8.7×10^{10} W/cm^2, which are slightly below, slightly above, and well above the threshold irradiance of 2.2×10^{10} W/cm^2. The laser-beam spot size at the silicon surface was 50 μm for all three experiments. Figure 3.4 shows the time sequenced images for 1.9×10^{10} W/cm^2. The first image at t = 10 ns shows the shockwave propagation into the ambient air, which is just after the laser pulse, (3 ns). The shockwave is formed due to compression of the ambient air as high pressure vapor plume expands against the ambient air during the laser pulse [14,19]. The propagation of the shockwave away from the surface was seen until t ~ 200 ns. Afterwards, images taken at times up to 30 μs reveal no measureable mass ejection from the surface.

Figure 3.5 shows the time resolved images for ablation at irradiance of 3.9×10^{10} W/cm^2. As in Figure 3.4, shock wave propagation is observed shortly after the laser pulse. The speed of the shock wave is significantly faster than that observed at 1.9×10^{10} W/cm^2; the shock wave reaches at a distance of 500 μm above

the sample surface at t = ~70 (versus ~200 ns for the smaller irradiance of 1.9×10^{10} W/cm^2). Approximately 400 ns after the laser pulse, mass leaving the silicon surface begins to appear. Approximately 1 μs after the pulse, the images clearly show the ejection of molten or solid particulates. The ejection of these particulates continued for about 30 μs. A precise determination of the ejected particulate size is difficult due to the presence of diffraction rings around the particles in the images. Larger particles will have fewer diffraction rings and a sharper boundary; the size of the large particles is estimated to be approximately 10 microns.

Figure 3.6 shows images for ablation at 8.9×10^{10} W/cm^2. Just after the end of the laser pulse at 3ns, the shock wave is distorted from the hemispherical shape observed at lower irradiances. At about 40 ns, the distorted front transforms into a triangular shape and has already reached the distance of 500 μm from the sample surface. The distortion of the shock-wave front may be due to the interaction between the dense plasma above the sample surface with the latter part of the laser pulse. The dense plasma region created by the initial part of the laser pulse expands in both transverse and longitutidional directions. When the plasma expanding in the directon of the incoming laser beam strongly absorbs the latter part of the beam, high kinetic energy and high pressure can result in the absorbing region [17]. The high pressure can produce additional shock waves, causing the bulge seen in Figure 3.6 at the center of the shock front at 5 ns.

At the irradiance of 8.9×10^{10} W/cm^2, a greater number of large particulates was observed. Similar to the 3.8×10^{10} W/cm^2 case, ejection of particulates was delayed

for ≈ 400 ns after the start of the laser pulse; vigorous ejection of the particulates occurred at μs times and continued for ≈ 30 μs. The size of the large particulates was estimated to be approximately 25 ~ 30 microns. In general, for other laser irradiances above the threshold value, approximately the same time delay (~ 300 to 400 ns) was observed for large particulate ejection to begin.

3.3.2 Early time shadowgraph imaging of the air plasma and vapor plume during picosecond laser ablation of silicon

The drastic change of the crater morphology at a threshold irradiance discussed in Chapter 2 was also observed for picosecond laser ablation (pulse width = 35 ps) of silicon at $\lambda = 1064$ nm. Figure 3.7 shows the crater depths as a function of laser irradiance for several beam sizes. For all beam sizes, the craters exhibit the deep structure at a threshold of 2.1×10^{12} W/cm^2. Above this threshold irradiance, the crater depth shows a rapid increase with respect to increasing laser irradiance. Time resolved imaging up to 3 ns after the initiation of laser heating was carried out at three laser irradiances: 1.9×10^{12}, 6.0×10^{12}, and 9.8×10^{12} W/cm^2 which represent irradiances just below , modestly above, and well above the threshold value. The shadowgraph images at these three irradiances reveals that different types of plumes dominate at different time scales. For very early times typically less than 200 ps, a conical-shaped air plasma was mainly observed. For times longer than 1ns, a hemispherical vapor plume dominated the air plasma. At times between approximately 200 ps to 1 ns, the plume has a shape of a cone with a

bulging base when both the air plasma and hemispherical vapor plume at its early expansion are important. The extent of the lateral and transverse expansion of the plume varies with the laser irradiance. Large particulate ejection, as seen during nanosecond ablation, was not observed at any irradiances for times less than 3 ns. This suggests that the large particulate ejection (which occurs above the threshold irradiance and is responsible for the deep structure of the crater) may occur on a time scale much larger than 3 ns for picosecond ablation of silicon.

Figure 3.8 shows time-sequenced images of plume expansion dynamics at 1.9×10^{12} W/cm^2. The image just before the end of the laser pulse at t = 35 ps shows a hazy region above the sample surface, which develops into a conical structure at later times (seen at t = 67 ps). This conical structure is air plasma created by the electrons emitted from the sample surface. The electrons in the samples are emitted when they absorb one or more incident photons (multiphoton absorption) to overcome the ionization potential (photoelectric effect). They can also be emitted when their kinetic energy resulting from heating of the sample becomes large enough to overcome the surface energy barrier (thermiomic effect) [2,20]. The emitted electrons can ionize ambient air by the inverse Bremsstrahlung process. As a result, more electrons are formed for further ionization of the ambient air, leading to a cascade break down and formation of the air plasma [6,20]. Expansion of the air plasma in both the transverse and longitudinal directions is seen for times up to several hundred picoseconds later. Starting at approximately t = 300 ~ 400 ps, additional structure develops near the sample surface and evolves

at a time close to a nanosecond into a hemispherical structure. The hemispherical structure that forms after the conical air plasma is a vapor plume, which consists of ejected atoms by desorption and evaporating vapor from the molten mass [6,20]. For times greater than 2 ns, attenuation of the air plasma and significant expansion of the hemispherical vapor plume are observed.

Figure 3.9 and 3.10 show images taken at irradiances of 6.0×10^{12} and 9.8×10^{12} W/cm^2, with both above the threshold value at which the crater transforms into a deep structure. Similar to Figure 3.8, for time less than 200 ps, the plume dynamics is mainly described by formation of an air plasma and its subsequent expansion. Two figures show that while the transverse expansion of the air plasma is observed well after 500 ps, the longitudinal expansion seems to halt at about 150 ps after the peak of the 35 ps laser pulse. Mao at el. [6,20,21] attributes this suppression of the longitudinal expansion of the air plasma to the effects of strong electric field that is developed above the target surface. The electrons emitted from the sample cause the surface to attain an electrically positive charge. Thus, an electric field is established between the electrically positive sample surface and the electrically negative electrons above the sample surface. The field exerts a net force on the emitted electrons in the direction towards the sample surface and prevents further expansion of the air plasma away from the surface. Mao [6,20,21] observed this suppression of the longitudinal expansion of the air plasma during picosecond laser ablation of copper. Figure 3.9 and 3.10 show a suppression effect is also present for picosecond ablation of silicon. As seen at an irradiance of

1.9×10^{12} W/cm^2, development of a hemispherical vapor plume is observed on a nanosecond time scale. However, at these high irradiance values, the air plasma is still present at the nanosecond time scale, shown as a sharp conical tip protruding from the hemispherical vapor plume front.

The threshold laser irradiance for forming the air plasma was determined to be approximately 9.0×10^{11} W/cm^2. Figure 3.11 shows images of picosecond plumes at two times: 68 ps and 1 ns at various laser irradiances. For 7.0×10^{11} W/cm^2, no conical air plasma is observed at picosecond times. Only a hemispherical vapor plume was observed at nanosecond times (Figure 3.11). However, above 9.0×10^{11} W/cm^2, the figure shows expansion of an air plasma on the picosecond time scale. From the images taken at t = 1 ns, the air plasma is more extended in both longitudinal and transverse directions at higher laser irradiances.

The above shadowgraph imaging results for times upto 3 ns reveal that there was no substantial difference in the mass ejection process at laser irradiances above the threshold irradiance (for drastic increase in the mass removal) compared to irradiances below the threshold. At irradiances both below and above the threshold, the plume at early times consists of an air plasma formed at picosecond times and a hemispherical vapor plume that develops at nanosecond times. This implies that the mass ejection that is responsible for the creation of deep structure in the crater must occur at times that are longer than that associated with the formation of the vapor plume. This trend is consistent with nanosecond ablation

results; the large particulate ejection is initiated at times of several hundreds of nanoseconds and continues for several microseconds

3.4 Conclusions

In this chapter, time-resolved diagnostics of plume and ejected mass was performed using laser shadowgraphy for picosecond and nanosecond laser ablation of silicon to understand the relevant processes that may occur over a range of several orders of magnitude in time. Particularly, laser shadowgraphy was used to identify processes that are present above and absent below a threshold irradiance, which corresponds to a drastic increase in the mass removed. Characterization of the processes that are observed above the threshold irradiance is the key to understanding the fundamental mechanism causing the dramatic increase of mass removed above this value.

From shadowgraph images taken for both picosecond and nanosecond laser ablation of silicon, it was determined that the mass ejection, which caused a deep crater structure for irradiances above the threshold occur at times of about several hundreds of nanoseconds. The early time (< 3 ns) plume images for irradiances both below and above the threshold show a similar plume development for picosecond laser ablation: formation of the air plasma at picosecond times, followed by vapor plume expansion. There were no signs of substantial mass ejection that could have led to formation of deep structures of the crater at these times. It is therefore deduced that for irradiances above the threshold irradiances,

significant mass ejection must occur at times larger than several nanoseconds. For nanosecond laser ablation of silicon, for times less than 100 ns, the shadowgraph images show shockwave propagation caused by compression of the ambient air by the expanding vapor. The significant difference in the mass ejection process between irradiances above and below the threshold value is the large particulate ejection that is initiated at times of 300 ~ 400 ns. The vigorous mass ejection in the form of large droplets continues for several microseconds, and seems to cause the deep structure in the crater. In the next chapter, the mechanism that can account for the experimental results at irradiances above the threshold value is proposed based on a detailed analysis of the phenomena.

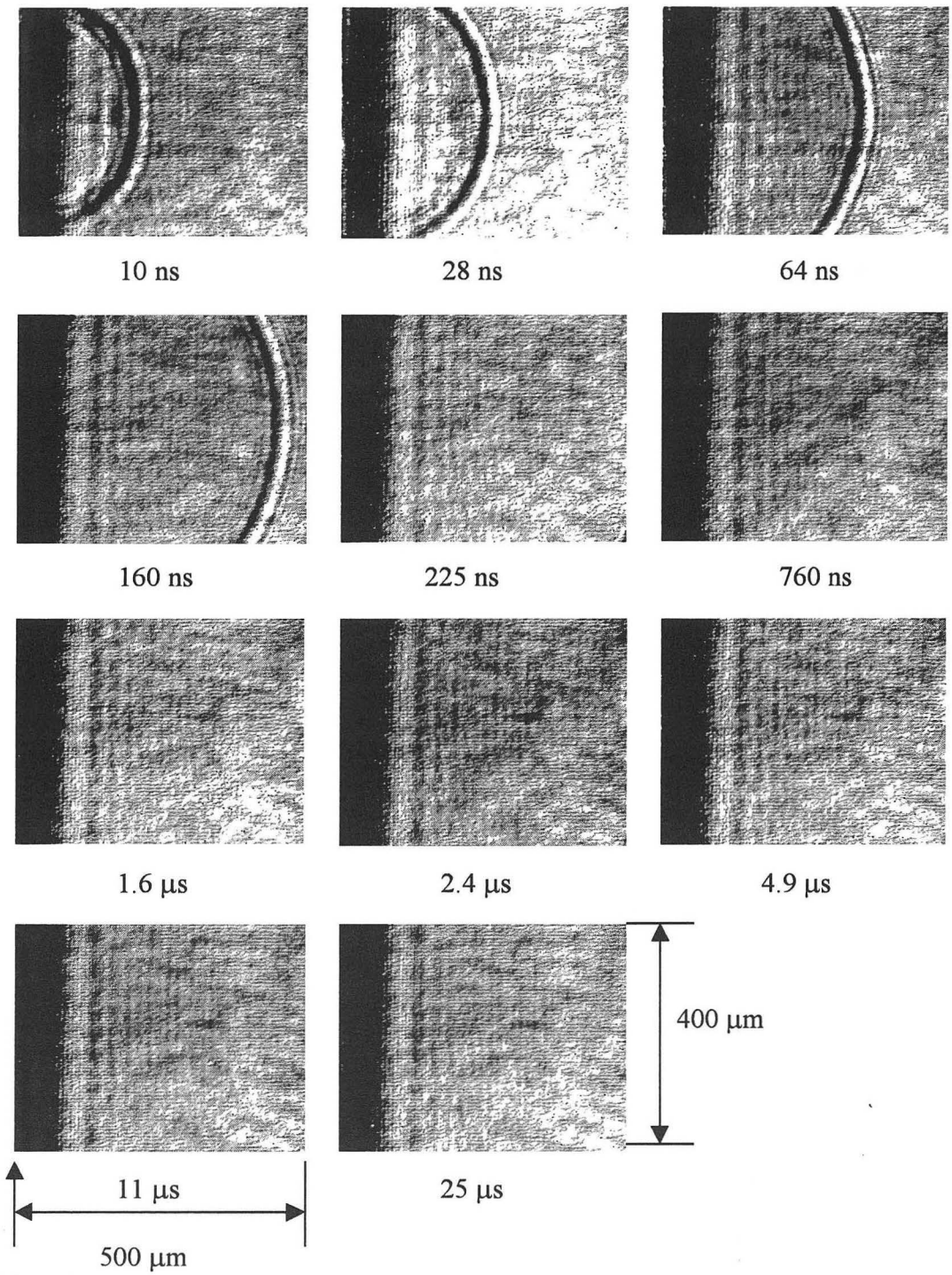

Figure 3.4 Sequence of mass ejection images obtained by laser shadowgraphy for the laser irradiance (FWHM = 3 ns) of 1.9×10^{10} W/cm^2

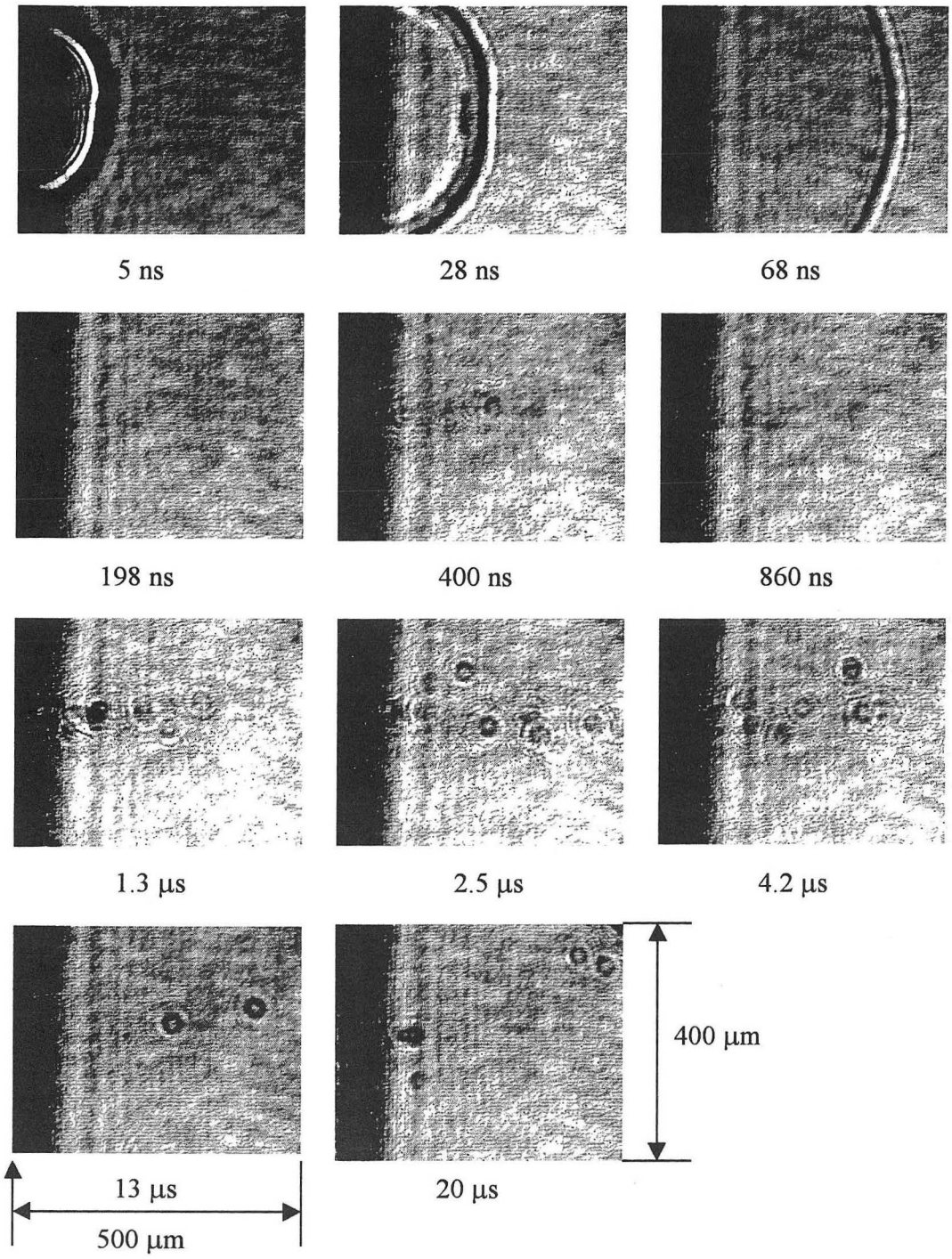

Si surface

Figure 3.5 Sequence of mass ejection images obtained by laser shadowgraphy for the laser irradiance (FWHM = 3 ns) of 3.9×10^{10} W/cm^2

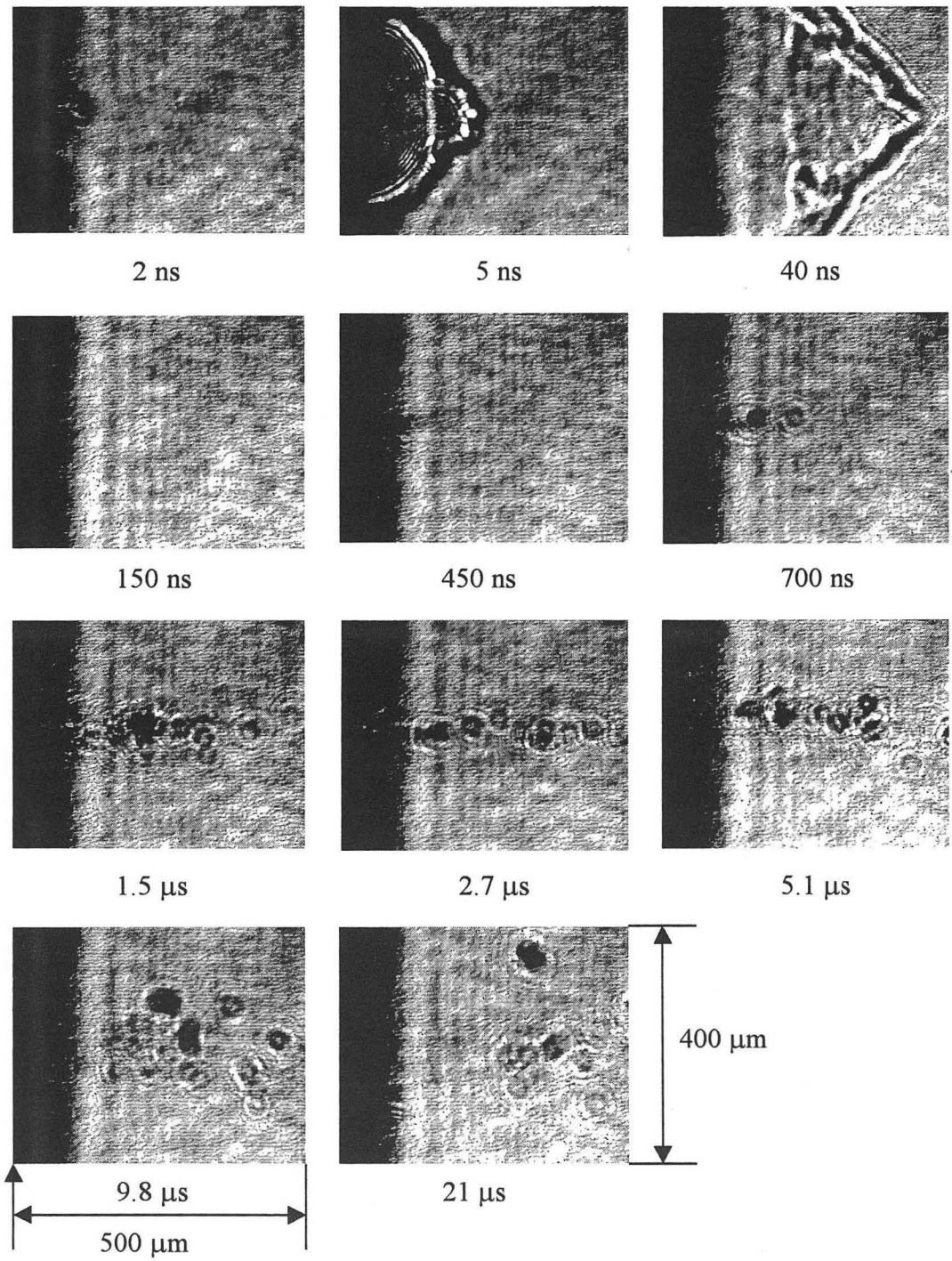

Si surface

Figure 3.6 Sequence of mass ejection images obtained by laser shadowgraphy for the laser irradiance (FWHM = 3 ns) of 8.7×10^{10} W/cm^2

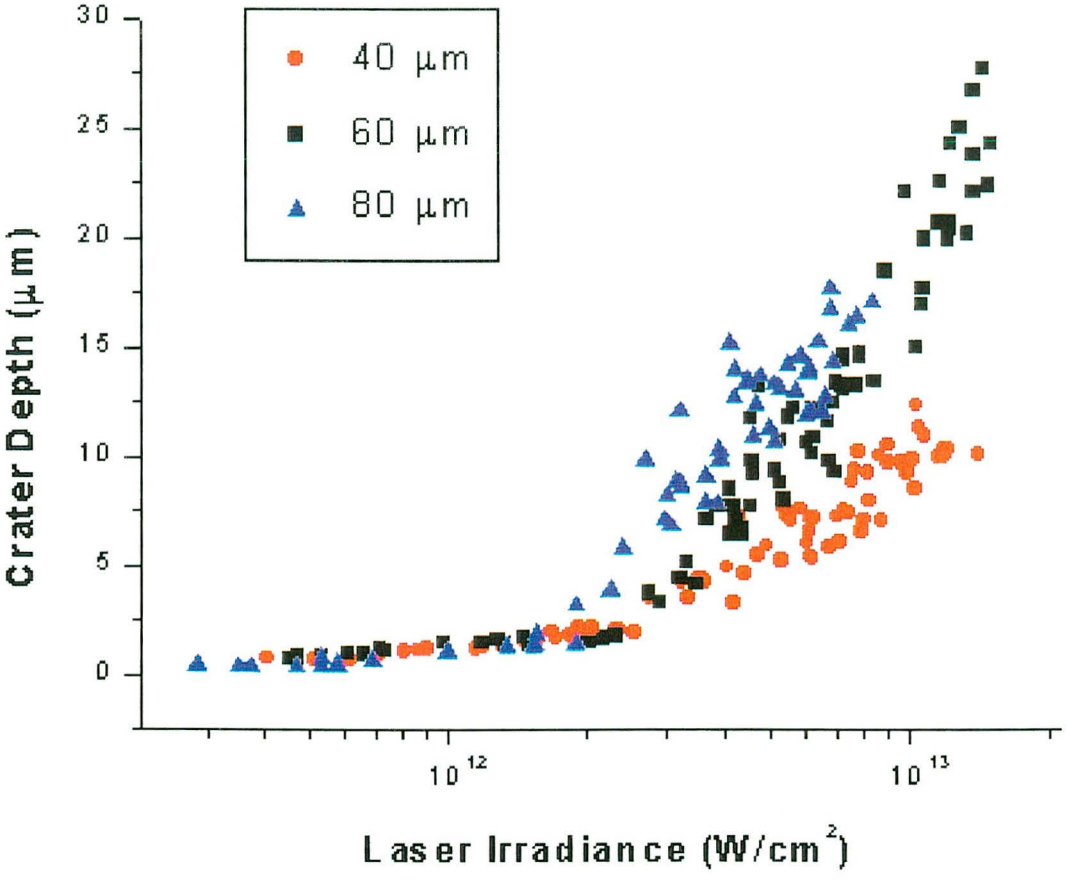

Figure 3.7 Crater depth as a function of laser irradiance for picosecond laser ablation of silicon (FWHM = 35 ps)

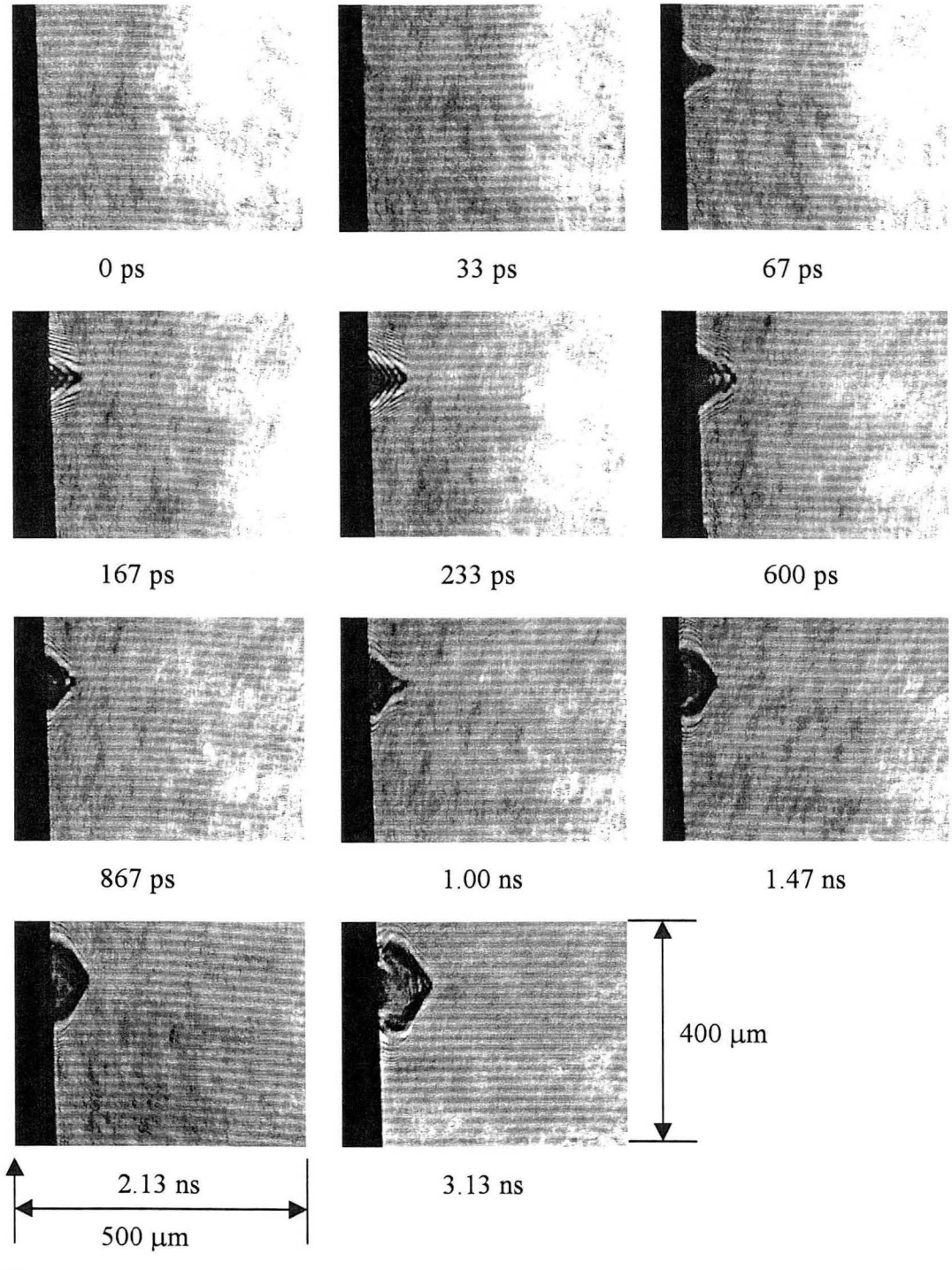

Si surface

Figure 3.8 Time-resolved shadowgraph images of air plasma and vapor plume during picosecond laser ablation (FWHM = 35 ps) of silicon at 1.9×10^{12} W/cm^2

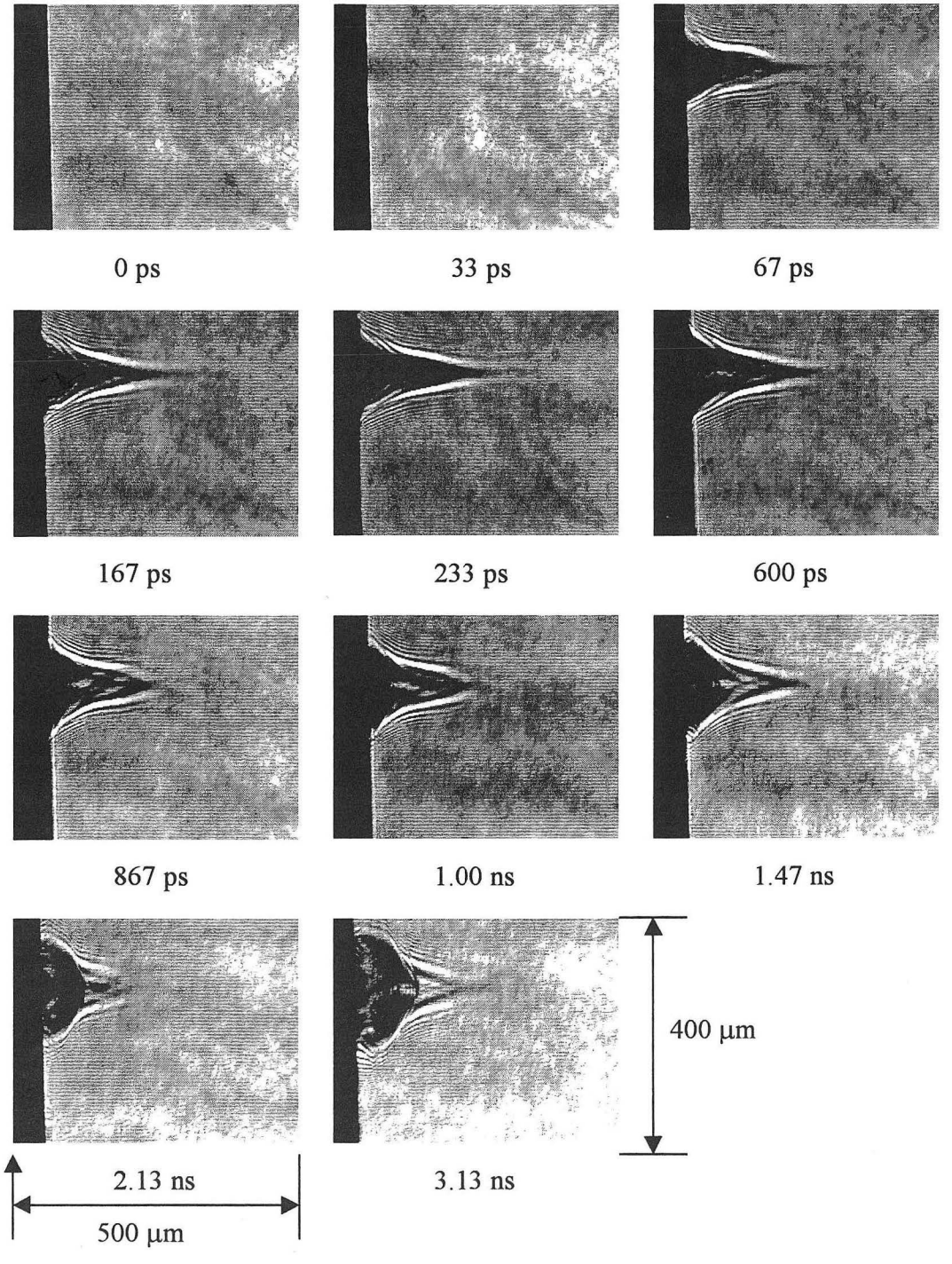

Si surface

Figure 3.9 Time-resolved shadowgraph images of air plasma and vapor plume during picosecond laser ablation (FWHM = 35 ps) of silicon at 6.0×10^{12} W/cm^2

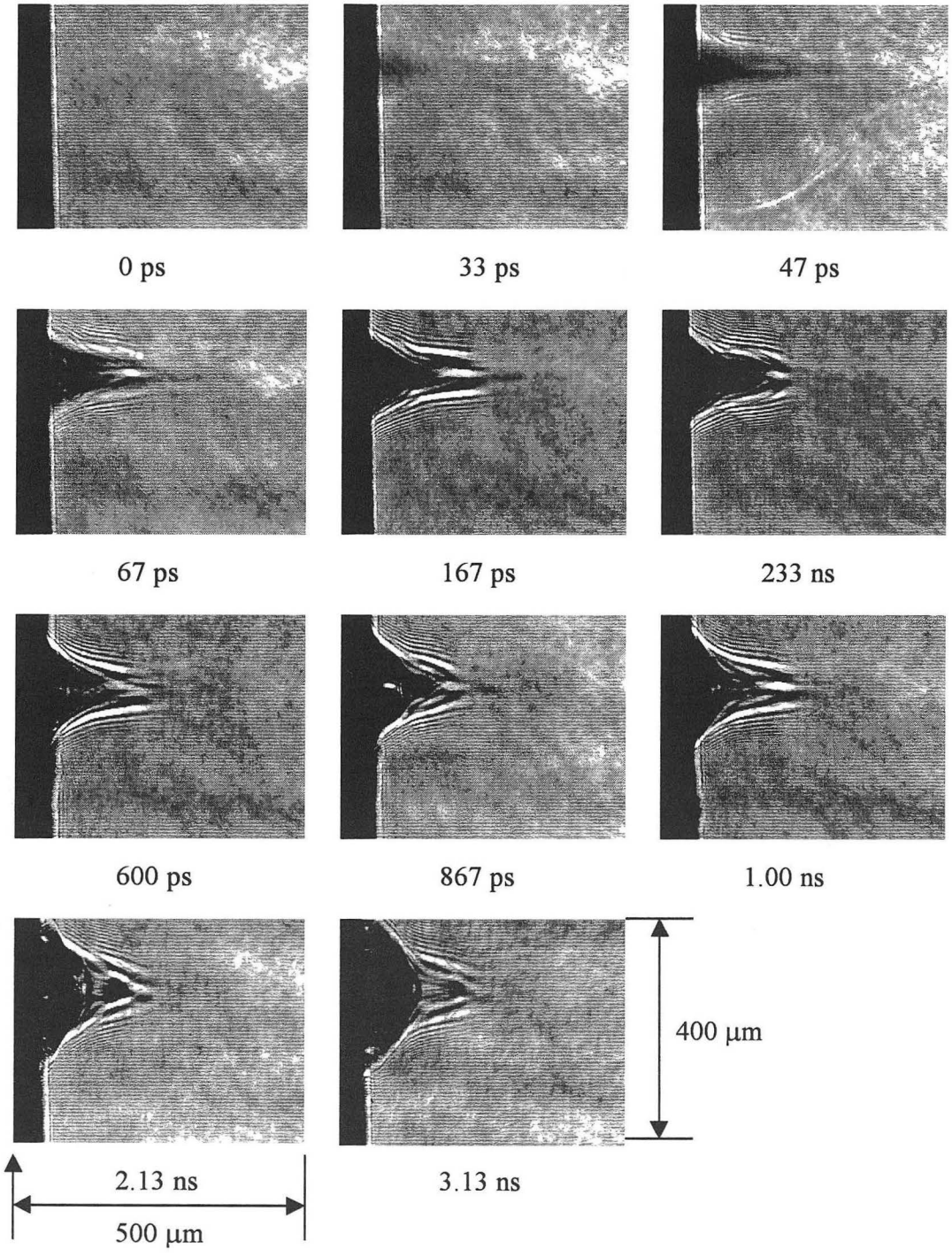

Si surface

Figure 3.10 Time-resolved shadowgraph images of air plasma and vapor plume during picosecond laser ablation (FWHM = 35 ps) of silicon at 9.8×10^{12} W/cm^2

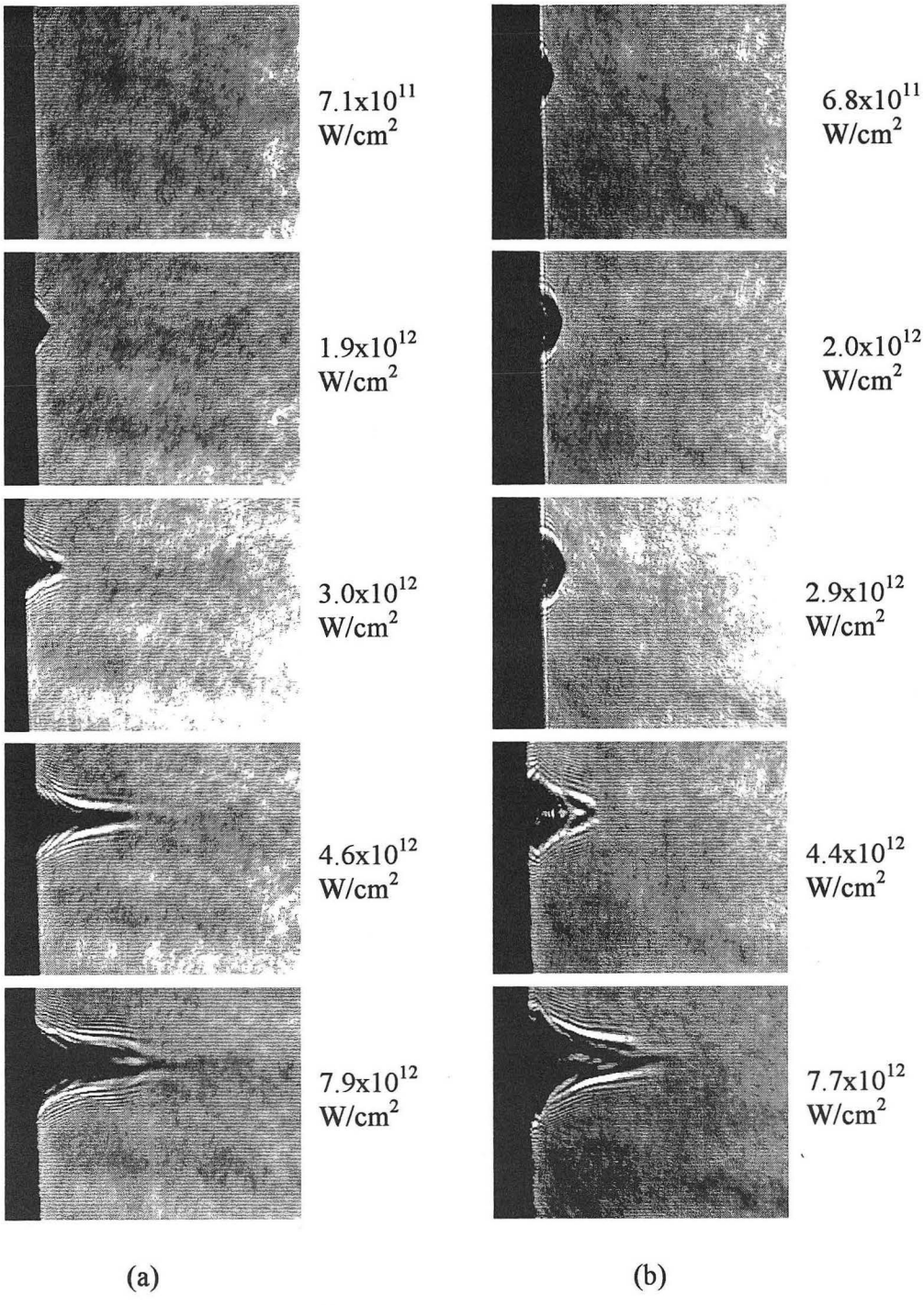

Figure 3.11 Dependence of air plasma and vapor plume formation on laser irradiance at selected times. (a) 68 ps and (b) 1.0 ns (FWHM = 35 ps)

REFERENCE

1. R.E. Russo and X.L. Mao: Chemical Analysis by Laser Ablation, in *Laser Ablation and Desorption*, ed. By J.C. Miller and R.F. Haglund (Academic Press, San Diego 1998) p. 375
2. S.S. Mao, X.L. Mao, J.H. Yoo, R. Greif, and R.E. Russo: J. Appl. Phys. **83**, 4462 (1998)
3. S.I. Ansimov, B.L. Kapeliovich, and T.L. Perelman: Sov. Phys. JETP **39**, 375 (1974)
4. M. Bensoussan and J.M. Moison: J. Phys. C **7**, 149 (1981)
5. J.T. Dickinson: Nucl. Instrum. Methods Phys. Res. B **91**, 634 (1994)
6. S.S. Mao, X.L. Mao, R. Greif, and R.E. Russo: Appl. Phys. Lett. **76**, 31 (2000)
7. T.Q. Qiu, and C.L. Tien: J. Heat Transfer **115**, 835 (1993)
8. D. von der Linde, K. Sokolowski-Tinten, and J. Bialkowski: Applied Surface Science 109/110, 1 (1997)
9. R. Kelly: Nucl. Instrum. Methods Phys. Res. B **46**, 441 (1990)
10. S.H. Jeong, R. Greif, and R.E. Russo: Appl. Surf. Sci. **127-129**, 177 (1998)
11. X. Mao and R. Russo: Appl. Phys. A 64, 1 (1997)
12. M. A. Shannon, X. Mao, A. Fernandez, W.T. Chan, and R. E. Russo: Anal. Chem. 67, 4522 (1995)
13. J.R Ho, C.P. Grigoropoulos, and J.A.C. Humphrey: J. Appl. Phys. **78**, 4696 (1995)

14. J.R. Ho, C.P. Grigoropoulos, and J.A.C. Humphrey: J. Appl. Phys. **79**, 7205 (1996)

15. R. Kelly, A. Miotello, B. Braren, and C.E. Otis: Appl. Phys. Lett. **60**, 2980 (1992)

16. R. Kelly and A. Miotello: Nucl. Instrum. Methods Phys. Res. B **91**, 682 (1994)

17. R. Srinivasan: J. Appl. Phys. **73**, 2743 (1993)

18. R. Srinivasan: J. Appy. Phys. **70**, 7588 (1991)

19. M. Von Allmen: Laser Beam Interactions with Materials (Springer, Heidelberg, 1987)

20. S.S.Mao: PhD dissertation, University of California at Berkeley, May 2000

21. S.S. Mao, X.L. Mao, R. Greif, and R.E. Russo: Phys. Rev. Lett. (submitted for publication)

Chapter 4

Phase Explosion (Explosive Boiling) and Induced Transparency during High Irradiance Laser Ablation

4.1 Introduction

In the two previous chapters, several experimental results showed the onset of a new ablation mechanism under high irradiance. The crater morphology study using white light interferometry reveals a drastic change in crater structures for laser irradiances above a threshold value. Time-resolved shadowgraphy shows that a sudden change in crater morphology is accompanied by violent ejection of large droplets which occurs at microsecond times.

One of the possible mechanisms that can account for increased mass removal under high irradiance is phase explosion, otherwise known as explosive boiling. Phase explosion refers to an abrupt release of mass that occurs near the thermodynamic critical temperature. Martynyuk [1,2,3,4] conducted pioneering experimental and theoretical investigations of explosive boiling. He observed a violent explosion of a rapidly heated metal wire and attributed this phenomenon to the occurrence of homogeneous nucleation within a molten metal layer. Other researchers have reported that the phenomena of phase explosion occurred when they subjected water and other organic liquid droplets to rapid heating with a short laser pulse [5,6,7,8]. Under intense heating, these droplets abruptly and violently explode during the laser heating. More recently, Kelly and Miotello [9,10]

proposed phase explosion as a primary mechanism for mass removal in pulsed laser sputtering.

In order for phase explosion to occur during laser ablation, the sample must be heated rapidly to conditions near the critical state. Very short times do not allow normal heterogeneous boiling and superheated liquid with temperature above the boiling point is formed. In a pool of superheated liquid near the critical state, homogeneous nucleation can occur, leading to phase explosion [9,10]. Thus, when phase explosion is the dominant mechanism for laser ablation, knowledge of the superheated liquid thickness near the critical temperature is critical in determining the crater depth and hence the amount of mass removed from the sample.

In this chapter, we analyze phase explosion during high irradiance ablation of silicon sample by considering two models; thermal evaporation and explosive boiling model. For the explosive boiling model, we also employed the theory of induced-transparency of metals near the thermodynamic critical temperature. Ablation depths were calculated using these two models and were compared with the experimental data. It is shown that computed ablation depths grossly underestimate the measured crater depths for irradiances above the threshold if only thermally evaporated mass is accounted for in estimating the ablation mass. Instead, above the threshold irradiances, the thickness of remaining superheated liquid (obtained by solving the energy equation) near the critical state at experimentally observed time of large particulate ejection agrees well with the crater depth data. From the results of the analysis for irradiances above the

threshold, it is proposed that phase explosion may be the dominant mechanism for mass removal and causes a dramatic change in the crater morphology.

4.2 Background on Phase Explosion (Explosive Boiling)

A possible mechanism for particulate ejection that contributes to formation of deep crater structures is phase explosion. Kelly [9,10,11,12] reported on the importance of this mechanism for mass removal during short pulse laser heating; rapid heating is required to induce explosive boiling. Since thermal diffusion takes place on the order of 10^{-11} second [13], a melt layer can readily form and propagate into the bulk silicon during the laser pulse. The liquid silicon can be heated above its normal boiling temperature and become superheated. The superheated liquid is said to be in a metastable state. Normal boiling occurs by heterogeneous nucleation at the solid-liquid interface or from microscopic gas inclusions. Because microscopic gas inclusions in pure molten silicon are unlikely to exist and the liquid-solid interface is rapidly changing during laser heating and subsequent cooling of molten silicon, there are a lack of sites for heterogeneous nucleation during laser ablation of silicon with a nanosecond pulse [9,10]. Normal boiling is not likely to be a significant process during short pulse laser heating.

The metastable state of liquid silicon is represented by the area between the liquid saturation curve and the liquid spinodal curve on a P-V thermodynamic diagram (Figure 4.1). On a P-T thermodynamic diagram, the same region is identified between the saturation curve and the spinodal line (Figure 4.2). The

spinodal curve in Figure 4.1 is determined from the thermodynamic stability criteria [14,15,16]:

$$\left(\frac{\partial P}{\partial V}\right)_T < 0 \tag{4.1}$$

By using a Van der Waals or Berthelot relation and setting $(\partial P/\partial V)_T = 0$, an expression for the spinodal curve in Figure 4.1 can be obtained. The spinodal curve specifies the maximum temperature to which metastable liquid silicon can be heated. Superheating beyond the liquid spinodal such as described by curve CDE in Figure 4.1 is not possible since these states violate the thermodynamic stability criteria given by equation (4.1). For a short pulse with high power laser irradiation, liquid silicon can be heated to a temperature near the spinodal limit without undergoing normal heterogeneous boiling.

Figure 4.3 illustrates a sequence of processes that may occur in the superheated liquid that is heated near the critical temperature. It is postulated that near the spinodal limit (denoted by the dotted line in Figure 4.2), superheated liquid silicon experiences large density fluctuations [14,15,16]. Near the critical point, these fluctuations can generate vapor bubbles in the superheated liquid silicon. For radii greater than a critical radius, r_c, vapor bubbles will grow spontaneously; bubbles less than r_c are likely to collapse [14]. The expression for r_c is given by:

$$r_c = \frac{2\sigma}{P_{sat}(T_l)\exp\{v_l[P_l - P_{sat}(T_l)]/RT_l\} - P_l} \tag{4.2}$$

where σ is the surface-tension coefficient, P_l is the pressure of the superheated liquid, v_l is the specific volume of the superheated liquid, T_l is the temperature of

the superheated liquid, P_{sat} is the saturation pressure at the superheated liquid temperature, and R is the gas constant. Once vapor bubbles of size r_c are generated in the superheated liquid, they cause the liquid to undergo a rapid transition to phase explosion which produces a mixture of vapor and liquid droplets. The craters resulting from this violent expulsion of liquid are likely to have rough surface structures and also poor repeatibility with respect to the depth and volume of the crater. Above 2.2×10^{10} W/cm^2 (threshold irradiance for nanosecond ablation of silicon at λ = 266 nm), the pulse-to-pulse variation of the crater depth and volume increase significantly and the white light interferometric microscope images show rough crater structures in the deep hole.

4.3 Threshold Irradiance for Phase Explosion

An order-of-magnitude estimate was made for the laser irradiance needed to initiate explosive boiling during nanosecond laser ablation of silicon and was compared to the experimentally observed threshold irradiance corresponding to a change in crater structure. Optically, liquid silicon behaves like a liquid metal [17,18] and the optical penetration depth of the liquid metal ($\delta_p = \kappa^{-1}$ where κ is the absorption coefficient) is much shorter than the thermal penetration depth ($\delta_T = \sqrt{\alpha t_p}$ where α is the thermal diffusion coefficient and t_p is the temporal pulse width of the laser beam). The incident surface laser-beam radiative flux, Q_o,

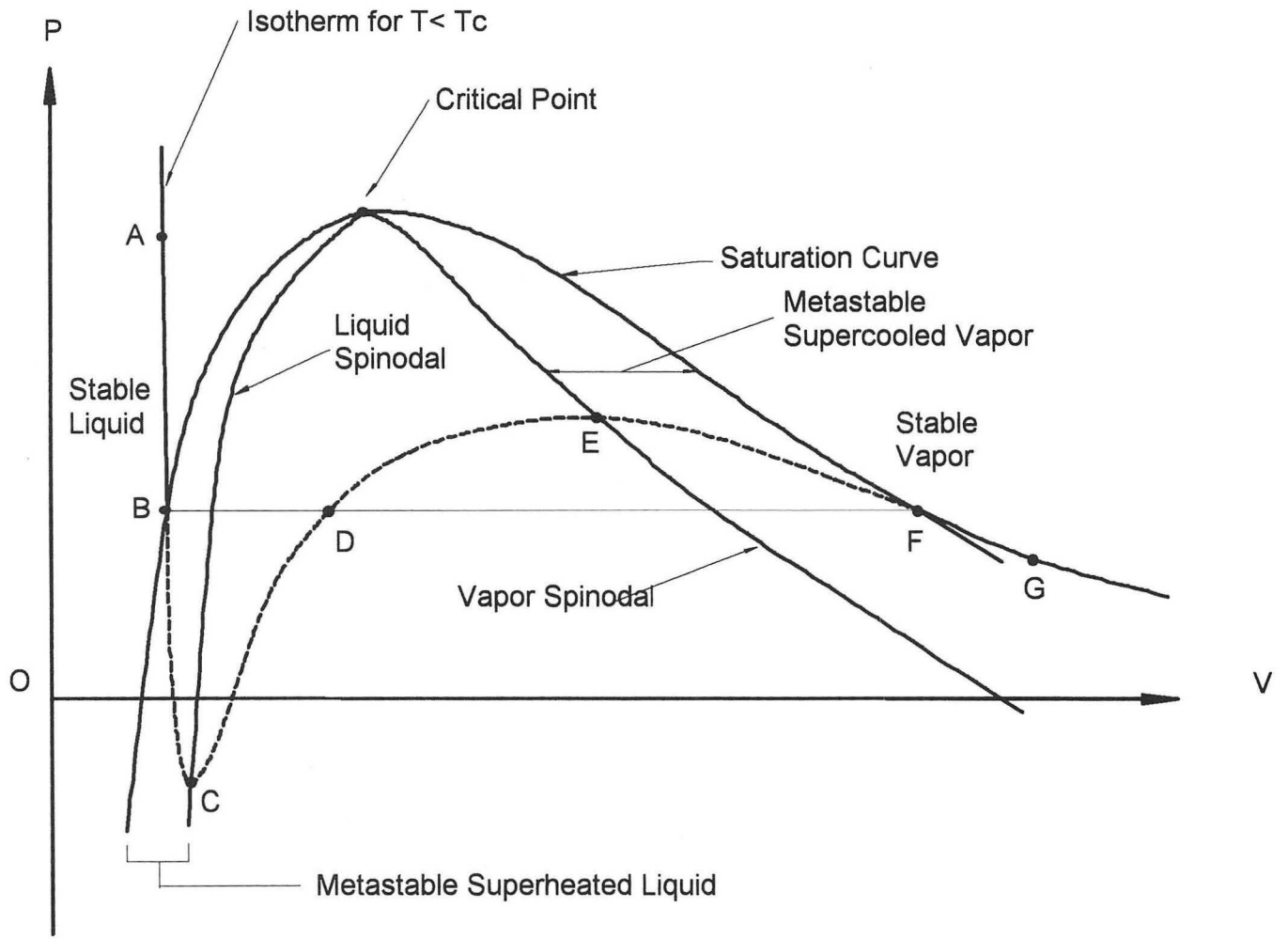

Figure 4.1 Spinodal lines and metastable regions on a P-V diagram

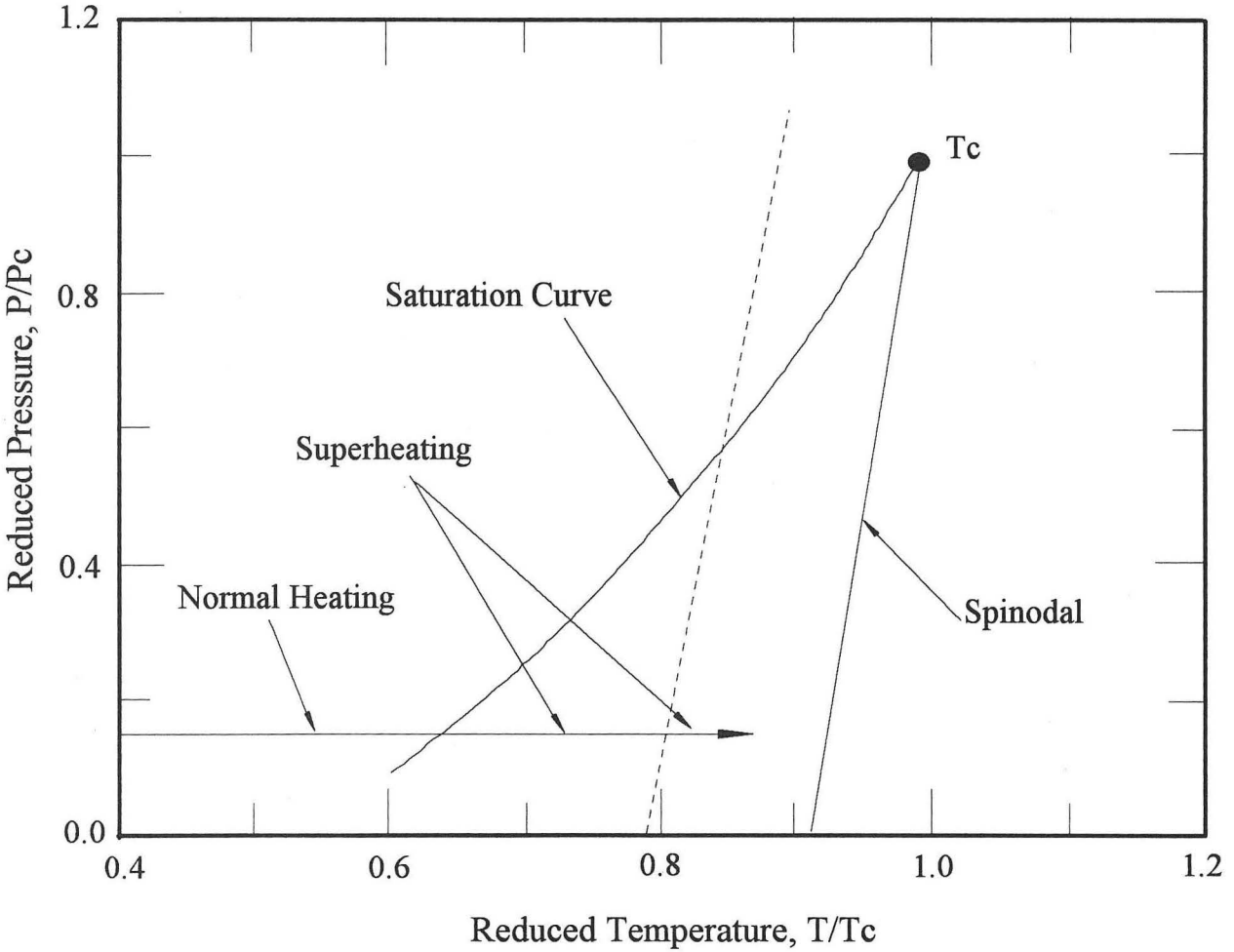

Figure 4.2 Region showing superheating of liquid silicon on a generalized P-T diagram

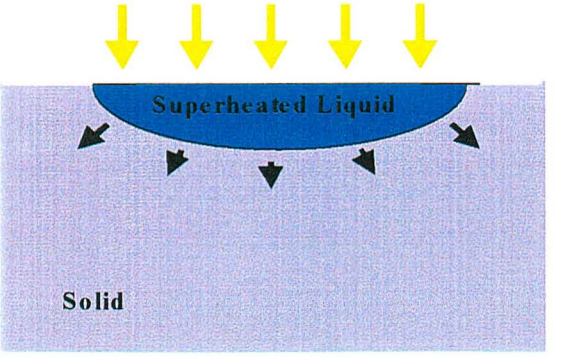

Superheated liquid heated to near critical state due to short heating time and insufficient heterogeneous nucleation sites

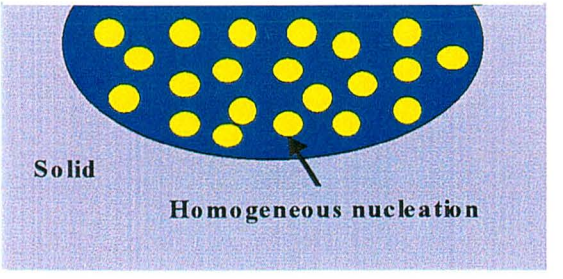

Homogeneous nucleation by density fluctuations at T ~ 0.8 to 0.9 T_c and growth of vapor bubbles to the critical size in the superheated surrounding

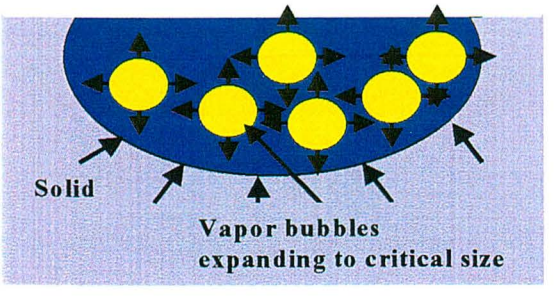

Spontaneous and rapid growth of bubbles after the critical size, resulting in a violent ejection of liquid mass

Figure 4.3 Sequence of possible processes in the superheated liquid during laser heating of the sample

multiplied by (1-R) where R is the reflectivity can be modelled as the heat flux into the silicon surface. The temperature distribution for a 1-D semi-infinite solid with a constant surface heat flux $Q_o(1-R)$ is expressed as [19,20]:

$$T(x,t) = \frac{Q_o(1-R)}{k}\sqrt{\frac{4\alpha t}{\pi}}\left(e^{\frac{-x^2}{4\alpha t}} - x\sqrt{\frac{\pi}{4\alpha t}}erfc(\frac{x}{\sqrt{4\alpha t}})\right) \qquad (4.3)$$

Q_o is determined for the case where the liquid silicon is heated to a temperature near the spinodal limit at $t = t_p$ (3 nsec) and $x = 2\sqrt{\alpha t_P}$. The spinodal temperature would depend on the actual pressure of the superheated liquid, typically ranging from 0.8 to 0.9 T_c. The actual pressure of the superheated liquid under short pulse laser irradiance is difficult to evaluate, and a median value of 0.85 T_c was used for the calculations. Due to the lack of available data, the critical temperature of silicon was assumed to be 5000 K, which is an average value for common metals [3]. The value for R and the thermal properties of silicon were obtained from [17], [18], [21],[22],and [23]. From Equation (4.3), Q_o was estimated to be $3.1\text{x}10^9$ W/cm^2. The onset of particulate ejection observed from the crater depth data and the shadowgraph images, was $\approx 2.2\text{x}10^{10}$ W/cm^2. However, due to "plasma shielding", a portion of the laser power does not reach the sample surface [21,24,25,26]. A theoretical prediction of the degree of plasma shielding that occurs near the laser irradiance of $2.2\text{x}10^{10}$ W/cm^2 is difficult to obtain due to the incomplete knowledge of the ablation phenomena. Mao and Russo [26] investigated plasma shielding by studying the reflected and transmitted laser pulse temporal profiles from metal and glass samples. Their work showed that only

about 20% of the laser beam energy was transmitted through the plasma to the sample surface at the laser output of 2.2×10^{10} W/cm^2 Using a value of 20% for the transmission of the laser power to the sample, the calculated threshold irradiance incident on the sample would be 4.4×10^9 W/cm^2. This value is close to the estimated irradiance to induce explosive boiling [3.1×10^9 W/cm^2 obtained from Eq. (4.3)].

4.4 Delay in Mass Ejection due to Phase Explosion

The characteristic time for explosive boiling induced by a short laser pulse is likely to be related to the time required for vapor nuclei to grow to size r_c. For short pulse laser heating, small vapor bubbles can be generated in the superheated liquid layer due to increased density fluctuations near the spinodal limit. These vapor bubbles can continue to grow after the laser pulse due to heat transfer from the superheated liquid silicon to the bubble interface. Once these bubbles grow to r_c, further growth of the vapor bubbles is spontaneous and explosive boiling should start.

The time for vapor bubbles to grow from initiation (of very small radii) to r_c was estimated and compared with the experimental delay time for particulate ejection. During and just after the laser pulse, bubble growth in the superheated liquid is strongly influenced by the momentum interaction between the growing bubble and the surrounding liquid being pushed away. At this time, heat transfer from the superheated liquid to the bubble interface is rapid and large, and is not a

limiting factor. The bubble growth in this regime is given by the following expression [14]:

$$r(t) = \left\{ \frac{2}{3} \left[\frac{T_l - T_{sat}(P_l)}{T_{sat}(P_l)} \right] \frac{H_{lv}\rho_v}{\rho_l} \right\}^{1/2} t \qquad (4.4)$$

where T_l, P_l, and $T_{sat}(P_l)$ represent the temperature and the pressure of the superheated liquid, and the saturation temperature at the superheated liquid pressure, respectively. H_{lv} is the latent heat of vaporization of the liquid, and ρ_l and ρ_v are the density of the liquid and the vapor. The time for the bubbles to grow to the critical size was obtained by solving for t from expression (4.4) when $r(t) = r_c$.

The critical radius, r_c, for superheated liquid silicon was evaluated using expression (4.2). The critical temperature of silicon was assumed to be 5000K. Large density fluctuations in a superheated liquid are reported at values of temperature of 0.8 ~ 0.85 T_c [9,10]. Accordingly, T_l was assumed to be 0.83 T_c. $P_{sat}(T_l)$ was obtained from the Clausius-Clayperon relation. The recoil pressure of the evaporating vapor, $0.54P_{sat}(T_l)$ [21], was approximated to be the pressure of the superheated liquid silicon layer, P_l. Above assumptions as well as the lack of knowledge on variation of surface tension of the liquid silicon can result in a substantial uncertainty in the calculated values for r_c and the bubble growth time. Therefore, the calculation is only expected to yield rough estimates for the derived quantities. The surface tension of liquid silicon, σ, at the melting temperature is 0.73 N/m [27]. The surface tension coefficient decreases as the temperature increases. Yoshida [28] suggested a relation for σ for liquid metals near the critical

state. Using this relation for silicon, a reduction of nearly 80% occurs for the value of σ at the assumed T_l. This yields a range for σ during laser heating from 0.14 to 0.73 N/m which yields a range in r_c to from 0.8 to 4.0 μm from equation (4.2). With this estimated r_c, Equation (4.4) yields the time for vapor nuclei to grow to r_c to lie between 90 to 490 nsec. The measured time delay for particulate ejection was 300 ~ 400 nsec. Because the probe beam created a dark diffraction fringe near the sample surface, the ejected particulates were noticed at a location slightly above the sample surface in the shadowgraph images. Considering the time for the particulates to reach this location, the observed delay time for particulate ejection is consistent with the time scale estimated from equation (4.4). Agreement between the experimental time and the calculated bubble growth time suggests that the time for the initiation of mass ejection may be associated with the time for vapor bubbles to grow to the critical size in the superheated liquid and for phase explosion to occur.

4.5 Analysis by Solution of the Energy Equation

4.5.1 Thermal Evaporation

The equation for the conservation of energy is given by

$$\rho C \frac{\partial T}{\partial t} - \rho C v \frac{\partial T}{\partial x} = \frac{\partial}{\partial x}\left(k \frac{\partial T}{\partial x} \right) + S \tag{4.5}$$

where T is temperature, t is time, ρ is density of the sample, C is specific heat, v is the receding velocity of the sample surface during evaporation, and k is thermal

conductivity. The spatial coordinate x is in the direction normal to the sample surface with the origin located at the surface. The source term, S, represents the laser energy absorbed by the sample and is expressed as

$$S = I_0(t)\alpha \exp(-\alpha x) \tag{4.6}$$

where I_0 [W/cm^2] is the temporal laser irradiance at the sample surface and α is the absorption coefficient of the sample material at the incident laser wavelength. The velocity v in Equation (4.5) is given by

$$v = \frac{\eta \dot{m}_v}{\rho_l} \tag{4.7}$$

where $\dot{m}_v$ is the mass flux of vapor evaporated from the liquid surface, ρ_l is the density of the liquid, and η is the ratio of molecules escaping the sample surface (without recondensation) to the total evaporated molecules. $\dot{m}_v$ is calculated using the Hertz-Knudsen formula [29],

$$\dot{m}_v(T_0) = p_0(T_0)\left(\frac{m_a}{2\pi k_B T_0}\right)^{\frac{1}{2}} \tag{4.8}$$

where m_a is the atomic mass of silicon. Subscript 0 represents the evaporation surface. The saturation pressure of the vapor at the evaporation surface, $p_0(T_0)$, is obtained from the Clausius-Clapeyron equation,

$$p_0(T_0) = p_\infty \exp\left[\frac{L_{ev}}{R_v T_{ev,\infty}}\left(1 - \frac{T_{ev,\infty}}{T_0}\right)\right] \tag{4.9}$$

where R_v is the gas constant of the vapor and L_{ev} and T_{ev} represent the latent heat of evaporation and the boiling temperature of the liquid, respectively. Subscript ∞

represents atmospheric pressure. The coefficient η in Equation (4.7) was assumed to be unity (no recondensation), but rigorous analysis indicated that recondensation of evaporated molecules could be as large as about 20 %[30].

For analyses with a phase change that includes a liquid-solid interface, an enthalpy formulation is commonly employed [31 - 34]. In the enthalpy formulation, which is used in the present work, the position of the liquid-solid interface does not appear explicitly. Instead, the variation of the enthalpy, h, is used to locate the phase boundary. Using the enthalpy formulation, Equation (4.5) can be rewritten as

$$\frac{\partial h}{\partial t} - v\frac{\partial h}{\partial x} = \frac{\partial}{\partial x}\left(k\frac{\partial T}{\partial x}\right) + S \tag{4.10}$$

where $h(T)$, is defined as

$$h(T) = \int_0^T \rho_s C_s \, dT \qquad \text{for } T < T_{sm} \tag{4.11}$$

$$h(T) = \int_0^{T_{sm}} \rho_s C_s \, dT + \int_{T_{sm}}^{T} \rho_m (C_m + dL_m/dT)\, dT \qquad \text{for } T_{sm} \le T < T_{lm} \tag{4.12}$$

$$h(T) = \int_0^{T_{sm}} \rho_s C_s \, dT + \int_{T_{sm}}^{T_{lm}} \rho_m (C_m + dL_m/dT)\, dT + \int_{T_{lm}}^{T} \rho_l C_l \, dT \quad \text{for } T_{lm} \le T \tag{4.13}$$

In Equations (4.11)-(4.13), it is assumed that the phase transformation of solid to liquid occurs over a small temperature range between T_{sm} and T_{lm}, defined as a *mushy region* (Figure 4.4). Employing a temperature range for phase change instead of a fixed melting temperature with a step change in h makes it easier to obtain numerical solutions [34]. For chemically impure substances, this behavior during phase change is more appropriate than a transition at a single temperature

[35]. Subscripts s, m, and l in Eqs. (4.11)-(4.13) represent solid phase, mushy region, and liquid phase, respectively.

To solve Eq. (4.5) or (4.10), boundary conditions are required at x=0 and x=L, where L is the length of the computational domain. At x=L, the temperature of the material is assumed to be unaffected by the laser irradiation, i.e. $T(L, t>0)=T_i$, where T_i is the initial temperature of the solid. At x=0, energy loss to the surrounding air can be ignored because the heat flux is negligible compared to the latent heat of the evaporating vapor. The heat flux due to thermal radiation is at least an order of magnitude smaller than the latent energy carried away by the evaporating mass. Thus, at x=0, an adiabatic boundary condition, i.e. $\partial T/\partial x=0$, was used when there is no surface evaporation. When vaporization exists at the surface, the energy loss was calculated as the latent heat of the evaporating mass.

4.5.2 Induced Transparency of Liquid Silicon Near the Critical Temperature and Phase Explosion

When a metallic sample is heated by intense laser irradiation to temperatures close to the thermodynamic-critical state, the liquid metal, by transforming into a liquid dielectric, becomes almost transparent to the incident laser radiation [36,37,38]. This phenomenon is called induced-transparency or bleaching of liquid metals, and is known to occur at a temperature of about $0.9T_c$. Induced-transparency occurs due to a strong reduction of electron density in the

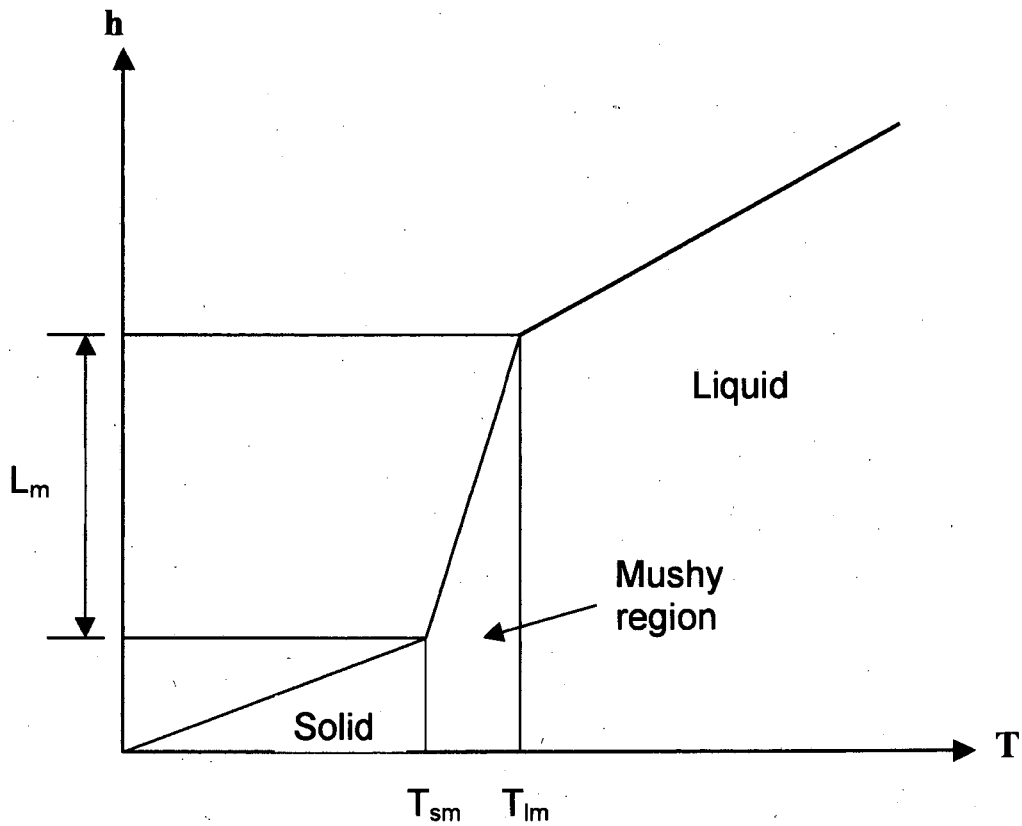

Figure 4.4 Schematic diagram for enthalpy-temperature relation during melting

liquid metal at temperatures near the critical point. Although the mass density of the liquid metal does not change significantly, a small variation results in a strong reduction in electron density [36,37]. When the temperature reaches $0.9T_c$, the liquid becomes transparent and the incident laser energy penetrates through this transparent layer to the underlying material. Because the liquid below the transparent layer may also reach $0.9T_c$ by subsequent heating, the transparent front propagates into the interior liquid until laser heating ceases.

The optical properties of liquid silicon are reported to be similar to those of liquid metals [17,18]. It is therefore proposed that when liquid silicon is heated close to its critical temperature, it may become transparent to the incident laser radiation. Below, we have applied induced-transparency theory to liquid silicon under laser irradiation and investigated the possibility of explosive boiling within the superheated volume.

The details of the induced-transparency theory described below are largely attributed to Batanov et al. [36]. During induced-transparency, three interfaces exist in the sample; the evaporation front at the top of the liquid layer, the liquid-solid interface, and the transparency front between these two interfaces (Figure 4.5). As the liquid metal is heated close to the critical temperature, the reflectivity and absorption coefficient of the heated liquid change drastically. The reflectivity of a metallic surface can be expressed as [39]:

$$R = \frac{(n-1)^2 + \kappa}{(n+1)^2 + \kappa} \tag{4.14}$$

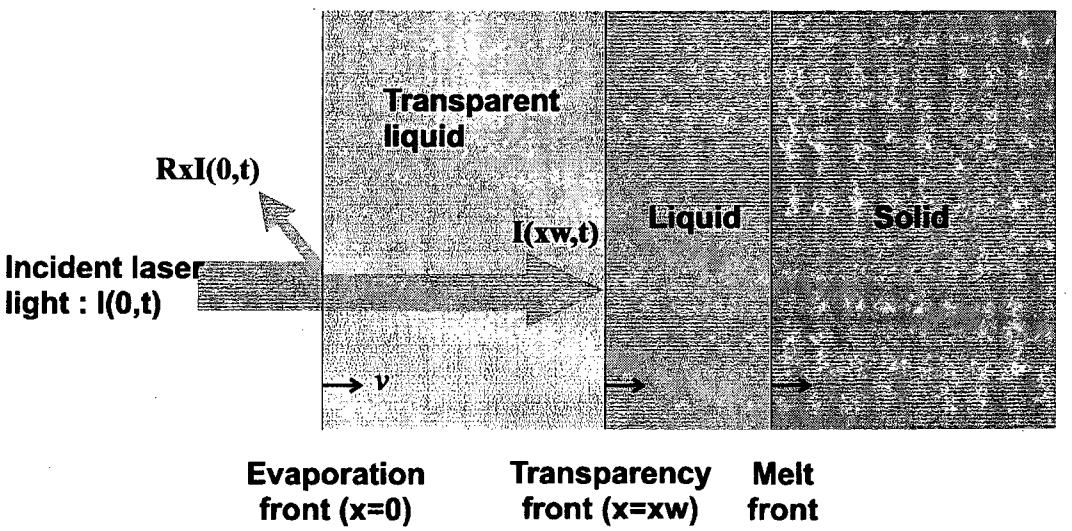

Figure 4.5 Schematic diagram of the sample during induced-transparency in the superheated liquid

where n and κ are real and imaginary parts of the complex refractive index $\hat{n} = n + i\kappa$. n and κ in Eq. (4.14) are described in terms of material properties as

$$n^2 = \frac{1}{2}\left\{\sqrt{\mu^2\varepsilon^2 + \frac{4\mu^2\sigma^2}{f^2}} + \mu\varepsilon\right\} = \frac{\mu\varepsilon}{2}\left\{\sqrt{1+\xi^2} + 1\right. \tag{4.15}$$

$$\kappa^2 = \frac{1}{2}\left\{\sqrt{\mu^2\varepsilon^2 + \frac{4\mu^2\sigma^2}{f^2}} - \mu\varepsilon\right\} = \frac{\mu\varepsilon}{2}\left\{\sqrt{1+\xi^2} - 1\right. \tag{4.16}$$

where μ is magnetic permeability, ε is dielectric constant, σ is electric conductivity, f is frequency of the laser radiation, and $\xi \equiv 2\sigma/\varepsilon f$. Batanov et al. [36] reported that for temperatures close to the critical temperature, the parameter ξ becomes very small ($\xi \ll 1$). As a result, the dielectric constant (imaginary part) is reduced significantly, which then causes absorption in the liquid metal and the reflectivity of the liquid metal surface to decrease drastically. In this work, we assume the superheated liquid silicon becomes optically transparent at 0.9 T_c and its reflectivity at the evaporation front is about 0.2 [36].

From Equation (4.8), the calculated rate of evaporation at x=0 during the induced-transparency period remains constant at $\dot{m}_v(0.9T_c)$. The energy required to maintain this evaporation rate is provided from the incident laser radiation. The energy incident on the transparency front, $I(x_w,t)$, is then equal to the difference between the incident laser energy and the sum of reflected laser energy and the latent heat of evaporation at the surface, i.e.

$$I(x_w, t) = (1-R)I(0,t) - L_{ev}v(0.9T_c) \tag{4.17}$$

When t exceeds τ_p, where τ_p is the laser pulse duration, the thickness of the induced-transparency layer immediately decreases. The temperature at the evaporating front drops below $0.9T_c$ and the receding velocity of the evaporating front becomes smaller than the value during the pulse. In the present analysis, surface evaporation continues until the temperature decreases below the normal boiling temperature. For $t \geq \tau_p$, the energy for evaporation is supplied from the interior liquid and the temperature profile in the liquid has a maximum below the evaporating surface.

4.6 Calculated Results and Discussion

For the calculation, a laser pulse with a Gaussian energy distribution was chosen as the ablation source. Total pulse duration and pulse width at 1/e of the maximum intensity were taken to be 6 ns and 3 ns, respectively, with the maximum located at 3 ns. Laser fluences from 10 to 100 J/cm^2 were used in the calculations. The spatial domain of 50 or 100 μm (depending upon the laser fluence) was uniformly divided with a grid size of 12.5 nm; results obtained for smaller grid sizes differed by a negligible amount. Time steps of 0.1 and 1 picosecond were used for the thermal evaporation and the induced-transparency models, respectively. The thermal and optical properties of silicon used in the computation are given in Table 4.1 [17,18,22]. The initial temperature of the sample was 300 K. The mushy region is assumed to be initiated at the melting temperature, i.e. $T_{sm}=T_m$, and to become liquid at $T_{lm}=T_m+0.1$ K (cf. Figure 4.4). Solutions at each

time step were completed when the computed enthalpy values satisfied the following criterion,

$$\left|\frac{h^{i+1}-h^{i}}{h^{i}}\right|_{grid=j}^{step=n} < 10^{-6}$$

where i is the number of iterations at each time step.

For high power laser ablation of solids, the vapor plume may absorb part of the incident laser energy; energy delivered to the sample surface is smaller than the original pulse energy due to absorption in the plume. This effect is often referred to as "plasma shielding". The ratio of the laser energy transmitted to the sample surface to the laser pulse output energy varies with laser irradiance [40]. To the authors' knowledge, no experimental data are available in the literature for plasma shielding during pulsed laser ablation of silicon for irradiances above 10 GW/cm^2. To estimate the plasma shielding effects for the silicon ablation data, we utilized the energy transmission data for glass samples reported by Mao and Russo [26]. According to Mao and Russo [26], the transmitted energy decreased to only about 20 % of the output pulse energy as the laser power density increased to about 60 GW/cm^2. Using this value to estimate plasma shielding, the net laser fluence at the sample surface ranged from about 3 to 80 J/cm^2 for the crater depth data obtained from nanosecond laser ablation of silicon. The measured crater-depth data are repeated in Figure 4.6 with the laser fluences now reduced by plasma shielding factor. Figure 4.6 also shows the computed depths of the induced-transparency

Table 4.1 Thermal and optical properties of silicon **[17,18,22]**

Latent heat of fusion, L_m (J/g)	1797.0	
Latent heat of vaporization, L_{ev} (J/g)	13722.0	
Melting temperature, T_m (K)	1683.0	
Boiling temperature, T_{ev} (K)	3514.0	
Atomic mass, m_a (g/molecule)	4.666×10^{-23}	
Thermal conductivity, k (J/cm s K)	Solid	$1521.0T^{1.226}$ for $T\leq1200$ K $8.98T^{-0.502}$ for $1200<T<T_m$
	Liquid	$0.5+2.9\times10^{-4}(T-T_m)$
Specific heat, C (J/g K)	Solid	$0.694\exp(2.375\times10^{-4}T)$
	Liquid	1.05
Density, ρ (g/cm^3)	Solid	2.32
	Liquid	2.52
Reflectivity, R	Solid	$(35.5+3.6\times10^{-3}T)/100$
	Liquid	0.72
Absorption coefficient, α (cm^{-1})	Solid	10^5
	Liquid	1.13×10^6
Boltzmann constant, k_B (J/K molecule)	1.38×10^{-23}	

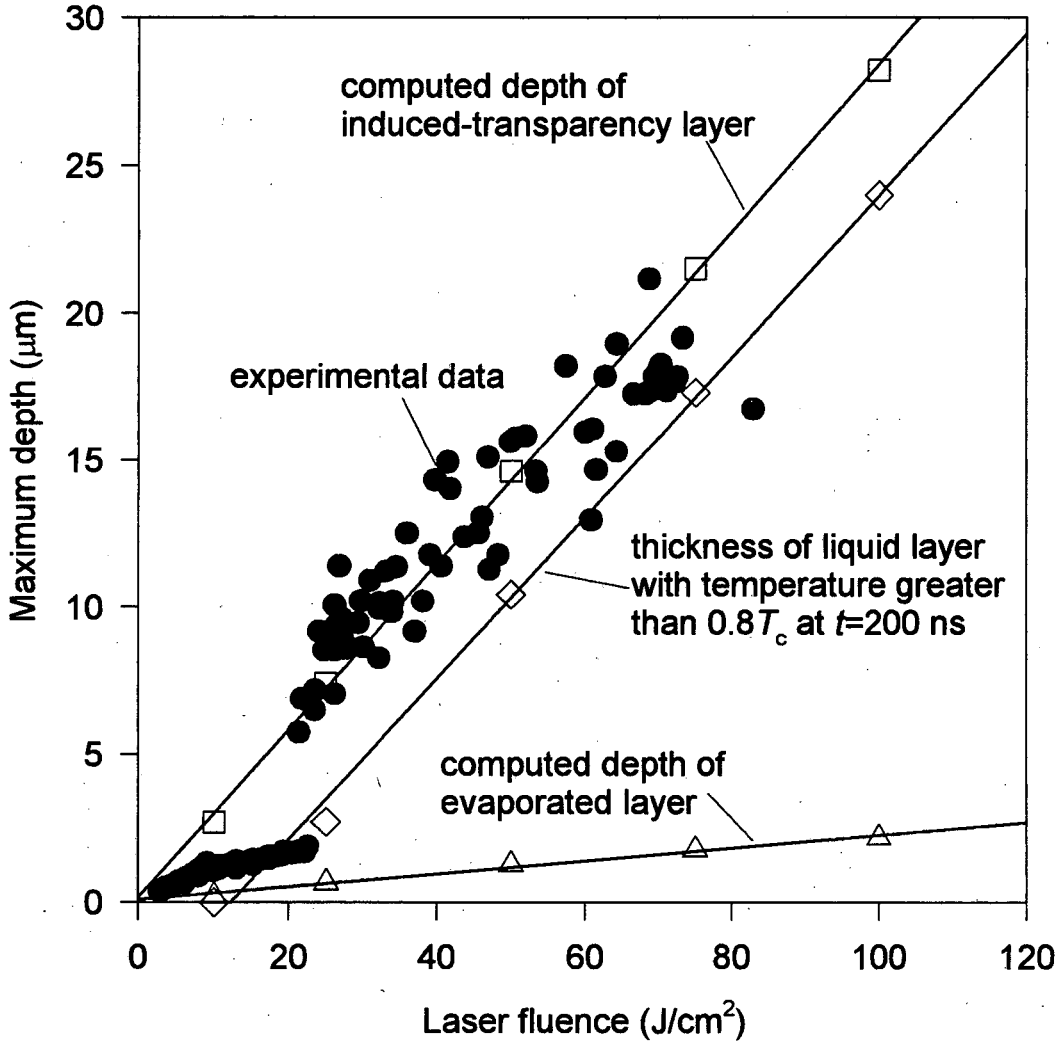

Figure 4.6 Comparison of measured crater depths (●) with the computed data. (□ : maximum depth of induced-transparency layer, ◊ : thickness of liquid layer with temperature greater than $0.8T_c$ at t=200ns, Δ : evaporation depth)

layer and the thermally evaporated layer, using the models described in Section 4.5. The details of these computed results are described below.

4.6.1. Thermal equilibrium model

The receding velocity of the evaporation front, calculated using Equation (4.7) is shown in Figure 4.7. Surface evaporation lasts for about the duration of the laser pulse, 6 ns. By integrating this receding velocity with time, the total thickness of the liquid layer removed due to thermal evaporation, denoted as "evaporation depth", was calculated. Despite the large receding velocity with maximum values ranging from about 100 to 700 m/sec, the computed evaporation depth varied only from about 0.2 to 2.2 μm (cf. Figure 4.6). The depth evaporation computed is shown in Figure 4.6 and is approximately one half of the measured crater depth for laser fluences up to about 25 J/cm^2, at which point the rapid increase in the measured crater depths occurred. For laser fluences above 25 J/cm^2, the computed evaporation depth is approximately an order of magnitude less than the measured crater depth.

The small evaporation depth calculated using the thermal evaporation model may be understood more clearly in conjunction with the computed temperature distributions in the sample. Figure 4.8 shows the calculated temporal variations of the surface temperature for laser fluences from 10 to 100 J/cm^2. The surface temperature change closely follows the temporal variation of the laser pulse; it increases rapidly but decreases almost immediately once the laser pulse

passes the maximum temporal intensity point (cf. Figure 4.7). Because of this fast decrease of the surface temperature, surface evaporation lasts only a short period of time (on the order of the laser pulse duration), resulting in the small calculated evaporation depths.

The critical temperature of most metals is about 10000 K or less [3]; the highest value reported is 15550 K for tungsten [3]. Compared to these reported thermodynamic critical temperatures of metals, the computed surface temperatures of 12000 to 35000 K in Figure 4.8 are well above the measured thermodynamic critical temperature of common metals such as aluminum, copper, etc.. These temperatures are very likely to be well above the critical temperature of silicon as well. When a liquid is heated close to the thermodynamic critical temperature, the liquid undergoes a phase change and becomes a vapor (implying that the computed surface temperatures cannot be considered accurate). Even with the unreasonably high surface temperatures, the evaporation depth calculated using a thermal evaporation model was still an order of magnitude smaller than the measured crater depths for laser fluences greater than 25 J/cm^2. These results demonstrate that the thermal evaporation model does not correctly represent the ablation process for this laser energy regime.

4.6.2 Induced-transparency model

Induced-transparency described in Section II is assumed to occur in molten silicon when the temperature reaches $0.9T_c$. Induced-transparency is initiated at the

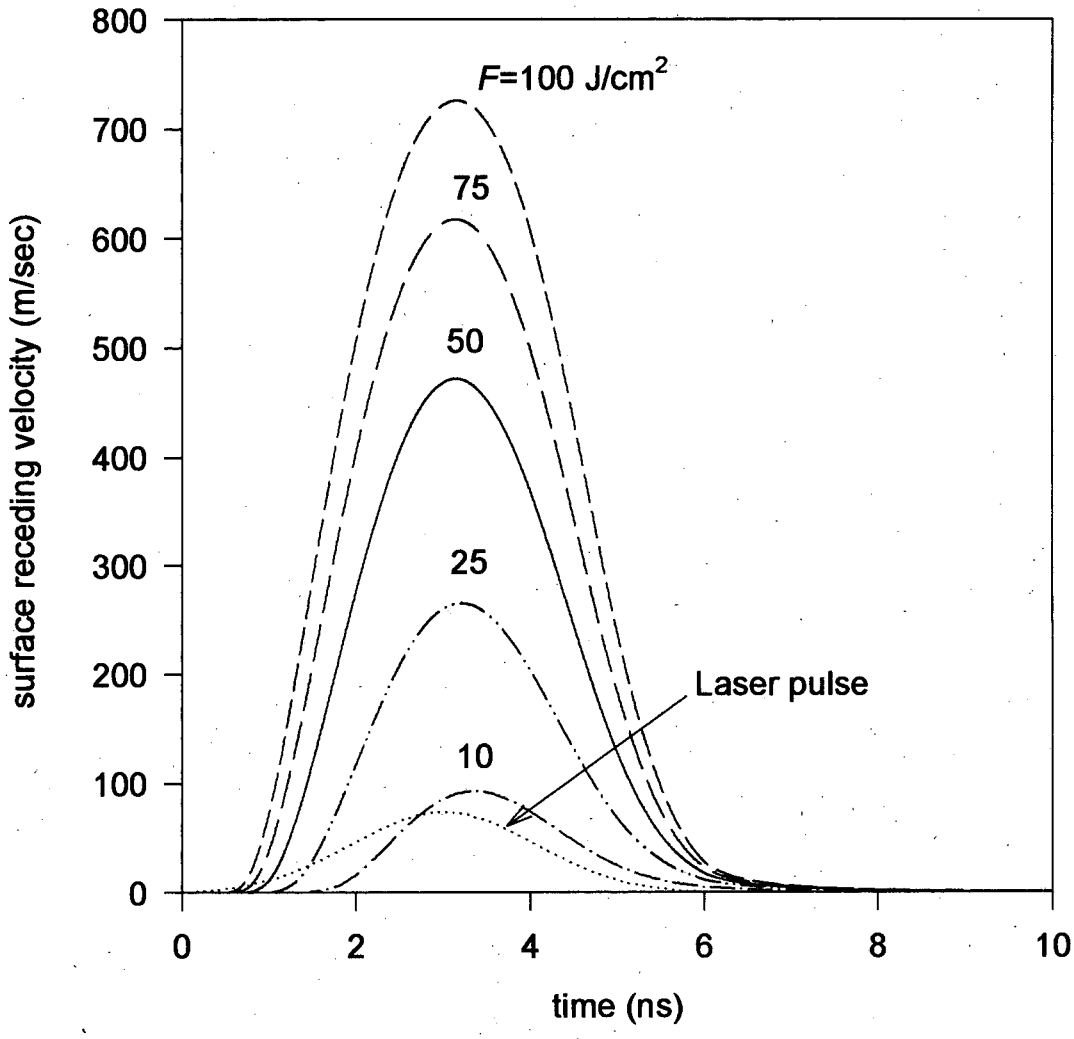

Figure 4.7 Receding velocity of the evaporation front with respect to laser pulse energy. (Thermal evaporation model)

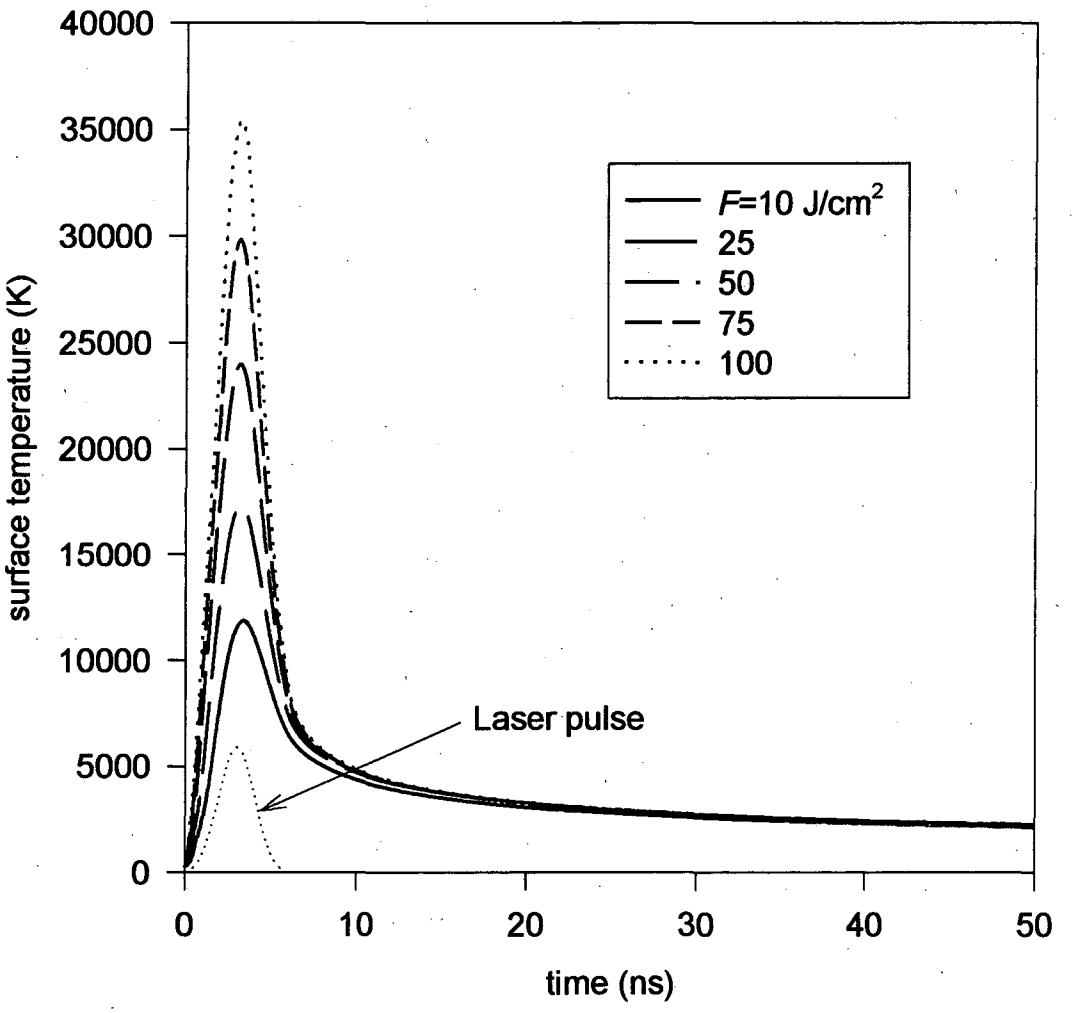

Figure 4.8 Variation of surface temperature for different laser fluences (Thermal evaporation model)

surface and propagates in the liquid. Numerically, the propagation of the transparency front was simulated as follows. When the liquid temperature at a grid point reaches $0.9T_c$, the liquid at this point is assumed to immediately become transparent to the incident laser radiation and this point stays at $0.9T_c$. The liquid next to this grid point absorbs the incident laser energy until its temperature reaches $0.9T_c$, resulting in the propagation of the transparency front.

To the author's knowledge, there are no published measured thermodynamic critical temperature data for silicon. Therefore, the effect of critical temperature on the thickness of computed transparent layer was examined for three specified values of T_c, namely 5000, 7000, and 9000 K, for a laser fluence of 100 J/cm^2. The thickness of the transparent layer decreased by about 40 % when the critical temperature was increased from 5000 to 9000 K, cf. Figure 4.9. The results in Figure 4.9 demonstrate that the order of magnitude of the transparent layer thickness is not significantly affected by the selected critical temperature. Measured thermodynamic critical temperatures of common metals like aluminum, copper, zinc, silver etc. range approximately from 3000 to 6000 K [3]. In this work, we assumed that the critical temperature of silicon also lies in this range and have selected 5000 K.

The computed maximum thickness of the induced-transparency layer for different laser energies was shown in Figure 4.6. The computed thickness of the transparency layer is consistent with the measured crater depths for laser fluences above the threshold value of about 25 J/cm^2. Furthermore, the agreement in the

slopes of the measured crater depth and the computed transparency-layer thickness demonstrates that induced-transparency of the liquid silicon during laser ablation is a possible transport process in this energy regime. Because of the significant uncertainties in the present calculations, e.g. the thermodynamic critical temperature and the optical properties of silicon at high temperatures, the values of the computed transparency layer thickness can be shifted to either higher or lower values.

The computed thickness of the induced-transparency layer itself does not represent the measured crater depth. Instead, the transparency layer provides the conditions that may lead to the generation of deep craters, that is, phase explosion. For phase explosion to take place, the vapor bubbles produced within the superheated metastable liquid must grow above a critical radius. In Section 4.4, the growth time of vapor nuclei in the liquid near the critical state was calculated to be in the range from 100 ~ 500 nanoseconds. As shown in Chapter 3, violent material ejection from the sample was observed after about 300-400 ns from the beginning of laser irradiation, which includes the bubble growth time and the time required for the material to flow out of the sample. The calculated growth-time range is in good agreement with the experimental data. These results demonstrate that for phase explosion to take place, the molten silicon should be in the superheated state for at least 100-300 ns, to allow bubbles to grow to the critical size. The temperature distribution inside the sample at different times shows that after 600 ns from the beginning of laser irradiation, the thickness of the liquid layer that is at

temperatures above $0.8T_c$ for F=100 J/cm^2 is more than 20 μm (Figure 4.10). Therefore, according to the above results, the liquid within 20 μm of the surface has sufficient time to allow vapor bubbles to grow to the critical size. After the laser pulse is completed, the maximum temperature occurs inside the liquid are not at the surface due to the evaporation energy loss at the surface.

The thickness of the liquid layer that is at temperatures greater than $0.8T_c$ (at a certain time) varies with laser pulse energy. Figure 4.11 shows calculated temperature distributions inside the sample at t=200 ns, which is between the lower range of predicted growth time and the measured onset (~ 300 ns) for violent material ejection. For F=10 J/cm^2, the thickness of the induced-transparency layer is about 2.7 μm (cf. Figure 4.6). However, after 200 ns, this transparency layer disappears completely, implying that the vapor bubbles would not have enough time to grow to the critical size and that no phase explosion would occur. For F=25 J/cm^2, the thickness of the induced-transparency layer is about 12 μm. For this laser fluence, at t=200 ns, the thickness of the liquid layer at temperatures greater than $0.8T_c$ is about 3.0 μm and a phase explosion can occur in this region. The thickness of the liquid layer at t=200 ns that has temperatures above $0.8T_c$ increases linearly with the same slope as the induced-transparency layer thickness and the measured crater depths (cf. Figure 4.6). These results demonstrate that for laser ablation with fluences of 25 J/cm^2 or greater, a model for an induced-transparency layer yields a sufficiently hot layer to permit phase explosion of the superheated liquid.

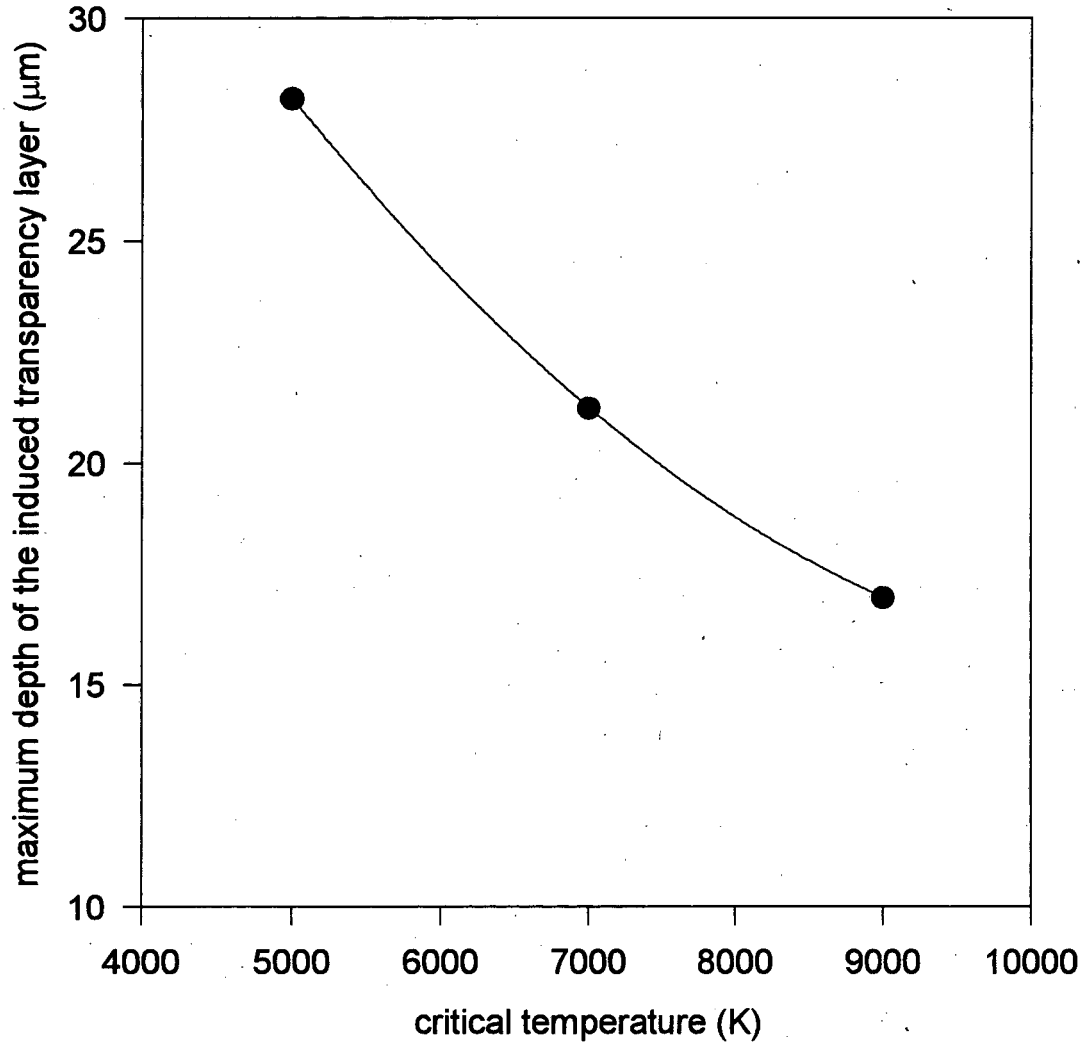

Figure 4.9 Variation of maximum depth of computed induced-transparency layer with respect to thermodynamic critical temperature

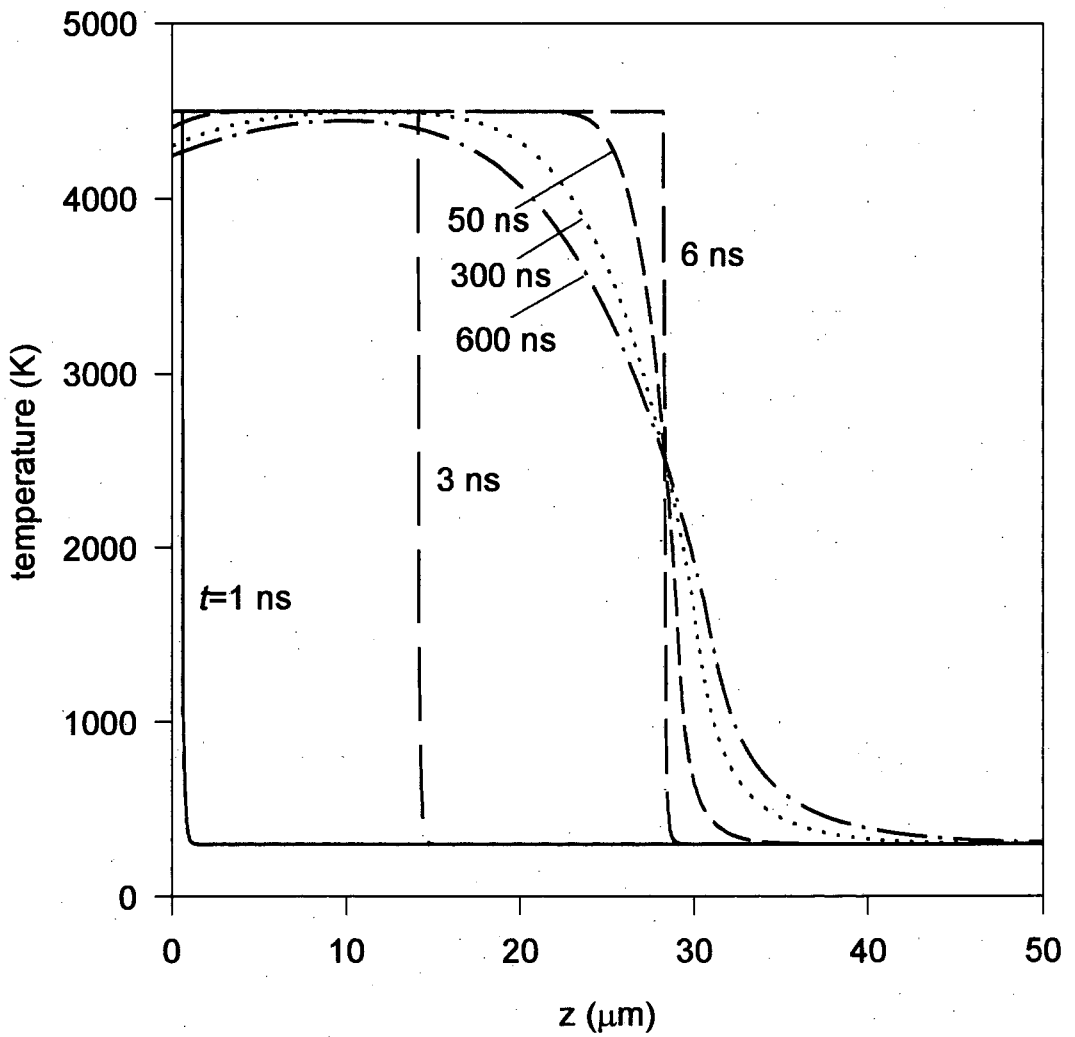

Figure 4.10 Temperature distribution inside the sample at different elapsed times (Induced-transparency model, F=100 J/cm^2)

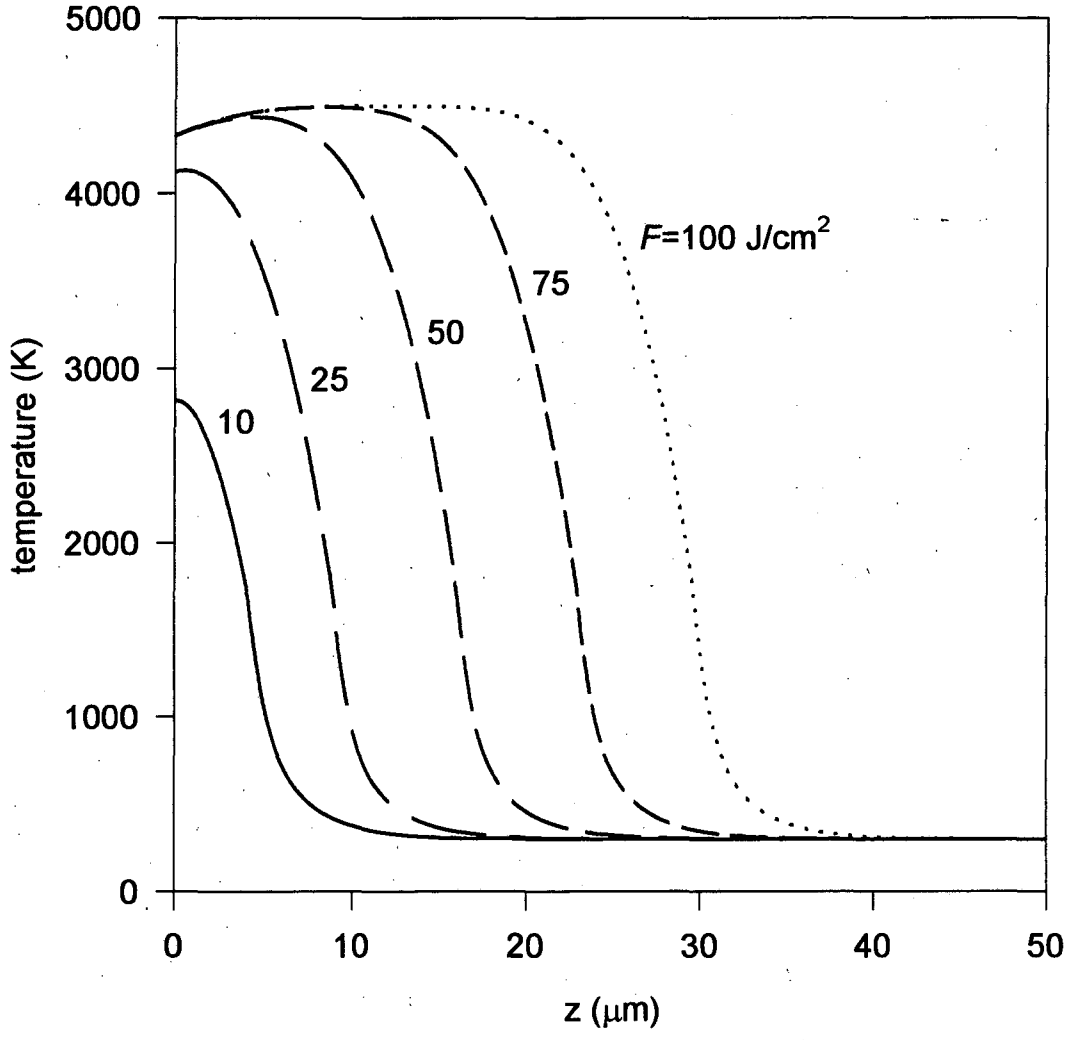

Figure 4.11 Temperature distribution inside the sample for different laser fluence at 200 ns after laser pulse irradiation is initiated (Induced-transparency model)

4.7 Conclusions

In previous chapters, we reported a dramatic increase in crater depth at a threshold laser fluence of 66 J/cm^2 (2.2x10^{10} W/cm^2) during nanosecond laser ablation of silicon. Above this threshold fluence, crater depths as large as 20 μm were produced from a single laser pulse of ns duration, and they were deeper by approximately an order of magnitude than the depths at fluences below the threshold value. The present work demonstrated that thermal evaporation cannot account for the crater depth data. Thermal evaporation grossly underestimates the measured depth, especially for the fluence regime above the threshold value. For fluences above the threshold value, good agreement between the measured and calculated crater depth can be obtained with the following assumptions:

1) Crater depth is assumed to be equal to the thickness of a liquid layer heated to a condition close to the critical state at a time of 200 ~ 300 ns. After the initiation of laser heating, particulate ejection was found to begin in this time range.
2) The superheated liquid silicon makes a transition from a metal to a dielectric and becomes transparent to incoming laser irradiation.

The above results suggest that induced transparency and explosive boiling may be important processes in forming deep craters. Induced transparency promotes formation and growth of the superheated liquid layer; the transparent liquid layer allows more incident irradiation to penetrate into the liquid to a liquid-solid interface during laser heating. Consequently, the resulting superheated liquid

layer is thicker and a greater amount of superheated liquid heated close to the critical temperature is present after the laser pulse. Vapor formed by density fluctuations near the critical state can nucleate as bubbles in this superheated liquid layer; once these vapor bubbles obtain a critical size, they can expand rapidly and initiate explosive boiling and mass ejection in the form of particulates.

REFERENCE

1. M.M. Martynyuk: Sov. Phys. Tech. Phys. **21**, 430 (1976)
2. M.M. Martynyuk: Sov. Phys. Tech. Phys. **19**, 793 (1974)
3. M.M. Martynyuk: Russ. J. Phys. Chem. **57**, 494 (1983)
4. M.M. Martynyuk: Russ. J. Phys. Chem. **49**, 1545 (1975)
5. P. Kafalas and A.P. Ferdinand, Jr.: Appl. Opt. **12**, 29 (1973)
6. P.Kafalas and J. Herrmann: Appl. Opt. **12**, 772 (1973)
7. J.D. Pendleton: Appl. Opt. **24**, 1631 (1985)
8. B.S. Park, A. Biswas, R.L. Armstrong, and R.G. Pinnick: Opt. Lett. **15**, 206 (1990)
9. A. Miotello and R. Kelly: Appl. Phys. Lett. **67**, 3535 (1995)
10. R. Kelly and A. Miotello: Applied Surface Science **96 – 98**, 205 (1996)
11. A. Peterlongo, A. Miotello, and R. Kelly: Phys. Rev. E **50,** 4716 (1994)
12. A. Miotello and R. Kelly: Appl. Phys. A **69** [Suppl.], S67 (1999)
13. D. von der Linde, K. Sokolowski-Tinten, and J. Bialkowski: Appl. Surf. Sci. **109/110**, 1 (1997)
14. V.P. Carey: Liquid-Vapor Phase-Change Phenomena (Hemisphere, Washington, 1992)
15. P.G. Debenedetti: Metastable Liquids (Princeton, New Jersey, 1996)
16. V.P. Skripov: Metastable Liquids (John Wiley & Sons, New York, 1974)
17. R.O. Bell, M. Toulemonde, and P. Siffert: Appl. Phys. A **19**, 313 (1979)

18. I. Lukes, R. Sasik, and R. Cerny: Appl. Phys. A **54,** 327 (1992)

19. J.F. Ready: Effects of High-Power Laser Radiation (Academic Press, New York, 1971)

20. N. Ozisik: Heat Conduction (John Wiley & Sons, New York, 1993)

21. M. Von Allmen: Laser Beam Interactions with Materials (Springer, Heidelberg, 1987)

22. O. Muller, S. De Unamuno, B.Prevot, and P. Dhamelincourt: Phys. Stat. Sol. (A) **158**, 385 (1996)

23. F.P. Incropera and D.P. Dewitt: Fundamentals of Heat and Mass Transfer (John Wiley & Sons, New York, 1996)

24. M. A. Shannon, X. Mao, A. Fernandez, W.T. Chan, and R. E. Russo: Anal. Chem. **67**, 4522 (1995)

25. J.R. Ho, C.P. Grigoropoulos, and J.A.C. Humphrey: J. Appl. Phys. **79**, 7205 (1996)

26. X. Mao and R. Russo: Appl. Phys. A **64**, 1 (1997)

27. D.R. Lide: CRC Handbook of Chemistry and Physics, 75th Edition (CRC, 1994)

28. A. Yoshida: J. Japan Inst. Metals **58**, 1161 (1994)

29. S. H. Jeong, R. Greif, and R. E. Russo: Proceedings of the ASME Heat Transfer, Vol. HTD **351**, 68 (1997)

30. S. I. Anisimov: Soviet Physics JETP **27**, 182 (1968)

31. J.R. Ho, C.P.Grigoropoulos, and J.A.C. Humphrey: J. Appl. Phys. **78**, 4696 (1995)

32. D.R. Atthey, J. Inst. Math. Appl. **13**, 353 (1974)

33. Shamsundar and E.M. Sparrow: J. Heat Trans. **97**, 333 (1975)

34. A. J. Dalhuijsen and A. Segal: International Journal for Numerical Methods in Engineering **23**, 1807 (1986)

35. G. H. Meyer: SIAM J. Numer. Anal. **10**, 522 (1973)

36. V. A. Batanov, F. V. Bunkin, A. M. Prokhorov, and V. B. Fedorov: Soviet Physics JETP **36**, 311 (1973)

37. R. V. Karapetyan and A. A. Samokhin: Sov. J. Quant. Electron. **4**, 1141 (1975)

38. F. V. Bunkin and M. I. Tribelskii: Sov. Phys. Usp. **23**, 105 (1980)

39. M. Born and E. Wolf: Principles of Optics (Cambridge University Press, New York, 1980)

40. X.L. Mao, W.T. Chan, M.A. Shannon, and R.E. Russo: J. Appl. Phys. **74**, 4915 (1993)

Chapter 5

Dependence of Phase Explosion on Laser Sampling Parameters and its Effects on Inductively Coupled Mass Spectrometry

5.1 Introduction

Laser ablation with inductively coupled plasma (ICP), mass spectroscopy (MS), or atomic emission spectroscopy (AES) has been investigated extensively for direct solid sample chemical analysis, due to its many advantages: any sample material, minimal sample preparation, localized (spatial) analysis, and minimal exposure of personnel to toxic samples [1,2,3,4,5,6,7]. For most conditions, the solid sample is ablated inside a simple chamber and the ablated mass is transported by a carrier gas to an ICP for analysis by AES or MS. In the ideal case, the chemical composition of the ablated mass should be identical to the parent sample to ensure accuracy and transport efficiency should be large to enhance sensitivity and detection limits. However, the sampling conditions often deviate from the ideal due to such factors as preferential vaporization of elements from the sample, failure of large particulates to be transported, and fractionation caused by incomplete vaporization of the large particulates in the ICP itself [1,4,8,9,10]. For these reasons, the quantity of the ablated mass and its size distribution are crucial factors that must be known in order to characterize and optimize the laser parameters for samples of interest.

When a micron-sized laser beam is used for localized chemical analysis of the sample, the laser irradiance can attain values well above 10^9 W/cm^2. At these

irradiance levels, mass removal can take place by multiple mechanisms including desorption, thermal evaporation, surface instability of the molten mass, and exfoliation; therefore, an analytical estimation of the mass removal for high irradiance laser ablation can be a formidable task., It was shown in the previous chapters that at irradiances exceeding 10^{10} W/cm^2, enhanced mass removal due to phase explosion (explosive boiling) can occur and mass may be moved in the form of large droplets.

The dramatic increase in ablated mass and the generation of large particulates due to phase explosion can significantly influence transport efficiency and the ICP-AES or MS signal intensities. It appears that there have not been any studies that have investigated the effect of phase explosion on transport efficiency or on the ICP-MS or AES signal intensities. The motivations of this chapter are three-fold. First, a relationship between the crater depth and volume data with respect to the ICP-MS intensity signal was made over the irradiance range involving phase explosion. The sudden increase in the crater depth at the phase explosion threshold irradiance influences the ICP-MS integrated intensity. Secondly, dependence of the threshold irradiance of phase explosion on various laser sampling parameters such as the beam area and wavelength was investigated. Finally, the ratio of ICP-MS integrated intensity to net crater volume (cratrer volume below the original surface subtracted by the volume above) is estimated over the irradiance range in which phase explosion occurs. Crater volume is a good indication of mass removed from the sample, whereas the integrated ICP-MS signal

over the sampling time is proportional to the mass reaching the ICP. The behavior of this ratio over the investigated irradiance range shows how the entrainment and transport efficiency of the ablated mass can vary before and after phase explosion.

5.2 Experimental System

The optical set-up discussed in Chapter 2 was used to deliver the laser beam to the silicon sample surface: an Infinity 40-100 Nd-YAG laser (FWHM = 3 ns and λ = 266 nm), a pinhole spatial filter in a vacuum cell, a pair of plano-covex lens used for laser beam collimation, and a laser beam focusing lens. Laser ablation sampling was done using an ICP-MS (VG Elemental, PQ3) and an ablation cell with a quartz window. A single crystal silicon sample was placed on an XYZ translation stage inside the ablation cell with manual controls. Ablated mass was transported to the ICP torch along a 1.4 m polyethelene tube with 4.3 mm i.d. Tube length between the ablation chamber and the ICP was 1.4 m. The ICP-MS was operated at forward rf power of 1350 W and gas flow rates of 14, 10, and 1.0 L min^{-1} respectively for plasma, auxiliary, and carrier flows. ICP-MS lens voltages were optimized to achieve maximum sensitivity for ^{29}Si. ICP-MS was operated in a single-ion-monitoring mode. Time-resolved ICP-MS signal intensity for ^{29}Si was measured during single pulse laser ablation of the sample with dwell time of 12 ms and 3 points per peak. Depending on the laser ablation parameters it took about 30 s for signal intensity to return to the background levels. The laser pulse was fired following a delay of 3 sec after starting the ICP-MS data acquisition. The system

intensity data recorded during the time delay were used in signal background calculations and subtractions. The integrated intensity was defined as the ICP-MS ^{29}Si intensity integrated over acquisition time with background subtraction.

5.3 Results and Discussion

5.3.1 Phase explosion and correlation of crater depth with respect to ICP-MS intensity counts

The MS signal intensity is proportional to the total mass removed from the sample surface and transported to the ICP [11,12]. For constant ICP conditions, the change in the ICP-MS or AES signal intensity can signify a change in mass removal due to onset of additional processes that cause or assist mass removal. It has been reported that the onset of plasma shielding for 30 nsec laser ablation causes a roll-off in the signal intensity. The onset of plasma shielding occurred at the irradiance of 0.3 ~0.4 GW/cm^2. The roll-off was attributed to a decrease in the rate of mass removal due to absorption of laser energy by the plasma formed above the sample surface, which resulted in a decrease in the fraction of the energy reaching the surface [11,12]. It is presumed that at the onset of phase explosion, there is a dramatic increase in both crater depth and volume. The enhanced mass removal due to phase explosion should result in a rapid rise in the ICP-MS integrated signal intensity.

Figure 5.1 shows the ICP-MS integrated intensity as a function of laser irradiance for the silicon sample ablated using the 3 nsec pulsed Nd:YA at 266 nm.

A sharp increase followed by a leveling off in the crater depth were observed in Ar for the 45 μm beam size. The corresponding ICP-MS integrated signal intensity data show two distinct regimes with respect to the threshold laser irradiance. For irradiances above the threshold, the total integrated intensity increases rapidly for increasing irradiance. Similar trends were observed at larger beam sizes of 55 and 65 μm; larger beam sizes yielding a higher integrated signal count due to more mass being removed from a larger area. Even though the growth of the crater depth and the net volume (the volume below the original surface subtracted by the volume above) levels off above 200 GW/cm^2 for the 45 μm beam size, the ICP-MS signal continually increases above this irradiance. These data imply that despite the leveling off of the total mass ablated from the sample, more mass is entrained and transported to the ICP at the high irradiances. The reason for this result is not yet fully understood: some possible explanations are discussed in the following sections.

5.3.2 Influence of laser wavelength and beam size on phase explosion

At and above threshold laser irradiance, the ICP-MS integrated intensiy increases at a substantially higher rate. In addition, a change in the size distribution of the ejected mass can occur above this value and this is attributed to liquid droplets being ejected from superheated volume during a phase explosion. The size distribution of the ablated mass will influence entrainment and transport efficiency

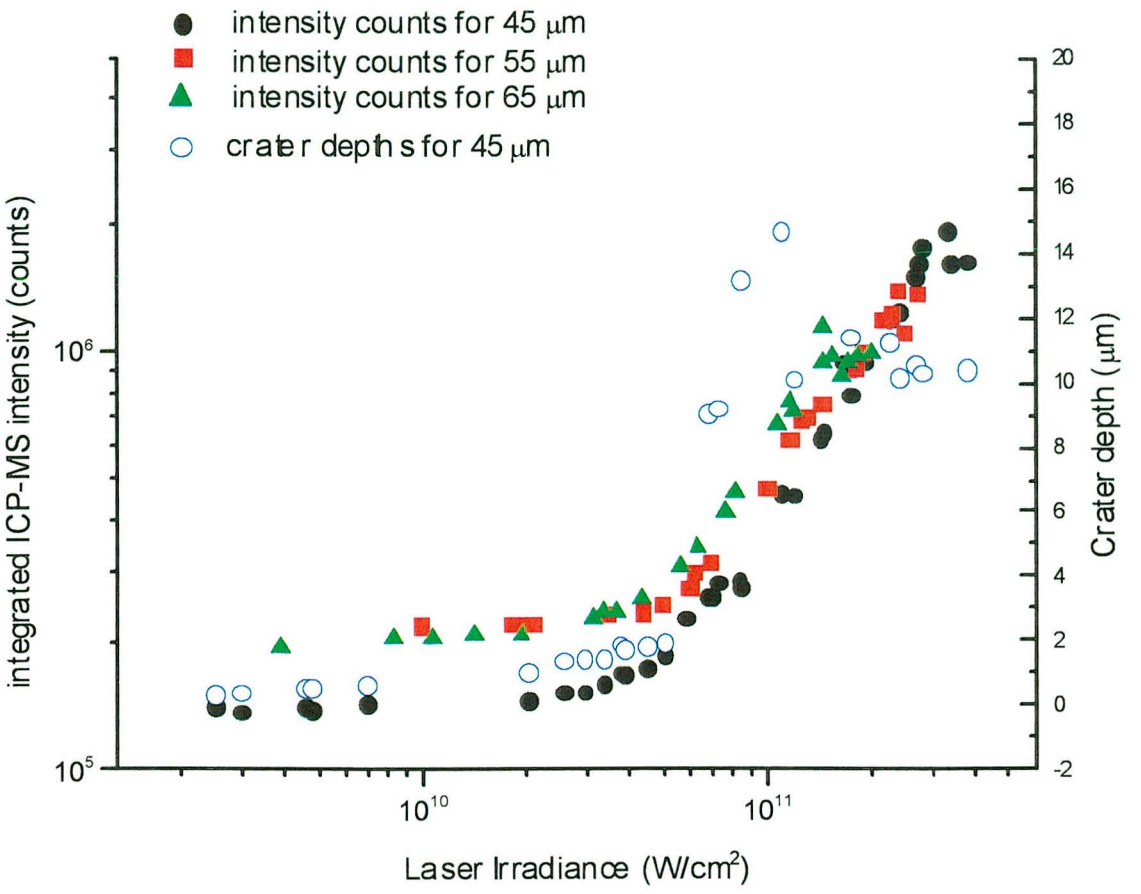

Figure 5.1 Correlation of Integrated ICP-MS signal with the crater depth for high irradiance laser ablation of silicon involving phase explosion

to the ICP. In order to investigate the effects of different laser sampling conditions on the threshold irradiance, single pulse (FWHM = 3 ns) ablation was conducted on a single crystal silicon sample in air by varying three parameters: laser irradiance ($10^9 \sim 10^{12}$ W/cm2), beam size (18 ~ 50 μm), and wavelength (λ = 266, 532, and 1064 nm). The ablated crater depths as a fuction of laser irradiance are plotted for several beam sizes in Figures 5.2, 5.3, and 5.4 at each wavelength. From these data, the following observations can be made: 1) the threshold irradiance is strongly dependent on the incident laser wavelength, and 2) at the same laser wavelength, the threshold irradiance is dependent on the laser beam spot size.

The threshold dependence on incident wavelength is illustrated in Figure 5.5. For approximately the same laser beam diameter of 35 μm, the 266 nm wavelength generated the lowest irradiance threshold of ~20 GW/cm^2, the 532 nm wavelength yielded a threshold irradiance of ~420 GW/cm^2 (roughly one order of magnitude higher). At the 1064 nm wavelength, a drastic increase in the crater depth was not observed. Two possible factors may contribute to these results: namely, stronger plasma shielding and deeper optical absorption lengths may occur at longer wavelengths. Plasma shielding reduces the quantity of laser energy available for heating the sample and the increased optical absorption length leads to more volumetric heating of the sample.

The ablated mass, which contain both ionized and neutral species of atoms and molecules formed by the early part of the laser pulse, can interact with the latter part of the pulse, and absorb the laser energy and thereby shield the target

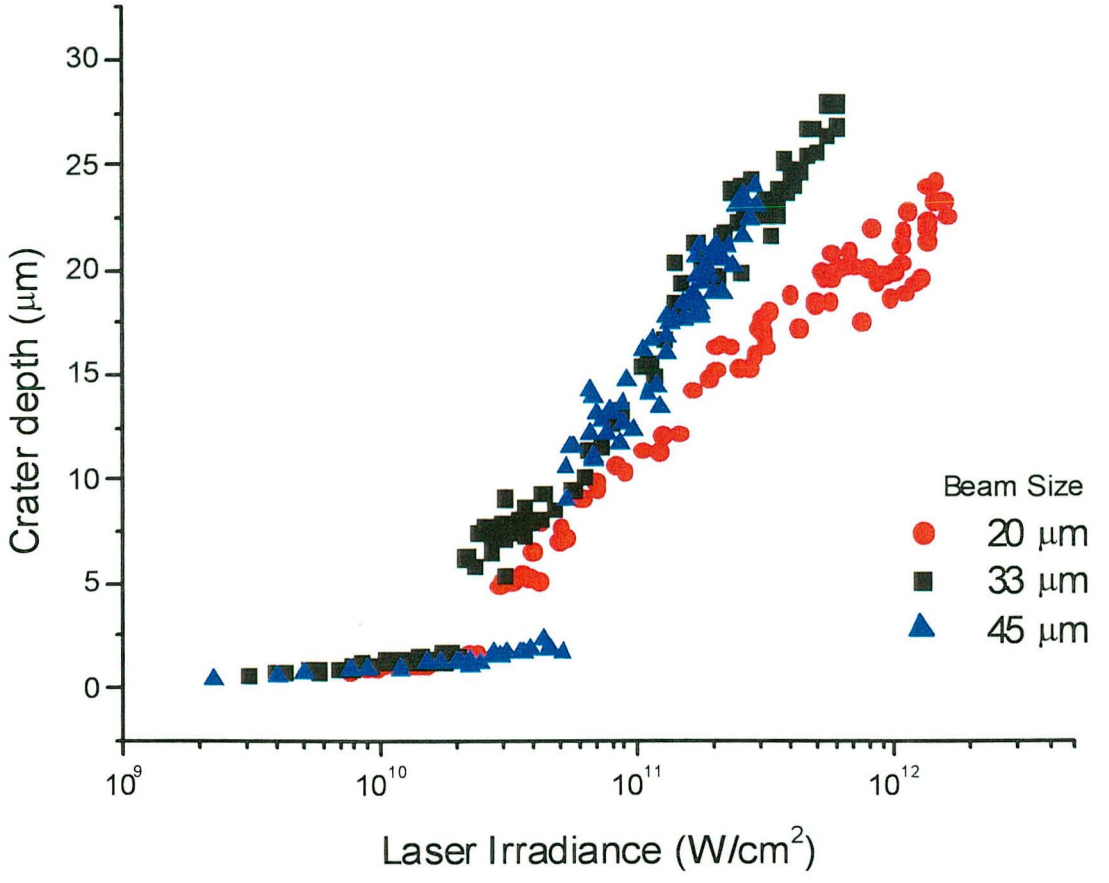

Figure 5.2 Crater depths as a function of laser irradiance for different laser beam sizes at $\lambda = 266$ nm

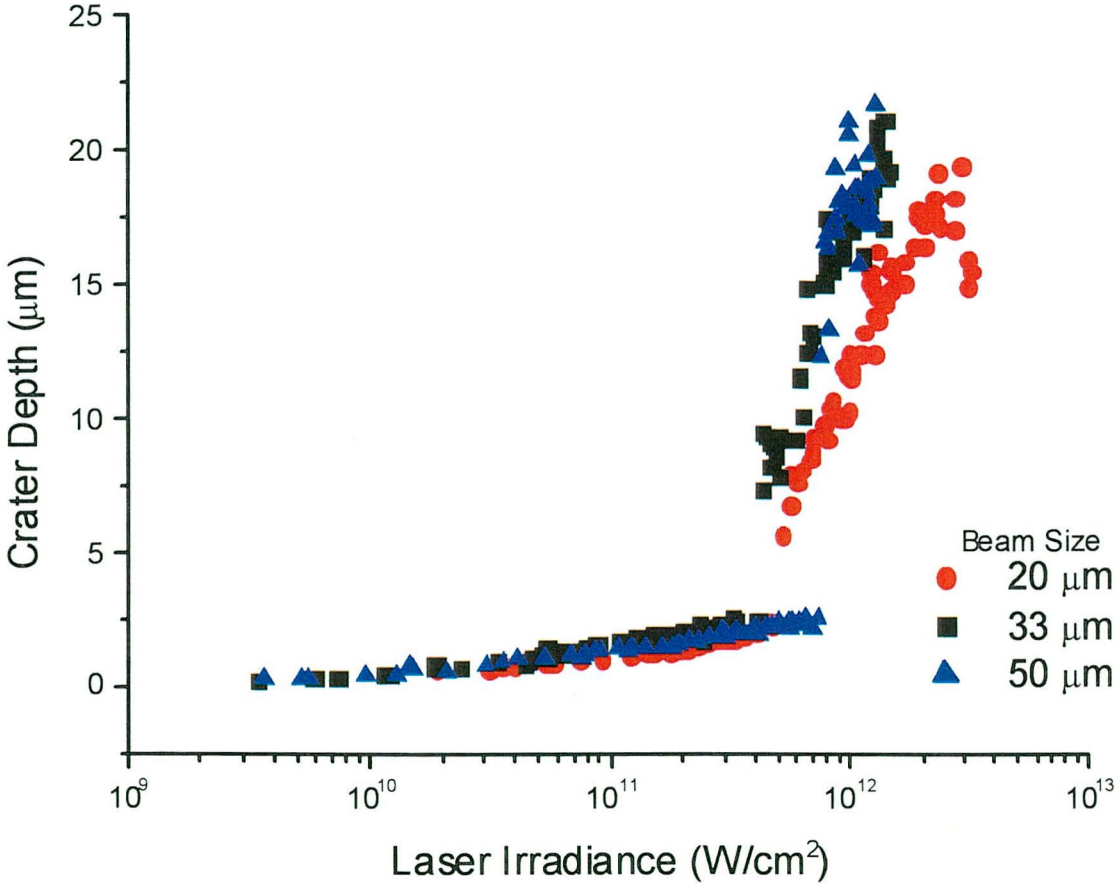

Figure 5.3 Crater depths as a function of laser irradiance for different laser beam sizes at $\lambda = 532$ nm

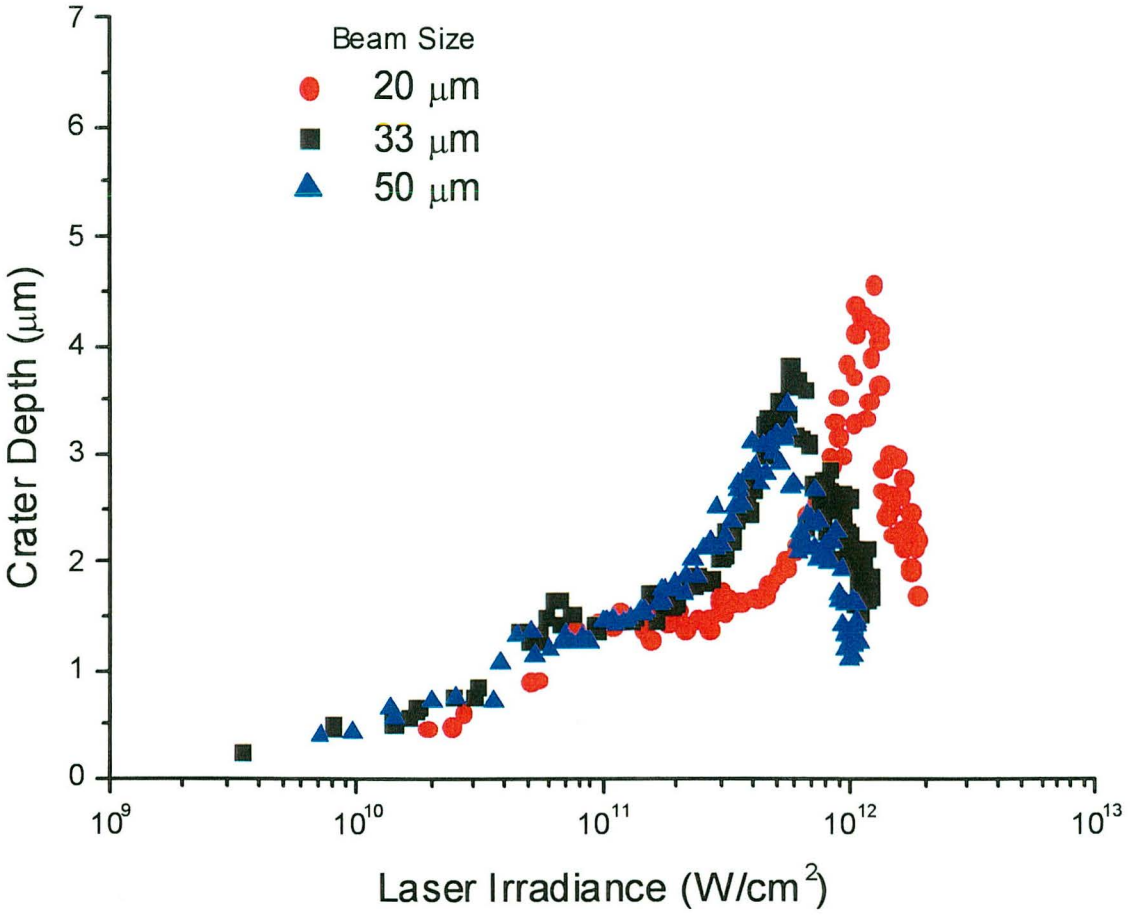

Figure 5.4 Crater depths as a function of laser irradiance for different laser beam sizes at $\lambda = 1064$ nm

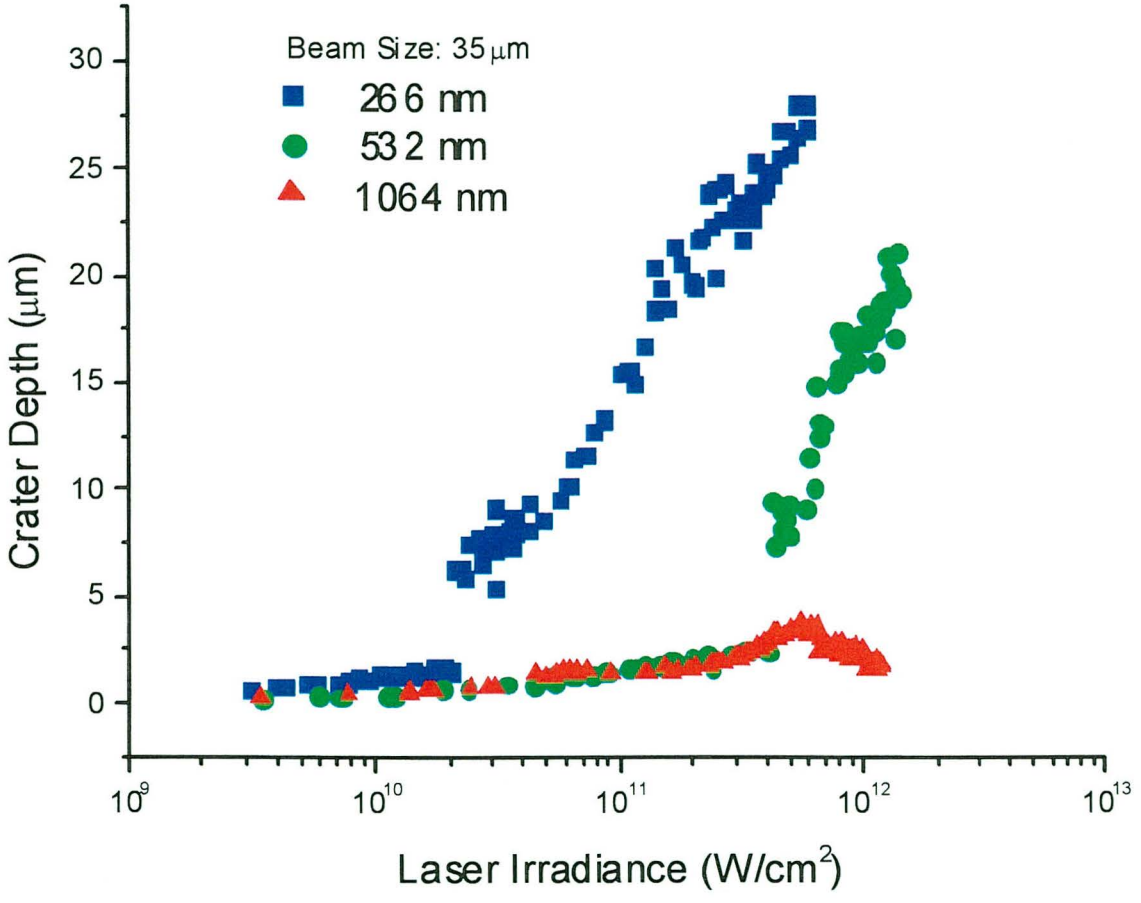

Figure 5.5 Dependence of crater depth on incident laser wavelength for laser beam size of 35 μm

from the incident radiation. The spectroscopic work of Liu et al [13] showed that for early phase silicon plasmas, at laser irradiance significantly below the threshold irradiance, the plasma was sufficiently ionized so that electron-ion inverse bremsstrahlung could dominate absorption for UV radiation. Electron-ion inverse bremsstrahlung is a stronger absorption mechanism for longer wavelengths [14,15]. The absorption coefficient α_p (cm^{-1}) for electron-ion inverse bremsstrahlung is expressed as [13]:

$$\alpha_p = 3.69X10^8 \frac{Z^3 n_i^2}{T^{1/2}\nu^3}[1-\exp(h\nu / kT)] \tag{5.1}$$

where Z, n_i, T, and λ are the average ion charge, ion density, temperature of the plasma, and the incident light wavelength. For sufficiently hot plasma (kT>>νT), the expression (5.1) can be simplified to:

$$\alpha_p \propto n_i^2 \lambda^2 / T^{3/2} \tag{5.2}$$

Therefore, at longer wavelengths, substantially higher absorption of the incident radiation can occur and less radiation energy will therefore be transmitted to the sample surface. It is possible that not enough laser energy would then be available to create a pool of superheated molten layer and heat it close to its critical temperature and generate phase explosion.

Another factor that could contribute to the higher threshold irradiance at the longer wavelength is the wavelength-dependent optical absorption of silicon. Absorption characteristics of silicon are illustrated in Figure 5.6. At 266 nm, the optical penetration depth for silicon is on the order of ten nanometers; all of the

incident optical energy is absorbed in a very small region near the surface, rapidly increasing its local temperature. Steep temperature gradients will exist in this region, causing large heat conduction into the bulk solid and forming a superheated liquid. At 532 nm, the optical penetration depth increases to hundreds of nanometers, which is still an order of magnitude less than the thermal diffusion (~ 1 μm) length for the 3 ns laser pulse. Therefore, as with the 266 nm wavelength radiation, the optical energy is deposited in a relatively shallow region near the surface and transported primarily by heat conduction into the bulk sample. However, at 1064 nm, the optical penetration depth (~ 200 μm) is two orders of magnitude greater than the thermal diffusion length (~ 1 μm); the absorption of the incident radiation and subsequent heating will therefore be volumetric. Since heating occurs over a substantially larger volume, the resulting peak temperature as well as the temperature gradient are less than for the 266 and 532 nm. Thus, at 1064 nm wavelength, the effects of both strong plasma absorption of the incident radiation as well as volumetric heating of the solid from the portion of the incident radiation that is transmitted may prevent the sample from attaining the superheated liquid state for the duration required for vapor nuclei to grow to the critical size. At 266 and 532 nm, greater transmission of the incident radiation and higher absorption near the surface would result in higher peak temperatures of the sample. This could contribute to the formation of superheated liquid near the critical state and the possible onset of a phase explosion. Higher threshold irradiances at 532 nm compared to that at 266 nm could be attributed to higher absorption of incident

radiation by the plasma layer, which decreases the transmitted energy to the surface.

The threshold irradiance is also dependent on the laser beam size. At both 266 and 532 nm, the threshold irradiance increased for a larger beam diameter. Figure 5.7 shows the dependence of the threshold value on the laser beam sizes for $\lambda = 532$nm. For laser beam sizes less than 35 μm, the threshold remained at ~ 420 GW/cm^2. However, for larger beam sizes, a higher threshold irradiance was required to generate phase explosion: at ~ 70 μm, irradiance exceeding 1000 GW/cm^2 was required. The dependence of the threshold irradiance on the laser beam size can be explained in terms of plasma expansion dynamics for different spot sizes. For small beam sizes , the three-dimensional spherical plume expansion is likely to occur. As the beam size increases, the expansion could shift towards a more planar front. The reduction in the plasma expansion dimension for a larger beam diameter may result in a decrease of the effective volume for the plasma layer and hence higher ion/electron number density. Increased ion/electron density increases the plasma absorption of the incident radiation and a higher irradiance may be required to compensate for the greater absorption by the plasma layer to initiate the threshold irradiance.

5.3.3 Dependence of the entrainment and transport efficiency on the laser irradiance

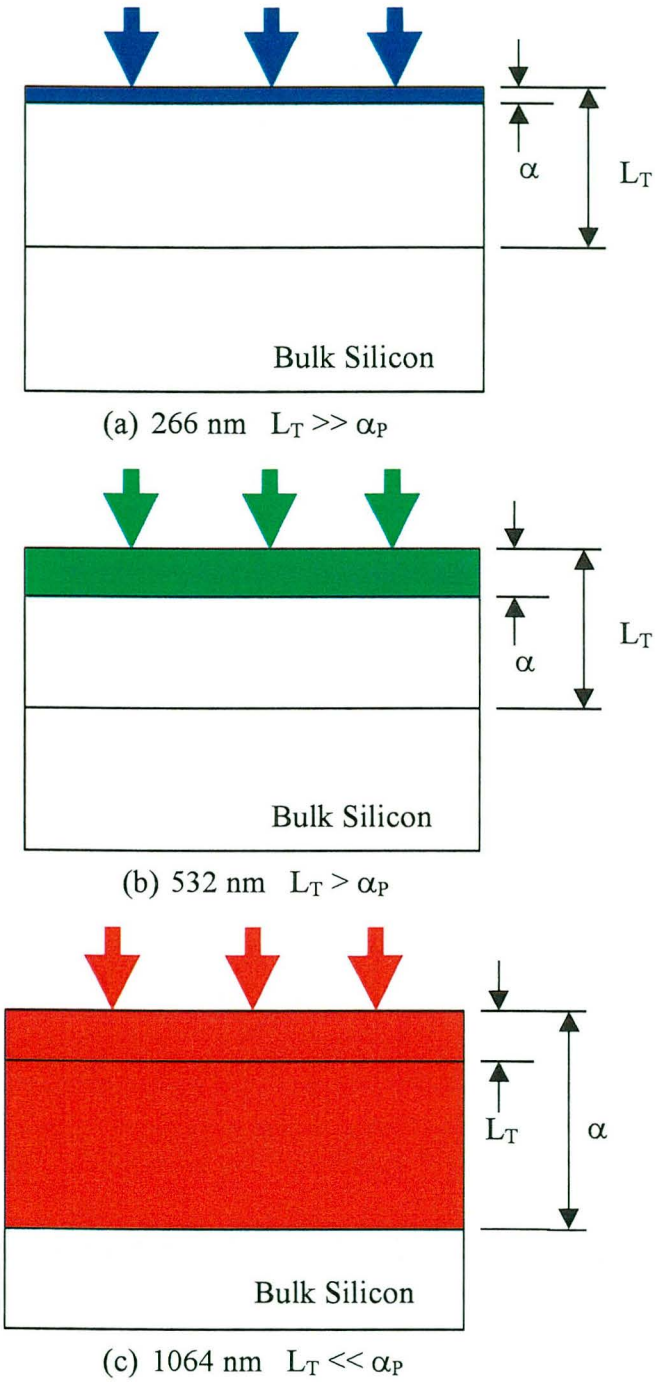

Figure 5.6 Wavelength-dependent absorption of incident laser light in silicon (L_T = thermal penetration depth, α_P = optical penetration depth)

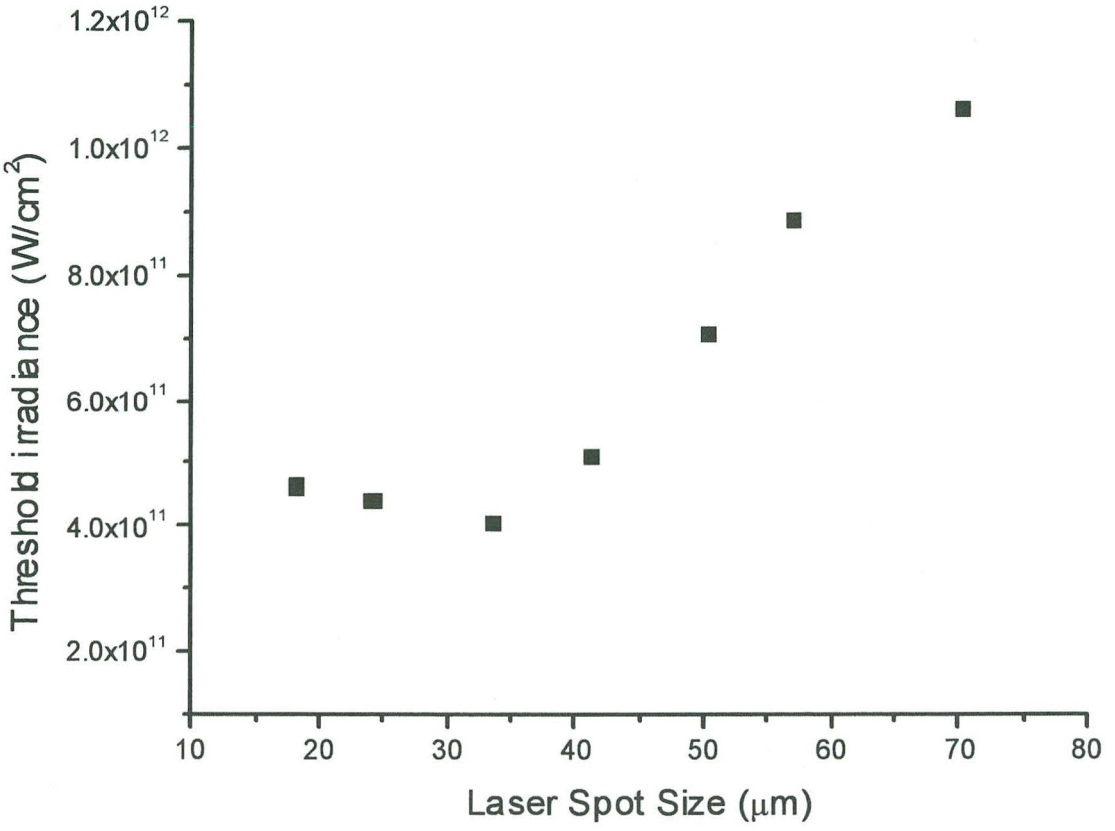

Figure 5.7 Dependence of phase explosion threshold on laser beam sizes at λ = 532 nm

An investigation of mass ejection due to phase explosion was made in Chapter 3. It was shown that initiation of a phase explosion occurs at ~400 nsec after the laser pulse, followed by ejection of large particulates and continuing for microseconds. Some of the particulates were estimated to be as large as 10 μm.

Due to gravity, large particulates will not be entrained into the argon gas flow and instead will fall into the ablation chamber [10]. In addition, these particles can settle in the transport tube. Thus, in the irradiance range large particles are present, entrainment and transport to the ICP could decrease. To assess these affects on particle entrainment and transport efficiency, the ratio of the net ICP-MS intensity (integrated counts with background subtraction) to the net crater volume was measured for laser irradiances from $5x10^9$ to $1x10^{12}$ W/cm^2 for several beam sizes. The net crater volume times the density of the sample indicates the mass that has been removed; the integrated signal is proportional to the mass entrained and transported to the ICP.

Figure 5.8 shows the variation of the ratio as a function of laser irradiance at λ = 266 nm for various beam sizes. The ratio decreases until the phase explosion threshold irradiance (~ 25 to 75 GW/cm^2 for the laser beam size ranging from 30 to 72 μm) is reached, then stays constant, and then rises again at ~100 GW/cm^2. Jeong et al. [10] reported lower entrainment efficiency for ablation of glass sample at higher power densities. The observed decrease in the ratio for increasing irradiance below the threshold (cf. Figure 5.8) is consistent with these previous data. One possible reason for the decrease could be the increase in the number of

larger particulates produced by liquid droplet ejection, induced by hydrodynamic motion or "wash-out" of the molten layer, caused by the larger recoil pressure of the evaporating vapor at higher irradiances. Once the threshold occurs, the ratio (transport efficiency) remained at the lowest value. Large particulates with sizes approaching ten microns as shown in the shadowghraph images will not be entrained.

It is not clear why the ratio (cf. Figure 5.8) increases for increasing irradiances that are well above the threshold. The irradiance where the ratio starts to increase corresponds to the irradiance where leveling-off in the crater depth occurs. As shown in Figure 5.1, above 100 GW/cm^2 for laser ablation at 266 nm and with Ar carrier gas, the crater depth reaches a maximum value for the 45 μm beam size. Similar trends were observed for different beam sizes (not shown in the figure). In Figure 5.8, the increase in the ratio starts approximately at this irradiance. The leveling-off of the crater depth is also observed for laser ablation in the air ambient. When Figure 5.2 is replotted on a linear scale (Figure 5.9), it is clearly seen that the leveling-off of the crater depth occurs in air above a certain irradiance at $\lambda = 266$ nm. The leveling-off or decrease in the crater depth at high irradiance may be attributed to increasing absorption and reflection of the incident light due to the dense plasma layer. The plasma angular frequency, w_p, defines a limit for the lowest frequency of laser radiation which can be transmitted. In terms wavelength, the above statement is equivalent to $\lambda < \frac{c}{8.98(n_e)^{1/2}}$ where c is the speed of light and n_e is the electron number density [16]. Thus, at the laser

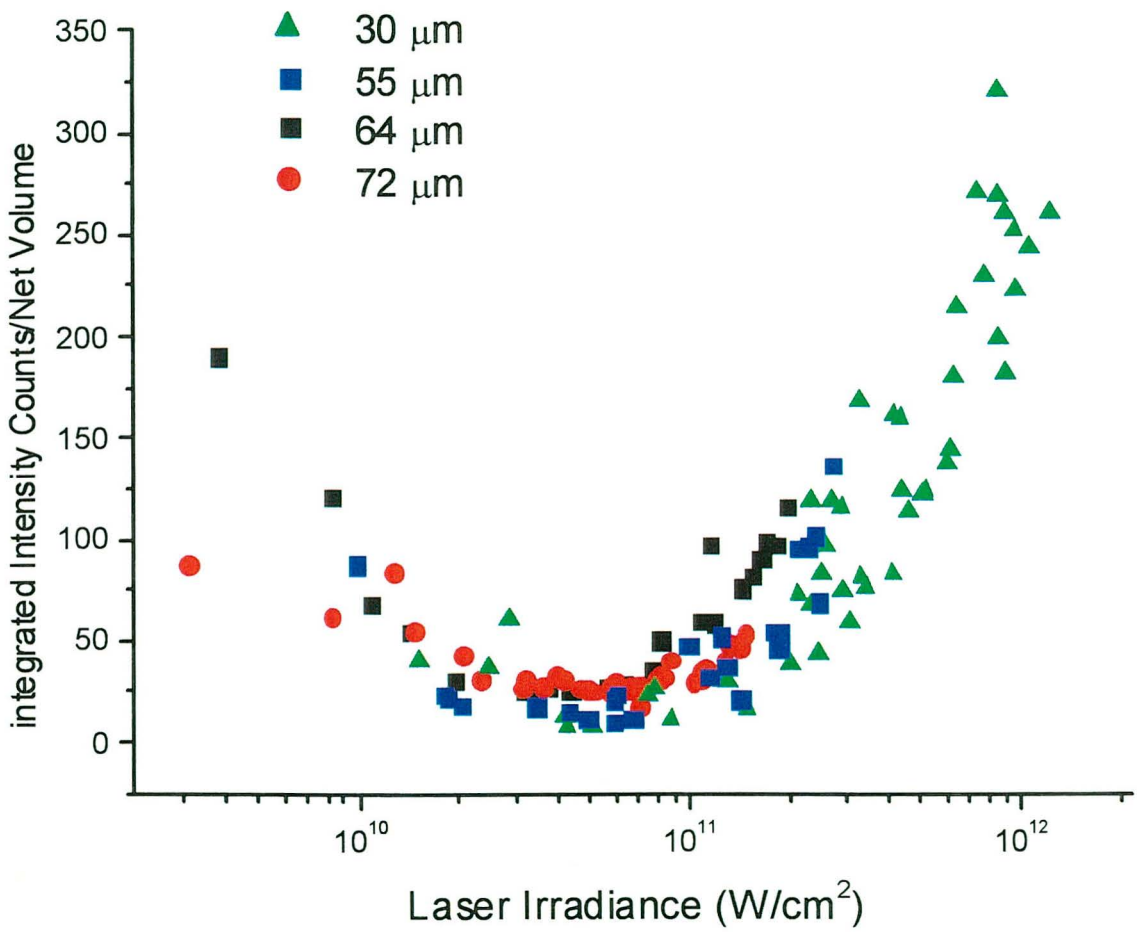

Figure 5.8 Ratio of integrated ICP-MS intensity to net crater volume as a function of laser irradiance

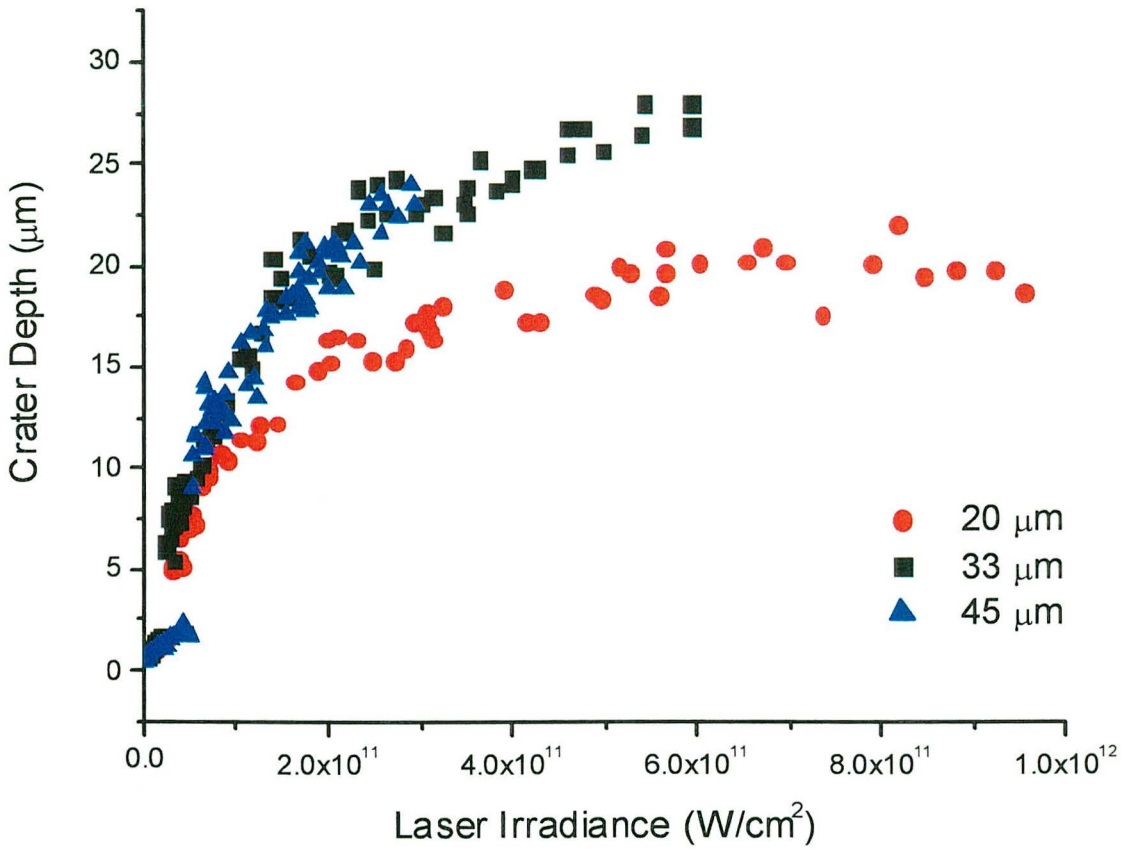

Figure 5.9 Crater depths as a function of laser irradiance at λ - 266 nm on a linear scale (replot of Figure 5.2)

wavelength of 266 nm, the reflection of incident irradiation can occur for a plasma with n_e greater than approximately 1.6×10^{22} cm^{-3}. At the upper laser irradiance range used in the current work, a very dense plasma layer can form above the sample, with local value of n_e greater than the reflection limit for the incident radiation; the plasma then becomes more reflective. The incident irradiation is also absorbed strongly by inverse bremsstrahlung since the degree of ionization at high irradiance is high [13]. Thus, a combination of strong reflection and absorption of the optical energy in the plasma layer limits the energy transfer to the sample surface, ultimately resulting in a leveling-off or even decrease in the crater depth as irradiance is increased beyond a certain value.

Leveling-off of the growth of the crater depth could suggest a similar maximum value for the number of large particulates ejected. Furthermore, very strong absorption of the incident energy in the plasma layer could create a region of high density, temperature, and pressure above the sample surface. Subsequent rapid expansion of the plasma in this region could produce a high ejection velocity of the ablated mass and a lower fraction that recondense on the sample surface. High plasma temperatures could also initiate plasma heating of the large particulates, breaking them into smaller size particles that are more easily entrained and transported. More investigations on the particle distribution of the ablated mass generated in this irradiance range are needed to fully understand the observed trends.

5.4 Conclusions

High irradiances above the threshold value may have several benefits. In the case of a composite sample material, it can be heated instantaneously and a pool of superheated liquid, comprised of all elements above the boiling point, may form. This rapid heating of the sample to the temperature near the critical state may eliminate factors such as preferential vaporization and elemental fractionation, leading to a good stoichiometric representation of the ablated mass to the parent sample.

One drawback of doing solid sampling under this irradiance range is the production of large particulates, which may result from homogeneous nucleation of vapor bubbles in the superheated volume and their subsequent rapid expansion. These large particulates can settle onto the transport tube or fall into the ablation chamber, leading to poor entrainment and transport efficiency. The current work has indicated that the entrainment and transport efficiency is a minimum at laser irradiances slightly above the threshold value. In addition, it has shown that the threshold irradiance depends on both the laser wavelength and the beam size; a higher threshold irradiance resulted for longer wavelengths and larger beam sizes.

At laser irradiances well above the threshold, as indicated by the higher ratio of the integrated ICP-MS intensity to the net crater volume, the entrainment and transport efficiency increased. At these large irradiances, highly absorbing and more reflecting plasma layers may form above the sample surface, which would shield the incident radiation from the sample surface and limit the formation of the

superheated layer and generation of the large particulates. Furthermore, radiative heating of the hot plasma layer may be effective in breaking the large particulates into smaller parts that are more readily entrained and transported. Thus, identification of the phenomena that occur well above the threshold value could be essential for performing both accurate and efficient sampling under high irradiances.

REFERENCE

1. R.E. Russo: Appl. Spectrosc. **49**, A14 (1995)
2. L. Moenke-Blankenburg: Spectrochim. Acta Rev. **15**,1 (1993)
3. S.A. Darke and J.F. Tyson: J. Anal. At. Spectrom. **8**, 145 (1993)
4. W.T.Chan and R.E. Russo: Spectrochim. Acta **46B**, 1471 (1991)
5. P. Arrowsmith: Anal. Chem. **59**, 1437 (1987)
6. R.E. Denoyer, J.K. Fredeen, and J.W. Hager: Anal. Chem. **63**, 445 (1991)
7. Y. Huang, Y. Shibata, and M. Morita: Anal. Chem. **65**, 2999 (1993)
8. E.F. Cromwell and P. Arrowsmith: Anal. Chem. **67**, 131 (1995)
9. W.T. Chan, X.L. Mao, and R.E. Russo: Appl. Spectrosc. **46**, 1025 (1992)
10. S.H. Jeong, O.V. Borisov, J.H. Yoo, X.L. Mao, and R.E. Russo: Anal. Chem. **71**, 5123 (1999)
11. M. A. Shannon, X. Mao, A. Fernandez, W.T. Chan, and R. E. Russo: Anal. Chem. **67**, 4522 (1995)
12. A. Fernandez, X. L. Mao, W.T. Chan, M. A. Shannon, and R. E. Russo: Anal. Chem. **67**, 2444 (1995)
13. H.C. Liu, X.L. Mao, J.H. Yoo, and R.E. Russo: Spectrochim. Acta **54B**, 1607 (1999)
14. H. Schittenhelm, G. Callies, A. Straub, P. Berger, and H. Hugel: J. Phys. D: Appl. Phys. **29**, 1564 (1996)
15. D. Breitling, H. Schittenhelm, P. Berger, F. Dausinger, and H. Hugel: Appy. Phys. A **69**, S505 (2000)

16. W.W. Duley: UV Lasers: Effects and Applications in Materials Science (Cambridge University Press, Cambridge, 1996)

Chapter 6

Conclusions and Future Directions

6.1 Conclusions

As laser ablation is being utilized in an increasing number of technical applications, it is important to understand the fundamental mechanisms responsible for mass removal in order to obtain better control of the quantity and the size of the removed mass. In the present study, both experimental and computational works were carried out to study an ablation mechanism that greatly increases mass removal under high irradiance. This dramatic increase in mass removal may be useful in such applications as laser drilling and welding where high mass removal efficiency is desired.

Laser shadowgraphy was used to characterize the mass ejection process. After the analysis of the phenomena, it was proposed that the ablation mechanism responsible for dramatic increase in mass removal could be phase explosion (or explosive boiling). There have been considerable discussions concerning the possibility of phase explosion as a mechanism for laser ablation. The current work examines the possible existence of this mechanism.

Substantial structural changes in the crater morphology occur at the threshold irradiance. The crater depth and volume increase dramatically and the topology is transformed into a deep and rough structure. In chapter 2, this dramatic change in the crater properties was studied for 3 ns laser ablation of single crystal silicon using white light interferometry microscope. Starting at a laser irradiance of

2.2×10^{10} W/cm^2, a large quantity of mass was removed from the central portion of the irradiated area, as evidenced by the formation of deep craters. The crater morphology consisted of a deep structure and the large droplets that were present in its vicinity indicated a possibility of a violent ejection of mass at and above the threshold irradiance.

In Chapter 3, the mass ejection was characterized using laser shadowgraph imaging. The time delay between the probe and the pump beam was varied from several picosecond to microseconds, which allowed the time-resolved study of the gas dynamics and mass ejection process at different times. A distinctive feature of the mass ejection process at high irradiances was the large-size particulate ejection, which is initiated with a time delay of approximately 300 ~ 400 ns. The large particulates were clearly visible at microsecond times. For laser ablation both above and below the threshold irradiance, formation of a conical air plasma was observed at picosecond times, which was followed by a hemispherical vapor expansion at nanosecond times.

The crater depth and characteristics of the mass ejection process were analyzed in Chapter 4. If thermal evaporation is only considered in estimating the crater depth, the depths computed underestimate the measured values by an order of magnitude for irradiances above the threshold value. This indicates that above the threshold irradiance, thermal evaporation can only be considered as a minor mechanism for mass removal. Instead, the calculated thickness of the superheated liquid near the critical temperature was found to be a good indication of the crater

depth for irradiances above the threshold. The phase explosion model developed in Chapter 4 suggests that during very rapid heating of ablating samples, a superheated liquid layer is rapidly formed and as the temperature approaches the critical value, it was assumed that it becomes optically transparent to the laser irradiance. This induced optical transparency promotes the formation of a thick superheated liquid layer within which homogenous nucleation may occur. When the bubbles formed by homogeneous nucleation grow to the critical size in the superheated liquid environment, the bubbles are assumed to spontaneously expand and eject molten droplets from the superheated volume. The time delay for the mass ejection to initiate could be related to the time for the vapor bubbles formed by homogeneous nucleation to achieve the critical size; the estimated bubble growth time agrees well with the observed delay time.

In Chapter 5, the dependence of the threshold irradiance on the laser processing parameters were studied. It was shown that longer wavelengths and larger beam sizes result in higher threshold irradiances for 3 ns laser ablation of silicon. Higher absorption of the incident laser energy by inverse Bremsstrahlung and more volumetric absorption of transmitted energy by the silicon sample may account for the higher threshold irradiance at longer wavelength. In addition, higher threshold irradiance associated with larger beam size was explained by a more planar expansion (2D) of the vapor plume for the larger beam size, resulting in a reduced effective volume for the expanding plume and hence a higher electron density number inside this volume. Chapter 5 also studied how entrainment and

transport efficiency of the ejected mass can be influenced by the onset of threshold conditions; the entranment and transport efficiency is an important parameter in chemical analysis of sample material. It was determined that just above the threshold irradiance, the entrainment and transport efficiency of the ejected mass remained at a minimum.

6.2 Future Studies

The current work suggests that during high irradiance laser ablation, a phase explosion may be present. It is suggested that this requires the presence of a superheated liquid near the critical temperature that exists long enough for vapor nuclei to reach a critical size. To enhance understanding of the phenomena, the following studies are recommended:

1. For a given incident radiation, different thermal properties such as latent heat of fusion, thermal diffusivity, critical temperature, etc should lead to different thicknesses of the superheated liquid layer. Therefore, different sample materials should have different threshold irradiances and crater depths and this should be investigated. To repeat, the effects of thermal properties on the onset of phase explosion should be investigated by studying crater morphology for different materials as a function of the laser irradiance.

2. The laser pulse interval can influence the onset of phase explosion. For long laser pulse intervals (> 1 μs), the sample can be heated to near critical temperature and vapor nuclei due to homogeneous nucleation may be generated and grow to a critical size during the laser pulse. Consequently, phase explosions may be observed during long laser pulses. However, as the pulse interval is reduced, the superheated liquid region will be smaller and upon termination of the laser pulse, may not persist long enough to allow vapor bubbles to grow to a critical size; hence phase explosion may not occur. Thus, phase explosions may not be the dominant mechanism for ultrashort pulse (sub-picosecond or femtosecond) laser ablation. Further studies of the effects of pulse duration on the onset of phase explosion should be conducted.

3. Shielding effects of plasma significantly reduce the fraction of radiation reaching the material surface. The plasma shielding can depend on the incident wavelength as well as vapor expansion dynamics. Additional shadowgraph imaging work is needed to explore plasma expansion dynamics at different incident wavelengths and beam sizes. Furthermore, interferometry measurements to determine the electron number density at these different conditions would be useful in conjunction with shadowgraph imaging. From the electron number

density results, the absorption coefficient of the plasma can be determined and the amount of plasma shielding can be quantified.

4. A rapid expansion of the dense plasma that occurs after the laser heating may cause rarefaction waves to propagate towards the sample surface; as a result, strong tensile waves can develop and propagate in the superheated liquid. The rate of homogeneous nucleation is dependent on the pressure of the superheated liquid as well as its temperature. Therefore, tensile pressure waves are likely to influence nucleation processes and the onset of phase explosion. More rigorous analyse of the phase explosion phenomena should include the increase in the local pressure of the superheated liquid due to tensile pressure waves.

In addition to a phase explosion, the hydrodynamics of the melt layer may be important in determining the mass removal under high laser irradiance. Many solid state lasers have a Gaussian spatial beam profile that has a higher intensity in its central portion, which results in greater mass removal and a higher pressure at the central portion of the laser beam. At high laser irradiance, a Gaussian beam profile may cause stronger plasma shielding in the central portion than in the peripheral region of the laser beam. Larger shielding in the center may cause a greater reduction in the amount of mass being removed from the surface from the center, which would reduce the pressure increase above the surface after the laser

pulse. Consequently, a smaller pressure gradient may result because the pressure at the center is not as large as it would be without shielding. It is even possible that strong shielding in the center may result in a pressure at the center that is less than at the periphery. This pressure gradient would then induce a liquid flow towards the center of the beam and cause jetting of the liquid mass. Further studies are needed to assess the hydrodynamic effects on the mass removed under high irradiance laser ablation.

Ernest Orlando Lawrence Berkeley National Laboratory
One Cyclotron Road | Berkeley, California 94720

Prepared for the U.S. Department of Energy under Contract No. DE-AC03-76SF00098